Cell

Article

Biomaterial-minimalistic photoactivated bioprinting of cell-dense tissues

Graphical abstract

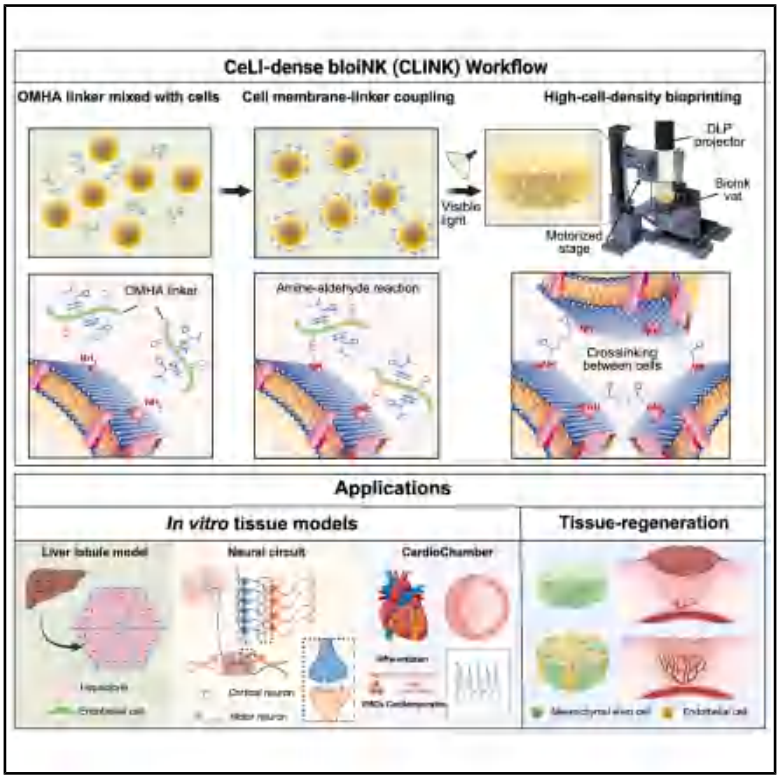

Highlights

- Living-cell-only photoactive bioinks enables scaffold-free light-based 3D bioprinting
- Ultrahigh cell densities are achieved in bioprinted tissues, mimicking native ones
- Cell-dense neural circuits and mini-hearts are rapidly bioprinted as *in vitro* models
- Vascularized liver and skin grafts promote *in vivo* integration and regeneration

Authors

Mian Wang, Wanlu Li, Jin Hao, ..., Kevin Eggan, Shaorong Gao, Yu Shrike Zhang

Correspondence

yszhang@bwh.harvard.edu

In brief

We developed a bioprinting strategy that turns living cells into cell-only bioinks, enabling light-based 3D bioprinting of tissues at native, ultrahigh cell densities (up to $\sim 10^9$ cells mL^{-1}) to rapidly yield functional neural circuit and beating mini-heart models as well as vascularized liver and skin grafts that promote regeneration.

Wang et al., 2026, Cell *189*, 1–17
January 8, 2026
https://doi.org/10.1016/j.cell.2025.11.012

CellPress

Please cite this article in press as: Wang et al., Biomaterial-minimalistic photoactivated bioprinting of cell-dense tissues, Cell (2026), https://doi.org/10.1016/j.cell.2025.11.012

Cell

CellPress

Article

Biomaterial-minimalistic photoactivated bioprinting of cell-dense tissues

Mian Wang,[1,11,13] Wanlu Li,[1,12,13] Jin Hao,[2,3,4,13] Ling Cai,[1,13] Xuan Mei,[1] Regina Sanchez Flores,[1] Penélope Cerón Castillo,[1] Carlos Ezio Garciamendez-Mijares,[1] Xuan Mu,[1] Xiao Kuang,[1] Xianbin Yu,[6] Jugal Kishore Sahoo,[5] Guosheng Tang,[1] Zeyu Luo,[1] Guillermo Wells,[1] Zhongmin Liu,[7] Alfredo Quiñones-Hinojosa,[8] Kevin Eggan,[2,3,4] Shaorong Gao,[9] and Yu Shrike Zhang[1,3,10,14,*]

[1]Division of Engineering in Medicine, Department of Medicine, Brigham and Women's Hospital, Harvard Medical School, Cambridge, MA, USA
[2]Department of Stem Cell and Regenerative Biology, Harvard University, Cambridge, MA, USA
[3]Harvard Stem Cell Institute, Harvard University, Cambridge, MA, USA
[4]Stanley Center for Psychiatric Research, Broad Institute of MIT and Harvard, Cambridge, MA, USA
[5]Department of Biomedical Engineering, Tufts University, Medford, MA, USA
[6]Department of Chemistry, Department of Biochemistry and Molecular Biology, and Institute for Biophysical Dynamics, The University of Chicago, Chicago, IL, USA
[7]Translational Medical Center for Stem Cell Therapy and Institute for Regenerative Medicine, Shanghai East Hospital, Tongji University School of Medicine, Shanghai, China
[8]Departments of Neurosurgery, Oncology, and Neuroscience, Mayo Clinic, Jacksonville, FL, USA
[9]Shanghai Key Laboratory of Maternal Fetal Medicine, Clinical and Translational Research Center of Shanghai First Maternity and Infant Hospital, Shanghai Institute of Maternal-Fetal Medicine and Gynecologic Oncology, Frontier Science Center for Stem Cell Research, School of Life Sciences and Technology, Tongji University, Shanghai, China
[10]Broad Institute of MIT and Harvard, Cambridge, MA 02142, USA
[11]Present address: Frontier Science Center for Stem Cell Research, School of Life Sciences and Technology, Tongji University, Shanghai, China
[12]Present address: Med-X Research Institute and School of Biomedical Engineering, Shanghai Jiao Tong University, Shanghai, China
[13]These authors contributed equally
[14]Lead contact
*Correspondence: yszhang@bwh.harvard.edu
https://doi.org/10.1016/j.cell.2025.11.012

SUMMARY

Conventional hydrogel-based bioprinting methods often suffer from insufficient cell densities, which may limit crucial cell-cell interactions and impair overall tissue functions. Here, we present an approach that modifies cell membranes with acrylate bonds, allowing living cells at physiological densities (up to $\sim 10^9$ cells mL^{-1}) to serve directly as bioinks, demonstrating photoactivated bioprinting through digital light processing using purely cellular bioinks. Our cell-dense bioinks (CLINKs) rapidly produce tissue constructs that closely mimic native tissues, characterized by strong structural relevancy and robust functionality. The high cellularity and living nature of CLINKs enable the creation of advanced biological models such as connected neural circuits and rhythmically contracting mini-hearts derived entirely from stem cells, effectively capturing essential native-like behaviors. Implants created through this method showcase the capacity to integrate with the host, thereby promoting regeneration. Our CLINK technology holds substantial promise in tissue biofabrication, opening alternative avenues for biomedical applications.

INTRODUCTION

Bioprinting is a three-dimensional (3D) biomanufacturing technology used to precisely pattern cells and cell-laden biomaterials (bioinks) to construct volumetric tissues with desired functions.[1–4] Typically, bioinks rely on hydrogel matrices to stabilize and crosslink constructs before, during, or after bioprinting.[5,6] Although such methods have advanced biomimicry, achieving *in vivo*-like cell densities remains challenging. Extensive hydrogel content can hamper cell-cell interactions, triggering phenotype loss and reducing tissue functionality.[7] Consequently, scaffold-free 3D bioprinting has emerged to address these concerns, enabling cells to form dense structures; to closely interact; and, for stem cells, to differentiate to fulfill specialized niches.[8]

Recent efforts have fostered various scaffold-free approaches to create functional tissue mimics.[9,10] For example, pre-aggregated cells can be fused on needle arrays to produce high-cell-density tissues.[11] Early demonstrations formed relatively simple shapes—often tubes of large diameters—owing to the

Please cite this article in press as: Wang et al., Biomaterial-minimalistic photoactivated bioprinting of cell-dense tissues, Cell (2026), https://doi.org/10.1016/j.cell.2025.11.012

limitations of needle-based designs. Alternatively, spheroids can be positioned within self-healing hydrogel baths for controlled spatial distributions,[12] and perfusable vascular channels have been introduced via sacrificial extrusion bioprinting into stem cell-derived aggregates.[13] Meanwhile, the self-organization of stem cells under 3D conditions[14] has enabled organoids that approximate native tissues,[15,16] but they often face reproducibility and size constraints.[17] To this end, the abovementioned bioprinting strategies can assemble these stem cells into continuous patterns—gut tubes,[18] renal organoids,[19] or neuronal tissues[20]—possessing structured tissue functions not quite possible before, or sometimes into somatic cell-dense structures.[21] Nonetheless, such methods, typically relying on extrusion bioprinting, may lack the resolution and complexity required for more intricate tissues.

To overcome the obstacles of structural flexibility in scaffold-free bioprinting and to provide a versatile approach of manipulating cell-dense bioinks, we hypothesized that other than extrusion bioprinting, additional bioprinting modalities such as digital light processing (DLP) might be a preferred option. DLP-based bioprinting can quickly produce 3D constructs featuring complex shapes and internal architectures by layer-by-layer photopolymerization.[3,22–27] Despite its wide application in tissue biofabrication, few reports detail fully cell-dense structures, likely because DLP typically necessitates photocrosslinkable biomaterials to maintain integrity.

Here, we present a unique method using oxidized and methacrylated hyaluronic acid (OMHA) as a linker to modify cell surfaces, enabling direct photocrosslinking of cells in native densities (Figure 1). Conventional hydrogel-based bioinks and scaffold-free fusion approaches suffer from low cell densities, poor cell-cell interactions, or limited structural control, hindering the construction of functional tissues. By contrast, our biomaterial-minimalistic, scaffold-free "cell-dense bioinks" (CLINKs) enable the creation of two-dimensional (2D) and 3D high-cell-density constructs with complex geometries. Using the CLINK technology, we established hepatic models by bioprinting functional liver tissues suitable for both *in vitro* and *in vivo* applications. The same strategy further allowed the construction of physiologically relevant architectures otherwise inaccessible with existing methods, including functional neural circuits and spontaneously contracting mini-hearts each containing a hollow chamber. Finally, we applied CLINKs to generate patterned mesenchymal stem cell/endothelial cell (MSC/EC) implants that recapitulated critical cellular interactions during wound healing, highlighting the broad potential of this approach for engineering diverse, cell-dense tissues.

RESULTS

Characterizations of OMHA-modified biomaterial-minimalistic cellular bioinks

We first confirmed successful OMHA synthesis using proton nuclear magnetic resonance (^{1}H-NMR), revealing characteristic peaks for methacrylation (vinyl protons at 6.16 and 5.73 ppm) and oxidation (aldehyde protons at 8.29 ppm) (Figure S1A). The degree of oxidation was 24.34% as determined by hydrazide titration. Gel permeation chromatography (GPC) analyses revealed that periodate oxidation reduced the hyaluronic acid (HA) molecular weight (MW) while maintaining the narrow dispersity (polydispersity indices [PDIs] from 1.64 to 1.93) (Figure S1B), thereby preventing the formation of heterogeneous oligomers. In assessing the interaction with cells, fluorescein isothiocyanate (FITC)-OMHA imaging showed rapid membrane labeling within seconds, with prolonged exposure increasing OMHA density (Figure S1C). Following DLP photocrosslinking, OMHA modification enabled membrane-localized stable cell anchoring, as evidenced by fluorescence, in contrast to the diffusive extracellular fluorescence surrounding the cells observed in methacrylated HA (HAMA)-based constructs (Figure S1D). The amine-aldehyde coupling reaction between the cell membrane and the linker led to the generation of reactive oxygen species (ROS); however, this mild ROS production did not adversely affect cell viability, as confirmed by live/dead assay (Figure S1E). Additionally, OMHA's rapid reaction kinetics with amine groups under physiological pH enabled swift cell surface modification and formation of stable methacrylate bonds toward efficient photocrosslinking of functionalized cells, unlike a commercial acrylate linker (Figure S1F).

Embryonic stem cells (ESCs) are potent cell sources because of their pluripotency and extensive self-renewal capacity.[28] To investigate the influences of the OMHA linker on cell behavior, we examined key ESC pluripotency factors. As shown in Figure 2A, Sox-2 and Oct 3/4 levels did not differ among unmodified ESCs, OMHA-modified ESCs, or ESCs post-DLP photocrosslinking. The first step of ESC differentiation is embryoid body (EB) formation.[29] We generated EBs with both untreated and linker-modified ESCs (Figure 2B), finding uniform size and shape across all groups with 100% yield (Figure 2C). A quantitative reverse-transcription polymerase chain reaction (RT-qPCR) ScoreCard assay[30] revealed similar self-renewal as well as ectoderm, mesoderm, and endoderm gene expressions on day 7 of EB induction in both conditions (Figures 2D and S1G).

Subsequent neural differentiation produced human cortical organoids (hCOs)[31] of comparable areas (Figures 2E and 2F), with similar neural progenitor and neuronal gene expressions (Figure S1H; primers listed in Table S1). Immunocytochemistry found NeuN$^+$ cells at 33.00% ± 10.89% and 32.98% ± 5.96% for unmodified and OMHA-linked ESCs, respectively (Figures 2G and 2H). Thus, OMHA modification revealed minimal impact on ESC marker expressions, EB formation, or neural differentiation.

We also examined CLINK's rheological properties in NIH/3T3 fibroblasts. The cell suspension and CLINK samples behaved similarly in elastic (G′) and viscous (G″) moduli (Figures 2I–2K). Both components shifted as shear stress or frequency changed, consistent with cytoskeletal viscoelasticity.[32] Overall, OMHA did not affect mechanical properties, indicating cytocompatibility suitable for bioprinting of functional tissues.

Printability evaluations and printing parameter optimizations of CLINK

Next, we optimized CLINK for DLP bioprinting using NIH/3T3 fibroblasts. Compositions varied photoinitiator and photoabsorber levels, crosslinking time, and cell density, with fidelity assessed by printing squares of different dimensions

Please cite this article in press as: Wang et al., Biomaterial-minimalistic photoactivated bioprinting of cell-dense tissues, Cell (2026), https://doi.org/10.1016/j.cell.2025.11.012

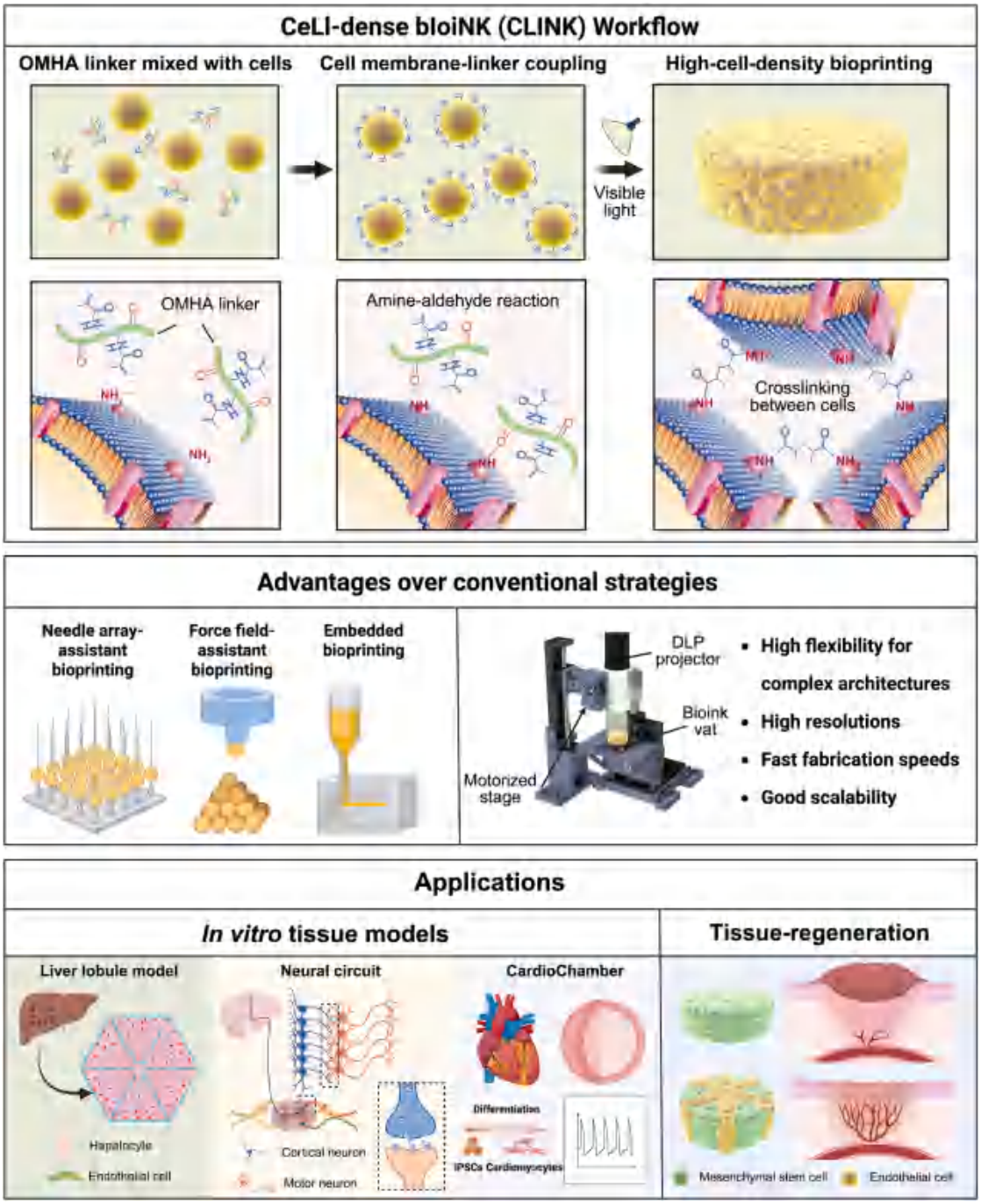

Figure 1. Biomaterial-minimalistic photoactivated DLP bioprinting using CLINK

Top: schematic illustration of the CLINK workflow. OMHA linkers are coupled to cell membranes via the amine-aldehyde reaction, enabling photocrosslinking between cells under light exposure and the fabrication of high-cell-density constructs through DLP bioprinting. Not drawn to scale.

Middle, comparison with conventional strategies, highlighting the advantages of CLINK, including ultrahigh cell density, high flexibility for complex architectures, native-like functionality, and high reproducibility.

Bottom: representative applications of biomaterial-minimalistic DLP-bioprinted tissue models for drug screening and tissues for regenerative medicine, including liver lobules consisting of hepatocytes and ECs, neural circuits containing spatially arranged cortical and motor neuron populations, CardioChambers featuring chambered cardiomyocytes, and MSC/EC-based constructs, are patterned to promote wound healing.

Please cite this article in press as: Wang et al., Biomaterial-minimalistic photoactivated bioprinting of cell-dense tissues, Cell (2026), https://doi.org/10.1016/j.cell.2025.11.012

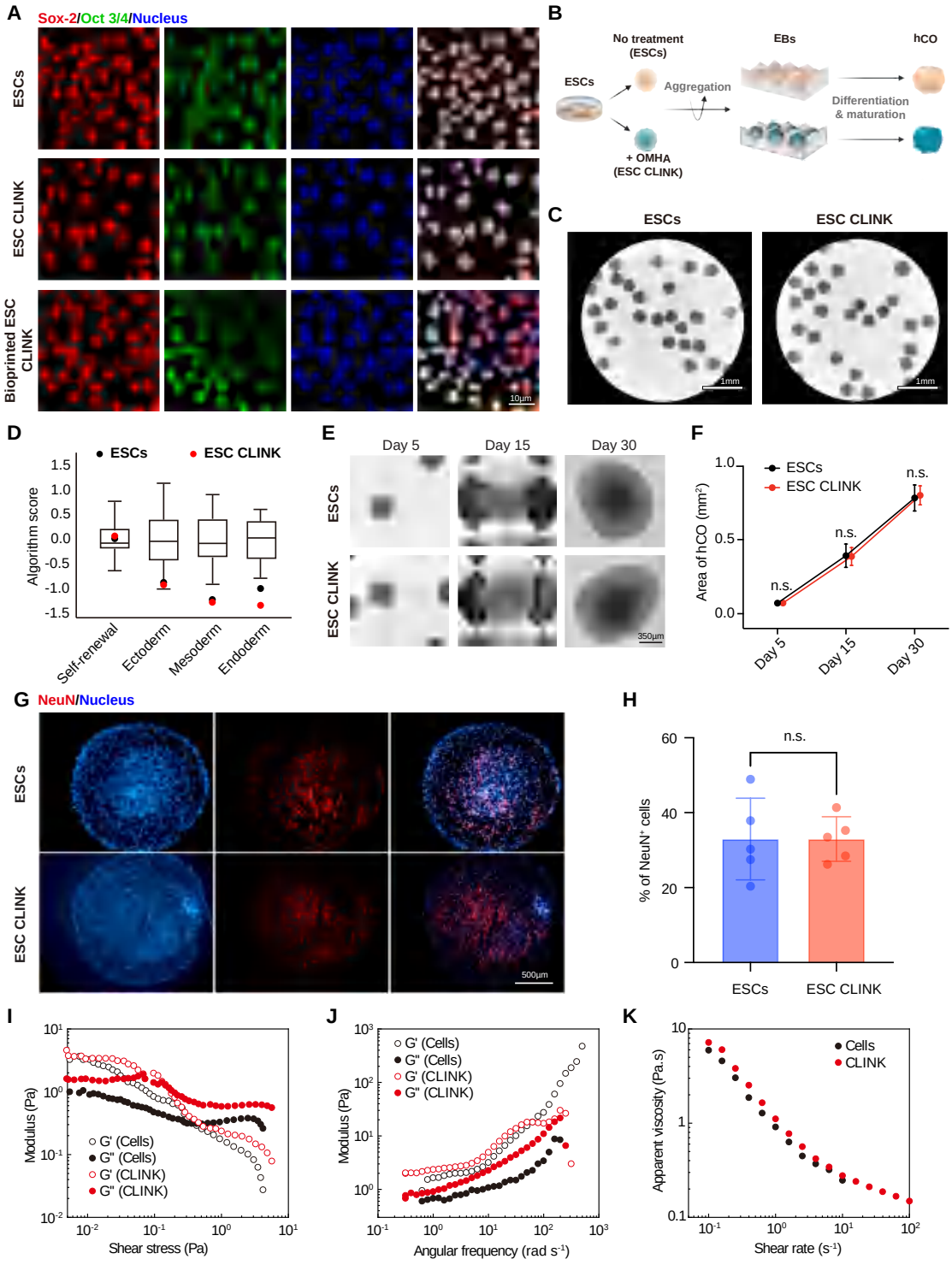

Figure 2. Stem cell behaviors and rheological characterizations of ESC CLINK

(A) Expressions of pluripotency markers Sox-2 and Oct 3/4 of 2D-cultured ESCs, 2D-cultured ESCs functionalized with OMHA, and DLP-photopatterned biomaterial-minimalistic ESCs.

(B) Schematic of EB formation from ESCs and ESC CLINK, using Aggrewell, and their differentiation into hCOs.

(C) Representative images of EBs formed by ESCs or ESC CLINK at day 7.

(D) TaqMan hPSC Scorecard analyses of EBs, with boxplot showing the algorithm scores for four gene classes (self-renewal, ectoderm, mesoderm, and endoderm). The algorithm scores were calculated based on the qPCR values and compared with the expression profiles of nine undifferentiated pluripotent stem

(legend continued on next page)

Please cite this article in press as: Wang et al., Biomaterial-minimalistic photoactivated bioprinting of cell-dense tissues, Cell (2026), https://doi.org/10.1016/j.cell.2025.11.012

(0.25 × 0.25 to 1.75 × 1.75 mm^2). A photoinitiator system of 0.5/5 mM tris(2,2-bipyridyl)dichlororuthenium(II) hexahydrate (Ru)/sodium persulfate (SPS) and 1 w/v% Ponceau 4R photoabsorber consistently yielded good shape fidelity (Figures 3A and S2A). At above 1.5 w/v% photoabsorber, smaller squares were under-crosslinking, whereas raising Ru/SPS above 0.5/5 mM caused over-curing (Figure S2B). Exposure durations from 2 to 8 s produced up to 153.85 μm of layer thickness, with shorter exposures failing to solidify the patterns (Figure S2C). Critically, densities of up to 10^9 cells mL^{-1} (i.e., nearly pure cells) remained printable with intact structures (Figure S2D). Cell viability was high across various light intensities and curing durations (Figure S2E), further verifying the cytocompatibility of CLINK.

Biomaterial-minimalistic DLP-bioprinted sophisticated structures with high cell densities

To illustrate CLINK's versatility in DLP bioprinting, we began by fabricating an array of geometric patterns by using fluorescently labeled NIH/3T3 CLINK with our customized top-down DLP systems (Figures S3A and S3B). As an example, a scaffold-free logo as well as patterns measuring fine features of 200 μm in line width was bioprinted within 5 s (Figures 3B, S3C, and S3D). We also generated multi-cell-type designs, including mosaic assemblies and stromal heterogeneities (Figures 3C, S3E, and S3F), and combined NIH/3T3 fibroblasts, human umbilical vein ECs (HUVECs), and smooth muscle cells (SMCs) into a single construct (Figure S3G). These findings highlight our method's capacity for patterning densely packed, heterogeneous cells in sophisticated forms.

Because cell-dense, multi-cell-type structures are vital for modeling complex biological interactions, we bioprinted an alveolus-like tissue by utilizing the CLINK of A549 adenocarcinomic human alveolar basal epithelial cells surrounded by that of human lung microvascular ECs (HLMECs) (Figure 3D). We also mimicked vascular walls by bioprinting SMCs alongside HUVECs (Figure S3G). As a tumor microenvironment example, a HUVEC-derived capillary-like pattern was embedded into MDA-MB-231-rich stroma (Figure 3E), achieving clear boundaries without noticeable mixing of CLINK formulations.

To prevent potential disassembly of the biomaterial-minimalistic, scaffold-free bioprinted constructs due to slightly weaker early cell-cell interactions supported only by OMHA and the dynamic cell membrane, a 0.25 w/v% alginate layer was applied immediately post-bioprinting (Figure S4A). Once sufficient cell-cell contacts formed, usually within 1 day, alginate was removed with 0.01 M ethylenediaminetetraacetic acid disodium (EDTA) solution.[33] By day 3, cells remained densely packed, and HUVECs showed a spreading morphology (Figure 3E). Some degree of detachment arose when the cells grew over-confluent within the bioprinted confined volumes (Figure S4B), and raising alginate to 1.00 w/v% caused partial cell death on day 1 (Figures S4C–S4E). At lower initial cell densities, the structures stayed stable throughout the culture period (Figures S5A–S5C). Despite occasional detachments, most cells retained high viabilities and metabolic activities for 14 days using biomaterial-minimalistic DLP bioprinting (Figures S5D–S5F). As a direct control, constructs produced using HAMA as the linker failed to support bioprinting at densities beyond 1 × 10^8 cells mL^{-1} or to sustain equally good cellular activities post-bioprinting, even at reduced cell densities where structural integrity could be retrained (Figure S5G).

Beyond 2D or pseudo-3D layers, we achieved true 3D fabrication using NIH/3T3 CLINK, by projecting sliced images as the build platform moved downward (Figures S3A and S3B). At 100-μm layer thickness and 5 s of exposure per layer, we bioprinted a cell-dense, translucent 3D pyramid (Figure S5H), illustrating CLINK's capacity to form complex, high-cell-density architectures beyond the capacity of conventional hydrogel-rich DLP bioprinting. We also created 3D constructs with hollow, branched channels (Figures 3F and S5I–S5L). A main 800-μm channel split into two 500-μm branches, with filamentous actin (F-actin) staining (horizontal and cross-sectional views) and hematoxylin and eosin (H&E) staining confirming high cell densities along the walls. Dye perfusion revealed channel patency, underscoring the potential for biomaterial-minimalistic bioprinting of vascular or tubular tissues.

Moreover, we demonstrated multi-material 3D bioprinting by sequentially switching the CLINK bioinks.[34] A voxelated construct with precise spatial organization of the cell populations was patterned layer by layer, with NIH/3T3 CLINKs labeled in different colors (Figures 3G and S5M). We also embedded hollow channels in a multi-material design, positioning green- and red-labeled fibroblasts in designated regions (Figure 3H). Unlike extrusion methods reliant on aggregates or sacrificial supports, this layer-by-layer approach enables rapid, high-resolution fabrication of intricate planar and volumetric patterns, accommodating virtually any cell type or combination.

Structures and functions of biomaterial-minimalistic DLP-bioprinted hepatic tissues

We next assessed cell viability in NIH/3T3 CLINK constructs after DLP bioprinting. Compared with biomaterial-rich bioinks (e.g., 5, 10, or 15 w/v% GelMA with NIH/3T3 cells),[35,36] only CLINK supported physiologically relevant high cell densities with minimal cell death (Figures S6A and S6B). A 3-(4,5-dimethylthiazol-2-yl)-5-(3-carboxymethoxyphenyl)-2-(4-sulfophenyl)-2H-tetrazolium (MTS) assay confirmed that cells in scaffold-free CLINK constructs maintained high metabolic activities for up to 5 days, which we evaluated (Figure S6C).

cell lines in the reference set. Scores close to 0 indicate similarity to the reference set, and scores higher than 1 suggest upregulation, or less than −1 suggest downregulation relative to the reference set.

(E and F) Representative images of hCOs differentiated from ESCs and ESC CLINK at days 5, 15, and 30 (E) and corresponding quantified areas of hCOs (F).

(G and H) Images of NeuN (red) and corresponding quantification of $NeuN^+$ cell percentages in ESC-derived and ESC CLINK-derived hCOs at day 75.

(I–K) Elastic modulus, viscous modulus, and viscosity characterizations of NIH/3T3 and NIH/3T3 CLINK.

See also Figure S1.

Data are means ± SDs. n.s., non-significant difference.

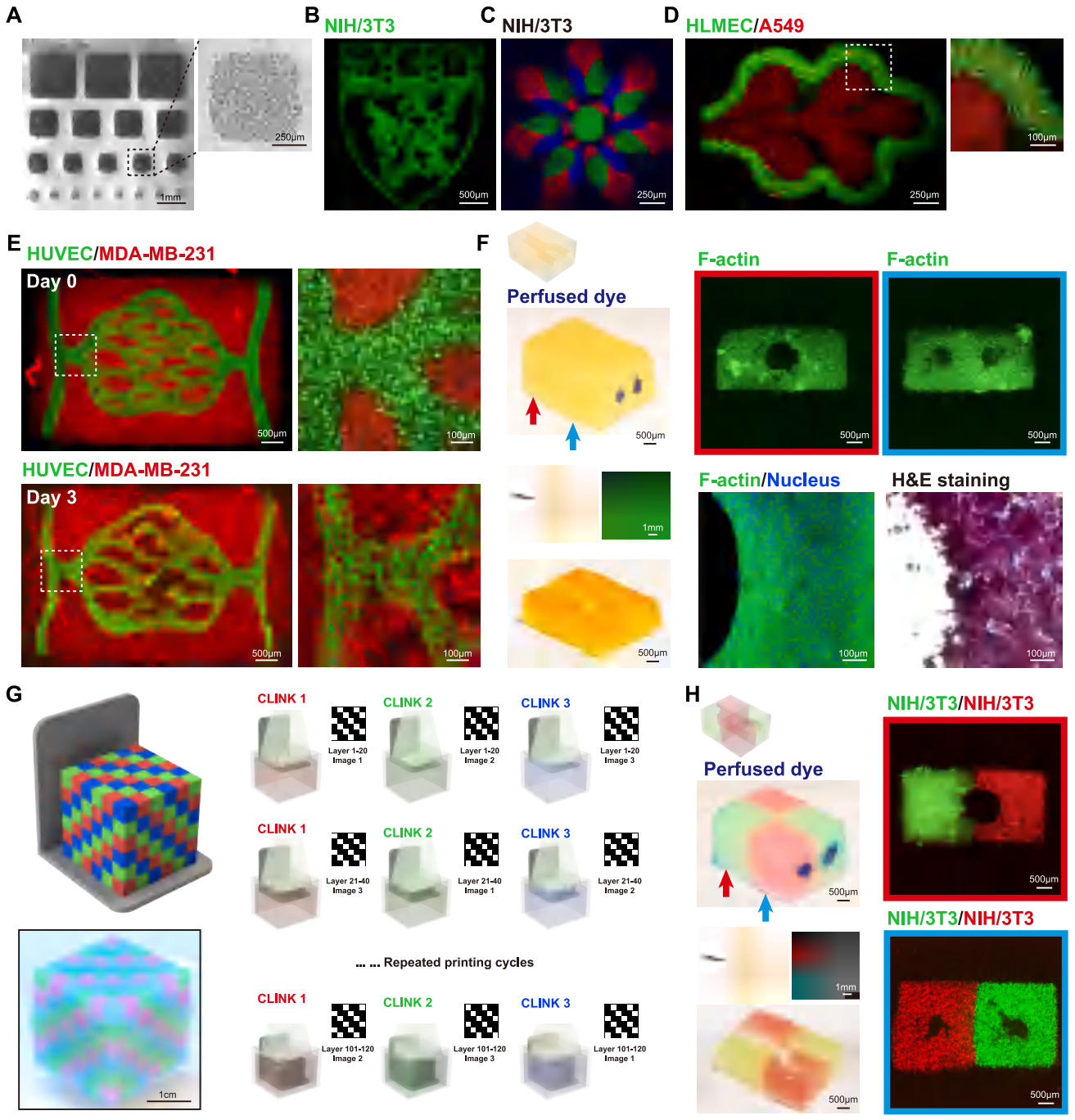

Figure 3. Biomaterial-minimalistic DLP bioprinting of CLINKs into sophisticated architectures with high cell densities and high resolutions

(A) Printing resolution and fidelity optimizations via photoabsorber. All square patterns were projected simultaneously with multiple sizes and replications, using the NIH/3T3 CLINK containing 0.50/5.00 mM Ru/SPS and 1 w/v% photoabsorber. Zoomed-in image of the bioprinted square illustrates the high cell density within the bioprinted biomaterial-minimalistic structure.

(B–D) Biomaterial-minimalistic bioprinting of sophisticated structures with CLINKs of single or multiple cell types.

(B) Logo consisting of fluorescently labeled NIH/3T3 fibroblasts (green).

(C) Multi-cell-type floral mosaic consisting of fluorescently labeled NIH/3T3 fibroblasts (red, green, and blue).

(D) Pulmonary alveolus-like tissue consisting of fluorescently labeled A549 cells (red) and HLMECs (green).

(E) Biomaterial-minimalistic bioprinting of breast cancer model using CLINKs of fluorescently labeled MDA-MB-231 breast cancer cells (red) and GFP-HUVECs (green) on days 0 and 3.

(legend continued on next page)

Please cite this article in press as: Wang et al., Biomaterial-minimalistic photoactivated bioprinting of cell-dense tissues, Cell (2026), https://doi.org/10.1016/j.cell.2025.11.012

Given the limitations of animal models in predicting drug efficacy and toxicity,[37–39] we leveraged our biomaterial-minimalistic DLP strategy to bioprint hepatic tissues at physiological densities. HepG2/C3A CLINK constructs ($\sim 1 \times 10^9$ cells mL^{-1}) were patterned into a lobule-like architecture within 10 s. Live/dead staining showed high viability values from days 1 to 3 (Figure S6D), with the lobule spaces narrowing as HepG2/C3A cells proliferated. We also produced multi-cell-type liver constructs with red CellTracker-labeled HepG2/C3A and green fluorescent protein-expressing HUVECs (GFP-HUVECs), by first bioprinting the HUVEC CLINK in a sinusoidal network, rinsing away uncrosslinked cells, and then bioprinting the HepG2/C3A CLINK (Figures 4A and S6E). Although ultrahigh densities and proliferation caused some detachments after 7 days (Figure S7A), overall viabilities remained strong.

We then compared biomaterial-minimalistic liver tissues with conventional biomaterial-rich ones. GelMA-based bioinks, often used for hepatocytes, typically limit cell density (e.g., maximum $\sim 8 \times 10^6$ cells mL^{-1}) to avoid scattering and interference with photocrosslinking.[40,41] In contrast, our HepG2/C3A CLINK reached $\sim 1 \times 10^9$ cells mL^{-1}, two orders of magnitude higher than that traditionally attainable with GelMA-rich bioink. As with NIH/3T3 fibroblasts, hepatic cell death mainly occurred in GelMA-based constructs from days 1 to 3 (Figures 4B, 4C, and S6E). By contrast, scaffold-free CLINK constructs retained high viability values. Metabolic evaluations confirmed that both single- and multi-cell-type biomaterial-minimalistic liver tissues proliferated robustly through day 5, unlike the GelMA-rich group (Figure 4C). Slightly lower viability at day 1 (Figure 4B) likely stemmed from potential photoinitiator/photoabsorber exposure or radicals. We used cytocompatible Ru/SPS and Ponceau 4R[22,24] and washed the constructs to remove the potentially harmful radical species as much as possible. Nevertheless, radical-free crosslinking methods might further improve cell viability.[42]

To evaluate liver-specific functions, we performed immunostaining on day 7. As seen from the unnormalized immunostaining quantifications, GelMA-based liver tissues displayed the lowest albumin (ALB), E-cadherin, cytochrome P1A2 (CYP1A2), and CYP3A4 levels (Figures 4D, 4E, and S7B–S7D). Conversely, biomaterial-minimalistic, high-density constructs showed stronger signals, especially in co-cultures with HUVECs. Gene expression analyses also revealed elevated liver biomarkers, including *ALB* and alpha fetoprotein (*AFP*) but higher caspase 8 (*CASP8*) in high-density constructs (Figure S7E), possibly linked to localized cell death over longer culture. These findings align with previous multi-cell-type liver models in which cell-cell interactions enhance phenotypic maintenance.[43] Enzyme-linked immunosorbent assay (ELISA) further confirmed greater ALB secretion in biomaterial-minimalistic tissues than in GelMA controls, with the highest levels in HepG2/C3A plus HUVEC co-cultures at day 10 (Figure S7F), facilitating better understanding of the hepatic biology and drug screening studies.

We next examined how perfusable channels might benefit 3D or 2D liver tissues bioprinted with either GelMA laden with HepG2/C3A cells ($\sim 8 \times 10^6$ cells mL^{-1}) or HepG2/C3A CLINK ($\sim 1 \times 10^9$ cells mL^{-1}) (Figure S7G). In bulk 3D constructs ($10 \times 8 \times 6$ mm^3), lower cell survival and functions were observed at higher densities without channels. However, ALB and AFP levels rose significantly in branched-channel constructs (Figure S7H). In 2D structures, nutrient diffusion was already sufficient, so channels provided fewer benefits. Altogether, the presence of specific patterns such as perfusable channels, as enabled by bioprinting, might promote the physiological functions of the biomaterial-minimalistic 3D liver tissues across the longer-term culture, compared with those without channels, 2D in nature, as well as of lower cell densities.

Creating engineered tissue models can be particularly challenging when large numbers of functionally identical replicates are required in a higher-throughput manner, where good reproducibility is essential to ensure consistent biological performance. We showed simultaneous bioprinting of 15 hepatic lobule patterns (each 2 mm in diameter, minimum size attainable) in one 10-s exposure (Figures 4F, 4G, and S7I). A total of 45 lobules in 15 experimental groups could be tested at once, forming a "liver chip" platform suitable for drug screening. As a demonstration, we treated these cell-dense tissues with doxorubicin (DOX) at various concentrations (0–100 μM). Cell viability (measured by CellTiter-Glo 3D) decreased in both concentration- and time-dependent manners (Figure 4H), corroborated by morphological changes under bright-field imaging (Figure S7J). The medium-throughput liver chip provided an appropriate tool featuring natural-like cell density for hepatic tissue and disease modeling as well as toward screening of therapeutic and other agents.

To further assess the *in vivo* functionality of bioprinted liver tissues, we transplanted four different constructs, GelMA only, GelMA containing HepG2/C3A cells, CLINK without channels, and CLINK with channels, into the mesenteric parametrial region of mice (Figure 4I). At 1 week post-transplantation, all implanted samples retained their structures, demonstrating the stability of high-cell-density constructs (Figure 4J). To evaluate the physiological relevance of these implants, we measured the activities of CYP3A4, a key indicator of hepatic metabolism and functions

(F) Biomaterial-minimalistic bioprinting of 3D cell-dense constructs containing a bifurcation geometry using CLINK of NIH/3T3 fibroblasts. These constructs were cut open in different ways for better visual illustrations. Images show F-actin staining (green) with top and cross-sectional views, where enlarged views of F-actin and H&E staining are also supplied. Red and blue lines/arrows/frames indicate the positions where cross-sections were cut. Channel irregularities were due to cutting artifacts.

(G) Multi-material biomaterial-minimalistic bioprinting of a 3D cell-dense voxelated construct using CLINK of labeled NIH/3T3 fibroblasts (green, red, and blue). Schematics on the right display the bioprinting process.

(H) Multi-material biomaterial-minimalistic bioprinting of 3D cell-dense constructs containing a bifurcation geometry using CLINKs of fluorescently labeled NIH/3T3 fibroblasts (green and red). These constructs were cut open in different ways for better visual illustrations. Images show top and cross-sectional views. Red and blue lines/arrows/frames indicate the positions where cross-sections were cut. Channel irregularities were due to cutting artifacts.

See also Figures S2, S3, S4, and S5.

Please cite this article in press as: Wang et al., Biomaterial-minimalistic photoactivated bioprinting of cell-dense tissues, Cell (2026), https://doi.org/10.1016/j.cell.2025.11.012

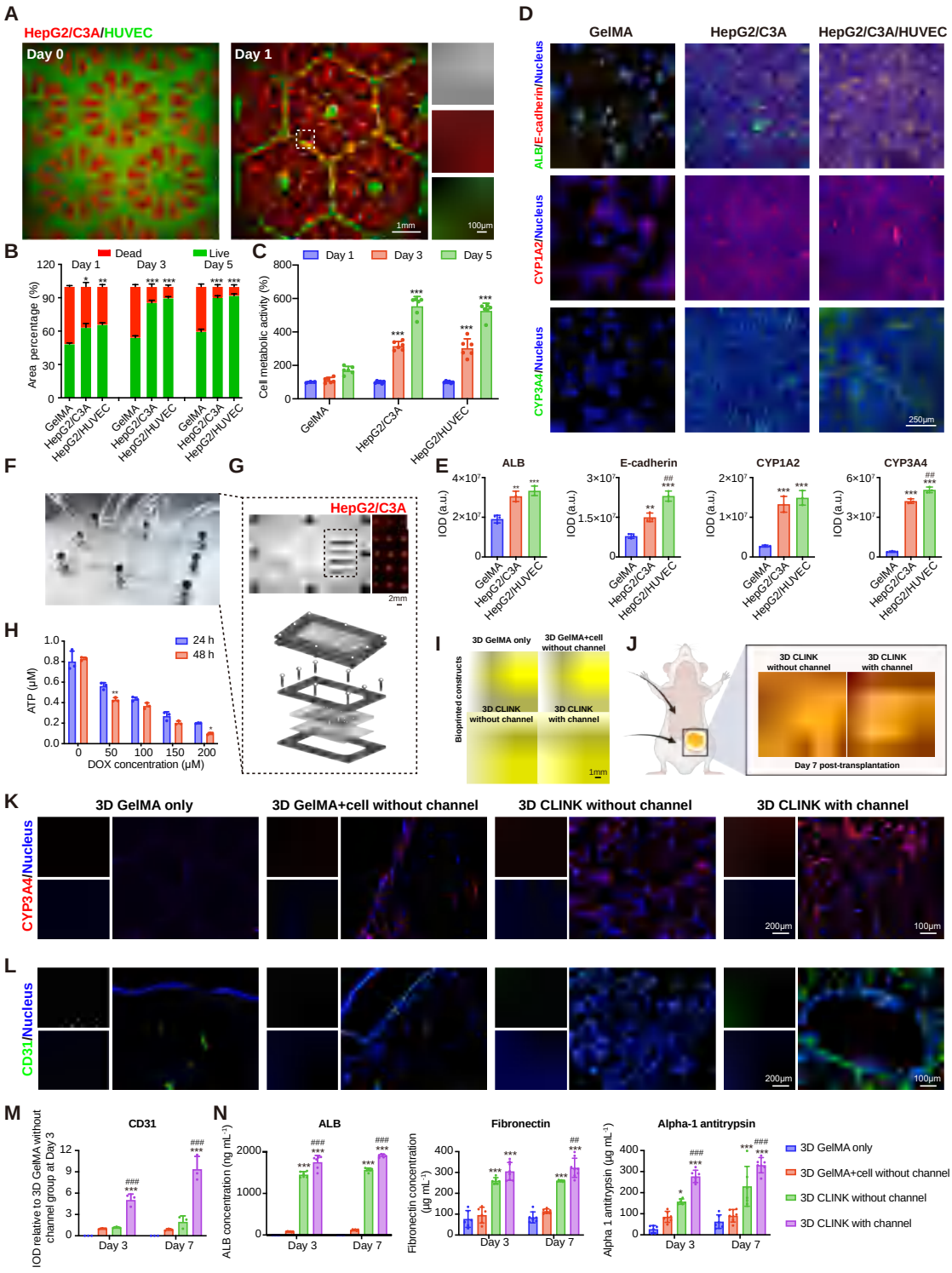

Figure 4. Biomaterial-minimalistic DLP bioprinting of cell-dense hepatic tissues

(A) Bioprinted biomaterial-minimalistic hepatic lobule structures with high densities of fluorescently labeled HepG2/C3A cells (red) and GFP-HUVECs (green) on days 0 and 1.

(B) Quantitative analyses of percentages of live/dead fluorescence areas based on the results of live (green)/dead (red) staining of bioprinted HepG2/C3A cells in 10 w/v% GelMA hydrogel, and HepG2/C3A cells or HepG2/C3A cells plus HUVECs in biomaterial-minimalistic cell-dense constructs on days 1, 3, and 5.

(C) Quantitative results of MTS assay showing metabolic activities of bioprinted hepatic tissues.

(legend continued on next page)

Please cite this article in press as: Wang et al., Biomaterial-minimalistic photoactivated bioprinting of cell-dense tissues, Cell (2026), https://doi.org/10.1016/j.cell.2025.11.012

(Figures 4K and S7K). CYP3A4 showed significantly higher activities in the CLINK constructs, compared with the other groups, suggesting improved metabolic capacity.

A well-established vascular network is essential for rapid integration of implants with host tissues. Accordingly, we assessed their neovascularization as early as day 7 post-transplantation. Immunofluorescence staining confirmed mouse CD31 expressions in CLINK constructs, particularly those containing channels, suggesting that the channel structure promoted EC migration and guided neovessel formation (Figures 4L, 4M, and S7K). In addition, we detected substantial levels of human ALB, fibronectin, and alpha-1 antitrypsin in the serum of mice transplanted with CLINK constructs, especially those incorporating channels (Figure 4N). Overall, the CLINK constructs bioprinted with channels not only demonstrated robust integration of hepatic functionality into the host animals but also facilitated rapid neovascularization *in vivo*, well beyond the performances of the conventional constructs containing low densities of hepatocytes.

Neural circuit and CardioChamber models via biomaterial-minimalistic DLP bioprinting

Microcircuits of the nervous system consist of sophisticated connections among multiple neurons. Constructing *in vitro* neuronal circuits that replicate these distinct architectures can greatly advance our understanding of neuronal interactions and connectivity under both physiological and pathological conditions.[44] Although earlier devices have segregated neurons within designed structures,[45] we instead leveraged our CLINK-based, scaffold-free DLP bioprinting to create spatially defined compartments at high neuronal densities, aiming to produce a 3D cortico-motor circuit rapidly.

To accomplish this, we first derived cortical and motor neurons using the neurogenin 2 (NGN2)-overexpression method (Figure 5A).[46,47] The CLINK ($\sim 1 \times 10^9$ cells mL^{-1}) of each neuron type was bioprinted sequentially in designated areas in a typical cortico-motor layout (Figure 5B). Tuj1 staining suggested that both CLINK-bioprinted and conventionally plated neurons developed neurite outgrowths at day 7 (Figures S8A and S8B); however, in plating cultures, neurites were randomly oriented (Figure S8A). In contrast, the bioprinted neurons, immediately confined to their respective areas, grew at high density (Figure 5C). Of significance, Tuj1-staining at day 7 confirmed axonal extensions spanning between these regions (Figures 5D, 5E, and S8B). Both cortical and motor neurons projected robust axons into adjacent compartments (Figure 5D). Immunofluorescence for calcium-calmodulin (CaM)-dependent protein kinase II (CaMKII; cortical) and ISL LIM homeobox 1 (Isl-1; motor) revealed that most neurons remained in their intended areas, although 5.22% ± 1.77% of motor and 11.07% ± 1.14% of cortical neurons were found elsewhere (Figures 5F, S8C, and S8D). By comparison, hCOs and spinal organoids (hSpOs) required up to 80 and 45 days, respectively, to exhibit similar cell types (Figures S8E–S8G), along with noticeable structural variations. Meanwhile, the same neurons failed to survive in a traditional GelMA-rich bioink (~81.34% ± 2.11% cell death within 3 days) (Figure S8H and S8I). Thus, our CLINK-based bioprinting produces these neurons at high densities with viable axonal connections in 3D, essential for reproducing neuronal communications observed *in vivo*.

We then tested whether the dense cortico-motor circuit formed functional connections by employing optogenetics and micro-electrode array (MEA) recordings (Figure 5G). A channelrhodopsin-2 (ChR2) construct was delivered to cortical neurons via an adeno-associated virus. Motor and ChR2-cortical neurons were bioprinted into two separate regions on an MEA plate. Under the CaMKII::ChR2-mCherry promoter, only cortical neurons expressed ChR2, localized in their designated area (Figure 5H). After 7 days, we stimulated these neurons with brief (100-ms) pulses of blue light (485 nm) using a custom optical device (Figure 5I). Although few spontaneous firings occurred before stimulation, pulsed light induced a burst of firing activities (Figures 5I and 5J). Notably, the neuronal activities were recorded not only in cortical but also in motor compartments, confirming functional circuit formation. Raster plots revealed that

(D) Confocal immunofluorescence micrographs illustrating staining results for ALB (green) and E-cadherin (red) or CYP1A2 (red) or CYP3A4 (green), with nucleus counterstaining (blue) of the cells in the bioprinted HepG2/C3A cells in 10 w/v% GelMA hydrogel, and HepG2/C3A cells or HepG2/C3A cells plus HUVECs in biomaterial-minimalistic cell-dense constructs on day 7.
(E) Corresponding quantitative analyses of IOD values of ALB, E-cadherin, CYP1A2, and CYP3A4.
(F–H) Medium-throughput drug screening using biomaterial-minimalistic bioprinted cell-dense hepatic tissues.
(F) Photographs of the medium-throughput liver chip showing the capacity of loading multiple drugs or doses.
(G) Fluorescence image presenting a simultaneously bioprinted array of hepatic lobules. Schematic illustrates assembly of the medium-throughput chip.
(H) Plot depicting cell viability results of DOX toxicity to the bioprinted hepatic tissues in the medium-throughput chip.
(I and J) Bioprinted hepatic tissues with 10 w/v% GelMA only, 10 w/v% GelMA laden with HepG2/C3A cells ($\sim 8 \times 10^6$ cells mL^{-1}), and CLINK of HepG2/C3A cells ($\sim 1 \times 10^9$ cells mL^{-1}) without or with perfusable bifurcation channels (I), and micrographs showing hepatic tissues on day 7 post-implantation (J).
(K–M) Immunofluorescence micrographs illustrating staining results for CYP3A4 (red) (K) and CD31 (green) (L), with nucleus counterstaining (blue) of the constructs on day 7 post-implantation. (M) Corresponding quantitative analyses of CD31 IOD values relative to the group of GelMA only without channel at day 3 post-implantation.
(N) Quantitative results of ALB, fibronectin, and alpha-1 antitrypsin secretion levels in serum of mice receiving the hepatic tissues on days 3 and 7 post-implantation.
Data are means ± SDs. In (B), $n = 3$; one-way ANOVA; $^*p < 0.05$, $^{**}p < 0.01$, $^{***}p < 0.001$ (compared with the group of GelMA). In (C), $n = 3$–6; two-way ANOVA; $^{***}p < 0.001$ (compared with the group of GelMA). In (E), $n = 3$; one-way ANOVA; $^*p < 0.05$, $^{**}p < 0.01$, $^{***}p < 0.001$ (compared with the group of GelMA); $^{\#\#}p < 0.01$ (compared with the group of HepG2/C3A). In (H), $n = 3$; one-way ANOVA; $^*p < 0.05$, $^{**}p < 0.01$, $^{***}p < 0.001$ (compared with the group of 24 h). In (M), $n = 3$; two-way ANOVA; $^{***}p < 0.001$ (compared with the group of 3D GelMA+ cells without channel at the same time point); $^{\#\#\#}p < 0.001$ (compared with the group of 3D CLINK without channel at the same time point). In (N), $n = 6$; two-way ANOVA; $^*p < 0.05$, $^{***}p < 0.001$ (compared with the group of 3D GelMA+ cell without channel at the same time point); $^{\#\#}p < 0.01$, $^{\#\#\#}p < 0.001$ (compared with the group of 3D CLINK without channel at the same time point).
See also Figures S6 and S7.

Please cite this article in press as: Wang et al., Biomaterial-minimalistic photoactivated bioprinting of cell-dense tissues, Cell (2026), https://doi.org/10.1016/j.cell.2025.11.012

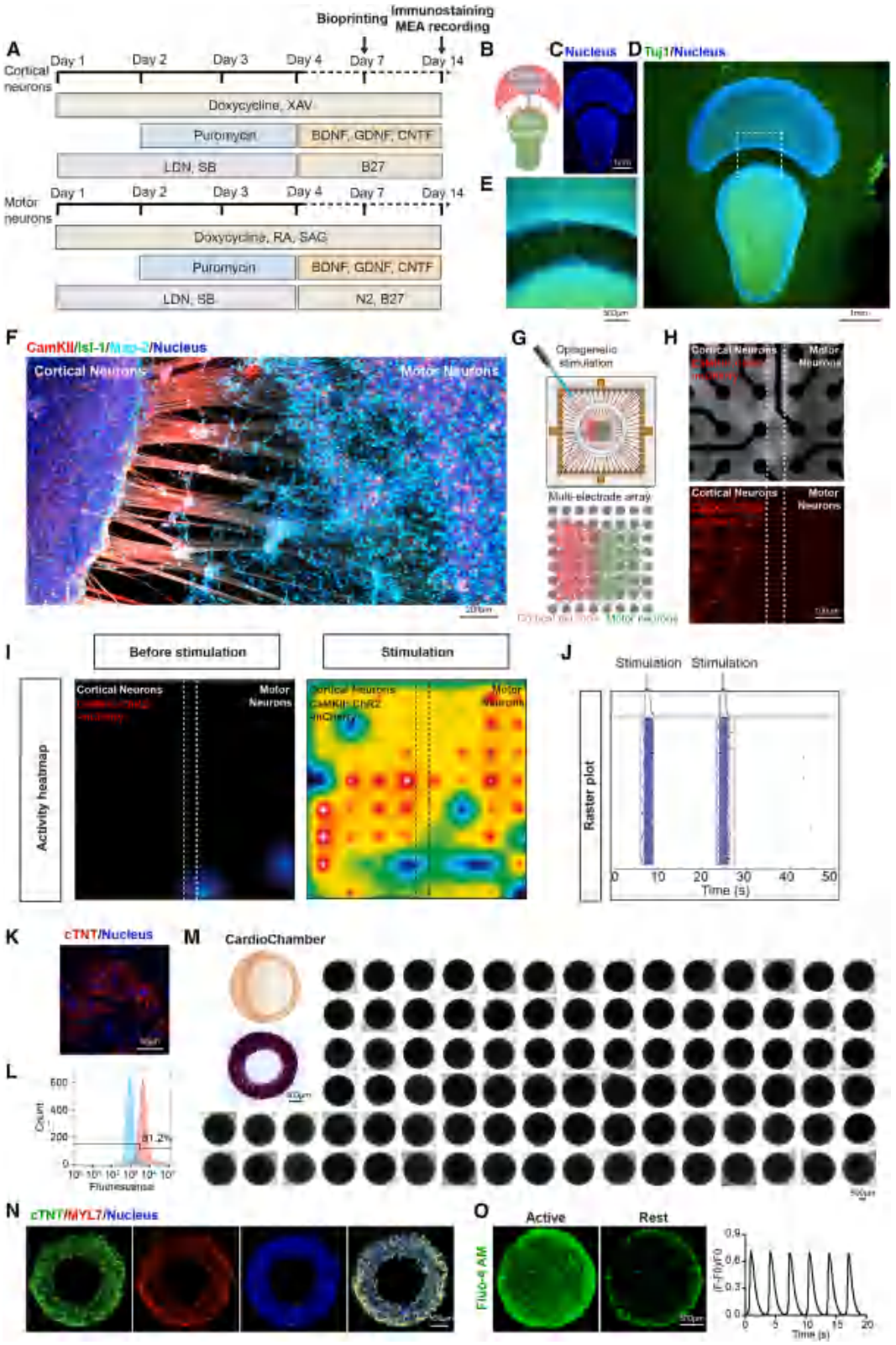

(legend on next page)

Please cite this article in press as: Wang et al., Biomaterial-minimalistic photoactivated bioprinting of cell-dense tissues, Cell (2026), https://doi.org/10.1016/j.cell.2025.11.012

neuronal bursts were time-locked to the optogenetic stimulus (Figure 5J). These results revealed that the bioprinted, high-density neurons established functional connectivity once corticomotor neurites converged.

On the other hand, cardiovascular diseases remain a leading cause of mortality, underscoring the need for robust *in vitro* cardiac models.[48] We therefore bioprinted 3D "CardioChambers" containing human induced pluripotent stem cell (iPSC)-derived cardiomyocytes (hCMs). The hCMs, which had high purity and strong cardiac troponin T (cTnT) expression (Figures 5K and 5L), formed a chambered tissue after each bioprinting procedure (Figure 5M). Of note, we produced 90 CardioChambers (each in ~4 min), all with consistent diameters and clearly defined chambers (Figure 5M). After 7 days, sectioning and staining for cardiac-specific myosin (Myl7) and cTnT showed the persistence of cardiac phenotypes (Figure 5N). Also, remarkably, fully synchronous beatings began within 2 days of culture, indicating functional intercellular connectivity. By day 7, strong spontaneous contractions were observed (Video S1), further validated by calcium-flux measurements (Figure 5O; Video S1). Hence, this CardioChamber model remained structurally intact and preserved key biological attributes of the native cardiac tissue, offering a powerful alternative platform for cardiovascular research and potential therapeutic discovery.

Wound healing via biomaterial-minimalistic DLP bioprinting of MSC/EC CLINKs

To explore the potential of CLINK biomaterial-minimalistic DLP bioprinting in regenerative medicine, we used a mouse dorsal skin-excisional wound model to evaluate how these bioprinted constructs affect wound closure and skin regeneration. GelMA scaffolds containing human MSCs (~8×10^6 cells mL^{-1}, GM-MSC group) were bioprinted, while MSC CLINK (~1×10^9 cells mL^{-1}) was produced via biomaterial-minimalistic DLP bioprinting, either without or with EC inclusion (MSC or MSC/EC group, respectively) (Figure 6A). In addition, EC-CLINK was bioprinted into a radially aligned structure (RAS) designed to mimic the vascular-paving architecture (MSC/EC-RAS group). This radially distributed vascular pattern has shown substantial promise for directing cell migration and promoting wound healing.[49] The constructs were implanted into dorsal skin wounds in mice, and their wound-closure performances were compared with untreated controls (Figure 6B, control group).

Macroscopic observations and wound-trace analyses revealed substantially faster wound closures in groups treated with biomaterial-minimalistic DLP-bioprinted constructs (Figures 6C and 6D). On day 3, the MSC-CLINK group achieved a wound-closure ratio of 40.59% ± 1.00%, significantly higher than the 18.92% ± 3.79% seen in the GelMA-MSC group and 18.11% ± 8.58% in the control groups. By day 7, wounds were only 45.72% ± 5.29% or 32.04% ± 4.90% of their original sizes in the MSC-CLINK or MSC/EC-CLINK-treated mice, respectively, compared with 68.00% ± 2.07% in GelMA-MSC and 68.41% ± 6.62% in the control. Notably, MSC/EC-RAS closed 65.97% ± 15.90% of the wounds by day 3 and 82.49% ± 2.06% by day 7. By day 14, all mice receiving CLINK-bioprinted constructs reached complete wound closure.

During skin regeneration, the epithelium develops an epithelial layer moving inward from the wound edge. We accordingly analyzed re-epithelialization using histological staining, which confirmed enhanced epithelial coverage in all CLINK-treated groups (Figures 6E, 6F, and S9A). Adding ECs improved day-7 coverage, reaching 69.37% ± 4.17% in the MSC/EC-CLINK group and 76.10% ± 3.48% in the MSC/EC-RAS group, ultimately achieving 100% re-epithelialization before day 14. These results highlight the regenerative potential of bioprinted high-cell-density constructs that incorporate multiple cell types and spatial organization. Additionally, CD31 staining revealed that

Figure 5. Biomaterial-minimalistic DLP bioprinting of cell-dense neural circuits and CardioChambers

(A) Schematic showing cortical and motor neuron-development through NGN overexpression; delivery of ChR2 specifically into cortical neurons; as well as biomaterial-minimalistic bioprinting of neuron CLINKs, immunostaining, MEA-recording.

(B–E) Biomaterial-minimalistic bioprinting of cell-dense cortical neurons and motor neurons.

(B) Pattern designed for bioprinting the neural circuit consisting of the top region of cortical neurons and the bottom area of motor neurons, modeling the circuit between the brain and the spinal cord.

(C) Bioprinted neural circuit showing densely allocated neuron nuclei and initial disconnection between the two regions.

(D) Fluorescence micrograph showing Tuj1 (green) staining at day 7 post-bioprinting, presenting axonal extensions of neurons.

(E) Enlarged image indicating process formation between cortical and motor neuron regions.

(F) Immunofluorescence micrograph showing cortical and motor neurons stained with CamKII (red) and Isl-1 (green), respectively, as well as dendrites stained with Map-2 (light blue).

(G) Setup of optogenetic stimulation for the bioprinted cell-dense neural circuit cultured directly in the MEA plate, where cortical neurons were bioprinted in the left region and motor neurons were bioprinted in the right area.

(H) Bright-field micrograph showing the bioprinted cell-dense neural circuit cultured for 7 days in the MEA plate. The expression of ChR2 (red) was detected only in cortical neurons.

(I and J) Firing activities of the bioprinted cell-dense neural circuit illustrated in the activity heatmap (I) before or under optogenetic stimulation, as well as in the raster plot obtained at randomly selected time points (J).

(K) Fluorescence micrograph showing cTNT staining (red) of differentiated hCMs.

(L) Flow cytometry results of differentiated hCMs, measuring the number of cells that express cTnT. Blue indicates isotype control, while red indicates stained cells.

(M) Bright-field micrographs showing 90 replicates of cell-dense CardioChambers at 3 days after biomaterial-minimalistic bioprinting. Inset shows an H&E-stained cross-section of a representative CardioChamber.

(N) Immunofluorescence micrographs showing staining of cTNT (green) and MYL7 (red) in the CardioChambers at 7 days after bioprinting.

(O) Representative calcium images of CardioChambers stained with the Ca^{2+} indicator Fluo-4 AM at active and resting stages, where the synchronized contractions are shown by normalized calcium-flux intensities relative to the Ca^{2+} transient intensities (F-F0)/F0.

See also Figure S8.

Please cite this article in press as: Wang et al., Biomaterial-minimalistic photoactivated bioprinting of cell-dense tissues, Cell (2026), https://doi.org/10.1016/j.cell.2025.11.012

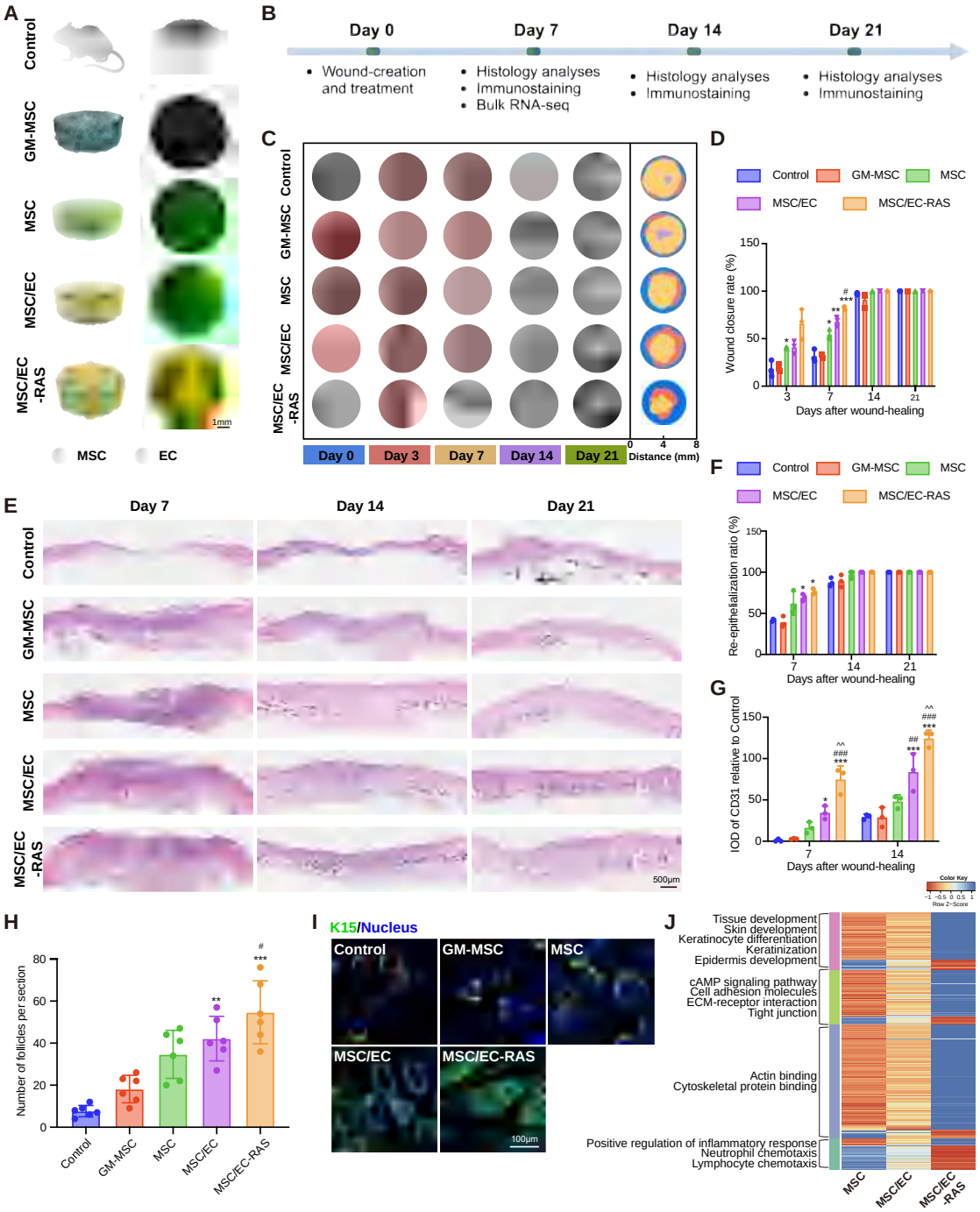

Figure 6. Biomaterial-minimalistic DLP bioprinting of cell-dense wound-healing constructs

(A) Schematics (left) and fluorescence micrographs (right) of bioprinted constructs: control, no treatment; GM-MSC, scaffolds of GelMA containing MSCs ($\sim 8 \times 10^6$ cells mL^{-1}); MSC, constructs of biomaterial-minimalistic DLP-bioprinted MSC CLINK; MSC/EC, constructs of biomaterial-minimalistic DLP-bioprinted MSC/EC CLINKs; MSC/EC-RAS, constructs of biomaterial-minimalistic DLP-bioprinted MSC/EC CLINKs in RAS.

(B) Workflow of animal experiments. Mouse dorsal skin-excisional wound model was prepared and treated on day 0, histological analyses and immunostaining were performed on days 7, 14, and 21, and bulk RNA-seq was performed on day 7.

(C) Representative photographs of wounds on days 0, 3, 7, 14, and 21. Right column, wound area tracing analyses corresponding to the photographs.

(D) Quantification analyses of relative wound areas on days 3, 7, and 14.

(E) Representative bright-field micrographs showing H&E staining of wounds on days 7, 14, and 21.

(F) Quantification analyses of re-epithelization ratios on days 7, 14, and 21.

(legend continued on next page)

the CLINK method improved neovascularization in the wound area by day 7, compared with GelMA (Figures 6G and S9B). The strongest CD31 expression occurred in MSC/EC-RAS. After 14 days, the CD31 integral optical density (IOD) in MSC/EC-RAS was 4.28 times higher than in GelMA and 1.48 times higher than in MSC/EC alone.

We next investigated whether CLINK bioprinting influenced hair follicle regeneration. Histological staining confirmed that MSC/EC-RAS had more regenerated hair follicles than any other group by day 21 (Figure 6H). Keratin-15 (K15), expressed in bulge keratinocytes, was also assessed on day 21; the MSC/EC-RAS group displayed complete hair morphogenesis (Figure 6I), whereas other groups had sparse, smaller follicles. Masson's trichrome staining further illustrated collagen deposition in MSC/EC-RAS at day 7 (Figures S10A and S10B), reaching 74.75% ± 6.82% by day 21.

To gain insights into the mechanisms, we performed bulk RNA-seq on day-7 CLINK constructs. Heatmaps and volcano plots of differentially expressed genes (DEGs) revealed a distinct gene expression profile for MSC/EC-RAS compared with MSC or MSC/EC alone (Figures 6J, S10C, and S10D). Gene Ontology (GO) analyses showed that MSC/EC-RAS upregulated genes linked to skin development and cytoskeletal protein binding relative to the MSC or MSC/EC group (Figure S10E). Inflammation-related genes, however, were downregulated in the MSC/EC-RAS group. Together, these findings underscore the potential of biomaterial-minimalistic bioprinting to produce living therapeutics with advanced biofunctionality, driven primarily by enhanced cell-cell interactions, extracellular matrix remodeling, and inflammatory modulation.

DISCUSSION

The CLINK and biomaterial-minimalistic, scaffold-free DLP bioprinting strategy has been established to produce physiological tissue structures containing cell densities similar to those *in vivo*. We have demonstrated that this approach enables rapid bioprinting of more sophisticated planar and volumetric architectures comprising single or multiple cell types at high resolutions and in reasonably high throughput. Achieving such high cell densities, akin to those in native tissues, has historically been a major challenge for the DLP method, which typically relies on photocrosslinkable biomaterials as the principal bioink constituents, resulting in diluted cell suspensions. In a recent study, tuning the refractive index of the biomaterial-based bioink minimized cell-induced scattering, allowing DLP bioprinting with high-density cells.[50] However, that strategy still required substantial amounts of biomaterials as the photocrosslinkable matrix, in addition to the need for a refractive index-matching agent iodixanol, which may exert negative effects on biological tissues.[51]

A key advantage in our approach is the use of OMHA as a linker to modify cell surfaces and produce CLINKs (Video S2), enabling direct photocrosslinking between the adjacent cell membranes without requiring any additional biomolecules. While the amine-aldehyde coupling reaction may reduce pH and generate mild ROS, it did not adversely affect cellular behavior, as evidenced by preserved cellular viability after modification and the ability of ESCs to form EBs and differentiate into specific lineages. These methacrylate bonds in OMHA facilitated rapid patterning with cell densities of up to $\sim 1 \times 10^9$ cells mL^{-1}, i.e., almost pure cells, whereas the control (GelMA or HAMA) consistently failed to maintain structural integrity or cell viability at densities exceeding 1×10^7–10^8 cells mL^{-1}.

To reinforce initial structural integrity in CLINK-bioprinted constructs, a 0.25 w/v% alginate coating was applied immediately after bioprinting in certain complex patterns. A similar stabilization tactic was used in another study.[20] During extended culture, cell-cell contacts gradually strengthened, ultimately preserving the bioprinted structures in the absence of alginate. Once stable intercellular connections formed, alginate was fully removed with EDTA after 1 day. Overall, our strategy has uniquely enabled the patterning capabilities in cell-dense tissues previously unattainable at such high cell densities and intricate architectures without compromising their biomaterial-minimalistic nature, since alginate is only transiently used to stabilize tissue integrity in the very beginning phase.

Bioprinting frequently relies on biomaterial-based bioinks, whereas CLINKs, in this study, redefine the paradigm by relying on living cells themselves as structural building blocks. The resulting bioprinted structures achieve ultrahigh cell densities that foster superior cellular communications and integration. Unlike biomaterial-rich bioinks that can inhibit cell-cell interactions, our scaffold-free constructs promote rapid yet reproducible functional assemblies. For example, functional neural circuits were formed in merely 7 days, validated by optogenetic stimulation and electrical measurements, while cortico-motor assembloids generated through fusion typically need approximately 30 days to achieve similar connectivity.[52] Similarly, our CardioChambers initiated synchronous contractions within 2 days of cultivation, intensifying significantly by day 7, while traditional cardiac organoids often require 20 days for comparable maturation.[53]

Thus, by pioneering this biomaterial-minimalistic, scaffold-free DLP bioprinting strategy, we now allow direct bioprinting of stem cell-derived neurons and hCMs with complex architectures. Of note, this study shows functional neural circuits bioprinted from cortical and motor neurons, opening horizons in neuroengineering. Neurons are highly specialized cells that

(G) Quantification analyses of CD31 IOD values on days 7 and 14.
(H) Quantification analyses of hair follicle numbers on day 21.
(I) Representative immunofluorescence micrographs showing staining of K15 (green) on day 21.
(J) Heatmaps for selected DEGs of MSC/EC-RAS and MSC/EC groups, compared with the MSC groups, showing upregulated (blue) and downregulated (red) genes.
Data are means ± SDs. In (D), (F), and (G), $n = 3$; two-way ANOVA; $^*p < 0.05$, $^{**}p < 0.01$, $^{***}p < 0.001$ (compared with the GM-MSC groups); $\#p < 0.05$, $\#\#p < 0.01$, $\#\#\#p < 0.001$ (compared with the MSC groups); $\hat{}\hat{}p < 0.01$ (compared with the MSC/EC groups). In (H), $n = 6$; one-way ANOVA; $^{**}p < 0.01$, $^{***}p < 0.001$ (compared with the GM-MSC groups); $\#p < 0.05$ (compared with the MSC groups).
See also Figures S9 and S10.

Please cite this article in press as: Wang et al., Biomaterial-minimalistic photoactivated bioprinting of cell-dense tissues, Cell (2026), https://doi.org/10.1016/j.cell.2025.11.012

require precise environmental cues for proper maturation and synapse formation.[54] Previous studies, including our own, have emphasized bioprinting of iPSCs or neural progenitor cells in biomaterial-dense hydrogel matrices and then guiding their differentiation into neuronal tissues.[20,22,55,56] Nonetheless, as demonstrated in this study, cortical neurons did not sufficiently survive in GelMA-rich constructs. Our approach circumvents prolonged differentiation within bioprinted hydrogels by directly bioprinting ESC-derived neuronal CLINKs, thus expediting the development of functional neural circuits while avoiding the constraints imposed by biomaterials on synapse formation.

Another key advance of this technology is the establishment of the CardioChambers, which leverages our scaffold-free bioprinting strategy to generate cardiac tissues with defined hollow architectures and consistent functionality. In contrast to organoid models that often suffer from batch-to-batch variability due to time-consuming heterogeneous differentiation and self-organization,[57,58] CLINK-bioprinted CardioChambers exhibit rapid yet reproducible morphologies, synchronous contractions, and maturation, potentially providing a standardized and reliable platform for future disease modeling and drug testing. Importantly, our current work represents only a proof-of-concept demonstration. This platform can be further expanded by incorporating diverse cardiac cell subtypes (e.g., atrial, ventricular, vascular, and fibroblastic cells), more complex spatial architectures, and even vascular networks, thereby broadening its utility for studying cardiac development, pathology, and regeneration.

Scaffold-free bioprinting has garnered substantial interest for its capability to form dense cellular constructs that secrete their own extracellular matrices, creating functional microenvironments relevant to natural tissues.[59] Many established scaffold-free bioprinting techniques, such as the Kenzan method,[60] aspiration-assisted bioprinting,[10,12] and magnetic bioprinting,[61] use a "pick-and-place" process. Generally, these methods, while potent, can sometimes face challenges in accurately positioning cells at the microscale within complex 3D patterns. In contrast, our biomaterial-minimalistic DLP strategy provides a powerful alternative solution for producing densely cellular 2D and 3D tissues, including challenging features like channels and chambers that require exact geometric fidelity. Crucially, it scales from sub-millimeter to centimeter constructs without sacrificing structural integrity, making it highly versatile for diverse application scenarios. For instance, our liver-mimetic constructs embedded with channels exhibited rapid host integration and endothelialization upon implantation, key for long-term survival. Similarly, vessel-structured MSC/EC implants facilitated wound healing by enhancing cell adhesion, migration, and communications. Moreover, by minimizing or eliminating external biomaterials, our technology can possibly reduce immunogenic risks tied to scaffold implants, thus supporting more natural tissue functionality.

In conclusion, this work represents a pivotal advance by turning living cells into bioinks with minimal exogenic biomaterials. By uniting ultrahigh cell densities with precise spatial organizations, we enable the fabrication of high-content tissues composed entirely of somatic or stem cell-derived cells. This capability not only yields biomimetic tissue architectures but also lays the foundation for unconventional approaches to tissue repair. Furthermore, our bioprinting platform provides a robust tool for creating next-generation functional biological microtissue models, surpassing proof-of-concept studies and offering genuine opportunities for wide-ranging biomedical applications.

Limitations of the study

During longer-term culture (>7 days), the structural stability of biomaterial-minimalistic CLINK-bioprinted tissues at very high cell densities varied according to cell type. Highly proliferative, weakly contact-inhibited cell lines (e.g., MDA-MB-231, HepG2/C3A) sometimes showed uncontrolled growth and self-organization, disrupting initial architectures. In contrast, fully differentiated neural cells and cardiomyocytes preserved bioprinted tissue integrity more effectively. Tailoring CLINK design and refining bioprinting parameters based on cell-specific properties and tissue geometries are essential for improving stability. Controlling precise initial cell densities helps strike a balance between cell-cell interactions and structural integrity. Additional strategies, including using proliferation-inhibitory reagents, might curb excessive growth without hampering functions. Future efforts should also explore additional linker molecule designs to enhance bioprinting performances across a broad range of cell types over extended culture periods.

Our DLP-based biomaterial-minimalistic bioprinting permits the fabrication of complex 3D structures at high resolutions. Nonetheless, multi-material DLP can be hindered by potential bioink contamination. Our bioink-switching technique[23] successfully combined multiple materials at a macroscopic scale, enabling the fabrication of voxelated 3D cubes with distinct cell populations. However, minor contamination persisted in neural circuits, especially under high cell densities that complicate effective washing. Recent advances in multi-material DLP hardware, such as centrifugal-assisted bioink removal,[62] indicate promise in reducing contamination. Future developments could, in addition, focus on hardware optimizations and automation to improve bioprinting quality, speed, and reproducibility further.

RESOURCE AVAILABILITY

Lead contact

Requests for material can be directed to the lead contact, Yu Shrike Zhang (yszhang@bwh.harvard.edu).

Materials availability

This study did not generate new unique reagents. Requests for research materials will be promptly reviewed by the Brigham and Women's Hospital and will be released via a material transfer agreement.

Data and code availability

- RNA-seq data have been deposited to ArrayExpress (#E-MTAB-16055) and are publicly available as of the date of publication.
- This paper does not report original codes.
- Any additional information required to reanalyze the data reported in this paper is available from the lead contact upon request.

ACKNOWLEDGMENTS

This work was supported by funding from the National Institutes of Health (R00CA201603, R01EB028143, R01CA282451, R21EB025270, R21EB030257, and R21HL168656), the National Science Foundation (CBET-EBMS-123859 and CISE-IIS-2225698), the Chan Zuckerberg Initiative (2022-316709 and

2024-347836), the Brigham Research Institute, the National Research Foundation of Korea (NRF) grant (RS-2024-00403376) funded by the Korean Government (MSIT), the Richard and Lauralee Uihlein Mayo Clinic Investigator Award, the Mayo Clinic Professor Endowed Chair, and the Monica Flynn Jacoby Endowed Chair. We would like to further thank the Neuro-Technology Studio at Brigham and Women's Hospital for providing confocal microscopy access and consultation on data acquisition and analyses. Finally, we thank Dr. Cuiyan Xin and Dr. Joseph V. Bonventre for their assistance with certain animal studies. The schematics of Figures 1, 2B, 5B, 5G, 5M, and 6A were created with BioRender.

AUTHOR CONTRIBUTIONS

Conceptualization and method design, M.W., W.L., and Y.S.Z.; investigation and formal analysis, M.W., W.L., J.H., L.C., X. Mei, R.S.F., P.C.C., C.E.G.-M., X. Mu, X.K., J.K.S., X.Y., G.T., Z. Luo, and G.W.; supervision, Y.S.Z.; discussion, Z. Liu, A.Q.-H., K.E., and S.G.; funding acquisition, A.Q.-H., K.E., and Y.S.Z; writing – original draft, M.W., W.L., and Y.S.Z.; writing – reviewing and editing, all authors.

DECLARATION OF INTERESTS

Y.S.Z. consulted for Allevi by 3D Systems; co-founded, consults for, and holds options of Linton Lifesciences; and sits on the scientific advisory board and holds options of Xellar Biosystems. The relevant interests are managed by the Brigham and Women's Hospital.

STAR★METHODS

Detailed methods are provided in the online version of this paper and include the following:

- KEY RESOURCES TABLE
- EXPERIMENTAL MODEL AND STUDY PARTICIPANT DETAILS
  - Cell cultures, human ESC culture and differentiation, and neuronal differentiation
- METHOD DETAILS
  - Linker synthesis and characterizations
  - Hydrazide titration for determining the degree of oxidation of OMHA linker
  - GPC analyses of HA, HAMA, and OMHA
  - Preparation of CLINKs
  - Assessments of ROS levels after cell-linker coupling
  - Comparison of OMHA with commercial acrylate linker
  - Characterizations of ESCs
  - EB-formation
  - hCO induction and neuronal differentiation, and hSpO induction
  - Rheological characterizations of CLINK
  - DLP bioprinter
  - Evaluations of printability
  - Biomaterial-minimalistic DLP bioprinting
  - Fabrication of liver tissues with biomaterial-minimalistic DLP bioprinting
  - Modeling of neural circuits *via* biomaterial-minimalistic DLP bioprinting of human ESC-derived neurons
  - CardioChamber modeling *via* biomaterial-minimalistic DLP bioprinting of human iPSC-derived hCMs
  - Skin-excisional wound model and implantation of bioprinted constructs
- QUANTIFICATION AND STATISTICAL ANALYSIS

SUPPLEMENTAL INFORMATION

Supplemental information can be found online at https://doi.org/10.1016/j.cell.2025.11.012.

Received: October 1, 2022
Revised: September 2, 2025
Accepted: November 6, 2025

REFERENCES

1. Murphy, S.V., and Atala, A. (2014). 3D bioprinting of tissues and organs. Nat. Biotechnol. *32*, 773–785. https://doi.org/10.1038/nbt.2958.
2. Zhang, Y.S., Haghiashtiani, G., Hübscher, T., Kelly, D.J., Lee, J.M., Lutolf, M., McAlpine, M.C., Yeong, W.Y., Zenobi-Wong, M., and Malda, J. (2021). 3D extrusion bioprinting. Nat. Rev. Methods Primers *1*, 75. https://doi.org/10.1038/s43586-021-00073-8.
3. Levato, R., Dudaryeva, O., Garciamendez-Mijares, C.E., Kirkpatrick, B.E., Rizzo, R., Schimelman, J., Anseth, K.S., Chen, S., Zenobi-Wong, M., and Zhang, Y.S. (2023). Light-based vat-polymerization bioprinting. Nat. Rev. Methods Primers *3*, 47. https://doi.org/10.1038/s43586-023-00231-0.
4. Bernal, P.N., Florczak, S., Inacker, S., Kuang, X., Madrid-Wolff, J., Regehly, M., Hecht, S., Zhang, Y.S., Moser, C., and Levato, R. (2025). The road ahead in materials and technologies for volumetric 3D printing. Nat. Rev. Mater. *10*, 826–841. https://doi.org/10.1038/s41578-025-00785-3.
5. Gungor-Ozkerim, P.S., Inci, I., Zhang, Y.S., Khademhosseini, A., and Dokmeci, M.R. (2018). Bioinks for 3D bioprinting: an overview. Biomater. Sci. *6*, 915–946. https://doi.org/10.1039/C7BM00765E.
6. Schwab, A., Levato, R., D'Este, M., Piluso, S., Eglin, D., and Malda, J. (2020). Printability and Shape Fidelity of Bioinks in 3D Bioprinting. Chem. Rev. *120*, 11028–11055. https://doi.org/10.1021/acs.chemrev.0c00084.
7. Ozbolat, I.T. (2015). Scaffold-based or scaffold-free bioprinting: competing or complementing approaches? J. Nanotechnol. Eng. Med. *6*, 024701. https://doi.org/10.1115/1.4030414.
8. Khoshnood, N., and Zamanian, A. (2020). A comprehensive review on scaffold-free bioinks for bioprinting. Bioprinting *19*, e00088. https://doi.org/10.1016/j.bprint.2020.e00088.
9. Norotte, C., Marga, F.S., Niklason, L.E., and Forgacs, G. (2009). Scaffold-free vascular tissue engineering using bioprinting. Biomaterials *30*, 5910–5917. https://doi.org/10.1016/j.biomaterials.2009.06.034.
10. Ayan, B., Heo, D.N., Zhang, Z., Dey, M., Povilianskas, A., Drapaca, C., and Ozbolat, I.T. (2020). Aspiration-assisted bioprinting for precise positioning of biologics. Sci. Adv. *6*, eaaw5111. https://doi.org/10.1126/sciadv.aaw5111.
11. Moldovan, N.I., Hibino, N., and Nakayama, K. (2017). Principles of the Kenzan Method for Robotic Cell Spheroid-Based Three-Dimensional Bioprinting<sup/>. Tissue Eng. Part B Rev. *23*, 237–244. https://doi.org/10.1089/ten.teb.2016.0322.
12. Daly, A.C., Davidson, M.D., and Burdick, J.A. (2021). 3D bioprinting of high cell-density heterogeneous tissue models through spheroid fusion within self-healing hydrogels. Nat. Commun. *12*, 753. https://doi.org/10.1038/s41467-021-21029-2.
13. Skylar-Scott, M.A., Uzel, S.G.M., Nam, L.L., Ahrens, J.H., Truby, R.L., Damaraju, S., and Lewis, J.A. (2019). Biomanufacturing of organ-specific tissues with high cellular density and embedded vascular channels. Sci. Adv. *5*, eaaw2459. https://doi.org/10.1126/sciadv.aaw2459.
14. Loeffler, M., and Roeder, I. (2002). Tissue stem cells: definition, plasticity, heterogeneity, self-organization and models–a conceptual approach. Cells Tissues Organs *171*, 8–26. https://doi.org/10.1159/000057688.
15. Takebe, T., and Wells, J.M. (2019). Organoids by design. Science *364*, 956–959. https://doi.org/10.1126/science.aaw7567.
16. Schutgens, F., and Clevers, H. (2020). Human Organoids: Tools for Understanding Biology and Treating Diseases. Annu. Rev. Pathol. *15*, 211–234. https://doi.org/10.1146/annurev-pathmechdis-012419-032611.
17. Rossi, G., Manfrin, A., and Lutolf, M.P. (2018). Progress and potential in organoid research. Nat. Rev. Genet. *19*, 671–687. https://doi.org/10.1038/s41576-018-0051-9.
18. Brassard, J.A., Nikolaev, M., Hübscher, T., Hofer, M., and Lutolf, M.P. (2021). Recapitulating macro-scale tissue self-organization through organoid bioprinting. Nat. Mater. *20*, 22–29. https://doi.org/10.1038/s41563-020-00803-5.

19. Lawlor, K.T., Vanslambrouck, J.M., Higgins, J.W., Chambon, A., Bishard, K., Arndt, D., Er, P.X., Wilson, S.B., Howden, S.E., Tan, K.S., et al. (2021). Cellular extrusion bioprinting improves kidney organoid reproducibility and conformation. Nat. Mater. *20*, 260–271. https://doi.org/10.1038/s41563-020-00853-9.

20. Skylar-Scott, M.A., Huang, J.Y., Lu, A., Ng, A.H.M., Duenki, T., Liu, S., Nam, L.L., Damaraju, S., Church, G.M., and Lewis, J.A. (2022). Orthogonally induced differentiation of stem cells for the programmatic patterning of vascularized organoids and bioprinted tissues. Nat. Biomed. Eng. *6*, 449–462. https://doi.org/10.1038/s41551-022-00856-8.

21. Jeon, O., Lee, Y.B., Jeong, H., Lee, S.J., Wells, D., and Alsberg, E. (2019). Individual cell-only bioink and photocurable supporting medium for 3D printing and generation of engineered tissues with complex geometries. Mater. Horiz. *6*, 1625–1631. https://doi.org/10.1039/C9MH00375D.

22. Wang, M., Li, W., Hao, J., Gonzales, A., 3rd, Zhao, Z., Flores, R.S., Kuang, X., Mu, X., Ching, T., Tang, G., et al. (2022). Molecularly cleavable bioinks facilitate high-performance digital light processing-based bioprinting of functional volumetric soft tissues. Nat. Commun. *13*, 3317. https://doi.org/10.1038/s41467-022-31002-2.

23. Wang, M., Li, W., Mille, L.S., Ching, T., Luo, Z., Tang, G., Garciamendez, C.E., Lesha, A., Hashimoto, M., and Zhang, Y.S. (2022). Digital Light Processing Based Bioprinting with Composable Gradients. Adv. Mater. *34*, e2107038. https://doi.org/10.1002/adma.202107038.

24. Li, W., Wang, M., Mille, L.S., Robledo Lara, J.A., Huerta, V., Uribe Velázquez, T., Cheng, F., Li, H., Gong, J., Ching, T., et al. (2021). A Smartphone-Enabled Portable Digital Light Processing 3D Printer. Adv. Mater. *33*, e2102153. https://doi.org/10.1002/adma.202102153.

25. Li, W., Mille, L.S., Robledo, J.A., Uribe, T., Huerta, V., and Zhang, Y.S. (2020). Recent Advances in Formulating and Processing Biomaterial Inks for Vat Polymerization-Based 3D Printing. Adv. Healthc. Mater. *9*, e2000156. https://doi.org/10.1002/adhm.202000156.

26. Koffler, J., Zhu, W., Qu, X., Platoshyn, O., Dulin, J.N., Brock, J., Graham, L., Lu, P., Sakamoto, J., Marsala, M., et al. (2019). Biomimetic 3D-printed scaffolds for spinal cord injury repair. Nat. Med. *25*, 263–269. https://doi.org/10.1038/s41591-018-0296-z.

27. Grigoryan, B., Paulsen, S.J., Corbett, D.C., Sazer, D.W., Fortin, C.L., Zaita, A.J., Greenfield, P.T., Calafat, N.J., Gounley, J.P., Ta, A.H., et al. (2019). Multivascular networks and functional intravascular topologies within biocompatible hydrogels. Science *364*, 458–464. https://doi.org/10.1126/science.aav9750.

28. Huang, G., Ye, S., Zhou, X., Liu, D., and Ying, Q.L. (2015). Molecular basis of embryonic stem cell self-renewal: from signaling pathways to pluripotency network. Cell. Mol. Life Sci. *72*, 1741–1757. https://doi.org/10.1007/s00018-015-1833-2.

29. Fok, E.Y.L., and Zandstra, P.W. (2005). Shear-controlled single-step mouse embryonic stem cell expansion and embryoid body-based differentiation. Stem Cells *23*, 1333–1342. https://doi.org/10.1634/stemcells.2005-0112.

30. Fergus, J., Quintanilla, R., and Lakshmipathy, U. (2014). Characterizing Pluripotent Stem Cells Using the TaqMan® hPSC Scorecard(TM) Panel. In Human Embryonic Stem Cell Protocols (Springer), pp. 25–37. https://doi.org/10.1007/7651_2014_109.

31. Miura, Y., Li, M.Y., Revah, O., Yoon, S.J., Narazaki, G., and Pașca, S.P. (2022). Engineering brain assembloids to interrogate human neural circuits. Nat. Protoc. *17*, 15–35. https://doi.org/10.1038/s41596-021-00632-z.

32. Elson, E.L. (1988). Cellular mechanics as an indicator of cytoskeletal structure and function. Annu. Rev. Biophys. Biophys. Chem. *17*, 397–430. https://doi.org/10.1146/annurev.bb.17.060188.002145.

33. Huang, D., Liu, T., Liao, J., Maharjan, S., Xie, X., Pérez, M., Anaya, I., Wang, S., Tirado Mayer, A., Kang, Z., et al. (2021). Reversed-engineered human alveolar lung-on-a-chip model. Proc. Natl. Acad. Sci. USA *118*, e2016146118. https://doi.org/10.1073/pnas.2016146118.

34. Miri, A.K., Nieto, D., Iglesias, L., Goodarzi Hosseinabadi, H., Maharjan, S., Ruiz-Esparza, G.U., Khoshakhlagh, P., Manbachi, A., Dokmeci, M.R., Chen, S., et al. (2018). Microfluidics-Enabled Multimaterial Maskless Stereolithographic Bioprinting. Adv. Mater. *30*, e1800242. https://doi.org/10.1002/adma.201800242.

35. Ma, X., Yu, C., Wang, P., Xu, W., Wan, X., Lai, C.S.E., Liu, J., Koroleva-Maharajh, A., and Chen, S. (2018). Rapid 3D bioprinting of decellularized extracellular matrix with regionally varied mechanical properties and biomimetic microarchitecture. Biomaterials *185*, 310–321. https://doi.org/10.1016/j.biomaterials.2018.09.026.

36. Maharjan, S., Alva, J., Cámara, C., Rubio, A.G., Hernández, D., Delavaux, C., Correa, E., Romo, M.D., Bonilla, D., Santiago, M.L., et al. (2021). Symbiotic photosynthetic oxygenation within 3D-bioprinted vascularized tissues. Matter *4*, 217–240. https://doi.org/10.1016/j.matt.2020.10.022.

37. Bhatia, S.N., and Ingber, D.E. (2014). Microfluidic organs-on-chips. Nat. Biotechnol. *32*, 760–772. https://doi.org/10.1038/nbt.2989.

38. Low, L.A., Mummery, C., Berridge, B.R., Austin, C.P., and Tagle, D.A. (2021). Organs-on-chips: into the next decade. Nat. Rev. Drug Discov. *20*, 345–361. https://doi.org/10.1038/s41573-020-0079-3.

39. Daly, A.C., Prendergast, M.E., Hughes, A.J., and Burdick, J.A. (2021). Bioprinting for the Biologist. Cell *184*, 18–32. https://doi.org/10.1016/j.cell.2020.12.002.

40. Madrid-Wolff, J., Boniface, A., Loterie, D., Delrot, P., and Moser, C. (2022). Controlling Light in Scattering Materials for Volumetric Additive Manufacturing. Adv. Sci. (Weinh) *9*, e2105144. https://doi.org/10.1002/advs.202105144.

41. Guan, J., You, S., Xiang, Y., Schimelman, J., Alido, J., Ma, X., Tang, M., and Chen, S. (2021). Compensating the cell-induced light scattering effect in light-based bioprinting using deep learning. Biofabrication *14*, 015011. https://doi.org/10.1088/1758-5090/ac3b92.

42. Rizzo, R., Petelinšek, N., Bonato, A., and Zenobi-Wong, M. (2023). From Free-Radical to Radical-Free: A Paradigm Shift in Light-Mediated Biofabrication. Adv. Sci. (Weinh) *10*, e2205302. https://doi.org/10.1002/advs.202205302.

43. Ma, X., Qu, X., Zhu, W., Li, Y.-S., Yuan, S., Zhang, H., Liu, J., Wang, P., Lai, C.S.E., Zanella, F., et al. (2016). Deterministically patterned biomimetic human iPSC-derived hepatic model via rapid 3D bioprinting. Proc. Natl. Acad. Sci. USA *113*, 2206–2211. https://doi.org/10.1073/pnas.1524510113.

44. Hasan, M.F., and Berdichevsky, Y. (2016). Neural Circuits on a Chip. Micromachines (Basel) *7*, 157. https://doi.org/10.3390/mi7090157.

45. Kamudzandu, M., Köse-Dunn, M., Evans, M.G., Fricker, R.A., and Roach, P. (2019). A micro-fabricated in vitro complex neuronal circuit platform. Biomed. Phys. Eng. Express *5*, 045016. https://doi.org/10.1088/2057-1976/ab2307.

46. Limone, F., Guerra San Juan, I., Mitchell, J.M., Smith, J.L.M., Raghunathan, K., Meyer, D., Ghosh, S.D., Couto, A., Klim, J.R., Joseph, B.J., et al. (2023). Efficient generation of lower induced motor neurons by coupling Ngn2 expression with developmental cues. Cell Rep. *42*, 111896. https://doi.org/10.1016/j.celrep.2022.111896.

47. Nehme, R., Zuccaro, E., Ghosh, S.D., Li, C., Sherwood, J.L., Pietilainen, O., Barrett, L.E., Limone, F., Worringer, K.A., Kommineni, S., et al. (2018). Combining NGN2 Programming with Developmental Patterning Generates Human Excitatory Neurons with NMDAR-Mediated Synaptic Transmission. Cell Rep. *23*, 2509–2523. https://doi.org/10.1016/j.celrep.2018.04.066.

48. Kivimäki, M., and Steptoe, A. (2018). Effects of stress on the development and progression of cardiovascular disease. Nat. Rev. Cardiol. *15*, 215–229. https://doi.org/10.1038/nrcardio.2017.189.

49. Chen, S., Wang, H., Su, Y., John, J.V., McCarthy, A., Wong, S.L., and Xie, J. (2020). Mesenchymal stem cell-laden, personalized 3D scaffolds with controlled structure and fiber alignment promote diabetic wound healing. Acta Biomater. *108*, 153–167. https://doi.org/10.1016/j.actbio.2020.03.035.

50. You, S., Xiang, Y., Hwang, H.H., Berry, D.B., Kiratitanaporn, W., Guan, J., Yao, E., Tang, M., Zhong, Z., Ma, X., et al. (2023). High cell density and high-resolution 3D bioprinting for fabricating vascularized tissues. Sci. Adv. *9*, eade7923. https://doi.org/10.1126/sciadv.ade7923.

51. Jo, S.-H., Youn, T.-J., Koo, B.-K., Park, J.-S., Kang, H.-J., Cho, Y.-S., Chung, W.-Y., Joo, G.-W., Chae, I.-H., Choi, D.-J., et al. (2006). Renal toxicity evaluation and comparison between visipaque (iodixanol) and hexabrix (ioxaglate) in patients with renal insufficiency undergoing coronary angiography: the RECOVER study: a randomized controlled trial. J. Am. Coll. Cardiol. *48*, 924–930. https://doi.org/10.1016/j.jacc.2006.06.047.

52. Andersen, J., Revah, O., Miura, Y., Thom, N., Amin, N.D., Kelley, K.W., Singh, M., Chen, X., Thete, M.V., Walczak, E.M., et al. (2020). Generation of Functional Human 3D Cortico-Motor Assembloids. Cell *183*, 1913–1929.e26. https://doi.org/10.1016/j.cell.2020.11.017.

53. Hofbauer, P., Jahnel, S.M., Papai, N., Giesshammer, M., Deyett, A., Schmidt, C., Penc, M., Tavernini, K., Grdseloff, N., Meledeth, C., et al. (2021). Cardioids reveal self-organizing principles of human cardiogenesis. Cell *184*, 3299–3317.e22. https://doi.org/10.1016/j.cell.2021.04.034.

54. Colón-Ramos, D.A. (2009). Synapse formation in developing neural circuits. Curr. Top. Dev. Biol. *87*, 53–79. https://doi.org/10.1016/S0070-2153(09)01202-2.

55. Yan, Y., Li, X., Gao, Y., Mathivanan, S., Kong, L., Tao, Y., Dong, Y., Li, X., Bhattacharyya, A., Zhao, X., et al. (2024). 3D bioprinting of human neural tissues with functional connectivity. Cell Stem Cell *31*, 260–274.e7. https://doi.org/10.1016/j.stem.2023.12.009.

56. Kupfer, M.E., Lin, W.H., Ravikumar, V., Qiu, K., Wang, L., Gao, L., Bhuiyan, D.B., Lenz, M., Ai, J., Mahutga, R.R., et al. (2020). In Situ Expansion, Differentiation, and Electromechanical Coupling of Human Cardiac Muscle in a 3D Bioprinted, Chambered Organoid. Circ. Res. *127*, 207–224. https://doi.org/10.1161/CIRCRESAHA.119.316155.

57. Zhao, Z., Chen, X., Dowbaj, A.M., Sljukic, A., Bratlie, K., Lin, L., Fong, E.L.S., Balachander, G.M., Chen, Z., Soragni, A., et al. (2022). Organoids. Natl. Rev. Methods Prim. *2*, 94. https://doi.org/10.1038/s43586-022-00174-y.

58. Silva, A.C., Matthys, O.B., Joy, D.A., Kauss, M.A., Natarajan, V., Lai, M.H., Turaga, D., Blair, A.P., Alexanian, M., Bruneau, B.G., et al. (2021). Co-emergence of cardiac and gut tissues promotes cardiomyocyte maturation within human iPSC-derived organoids. Cell Stem Cell *28*, 2137–2152.e6. https://doi.org/10.1016/j.stem.2021.11.007.

59. Ovsianikov, A., Khademhosseini, A., and Mironov, V. (2018). The Synergy of Scaffold-Based and Scaffold-Free Tissue Engineering Strategies. Trends Biotechnol. *36*, 348–357. https://doi.org/10.1016/j.tibtech.2018.01.005.

60. Itoh, M., Nakayama, K., Noguchi, R., Kamohara, K., Furukawa, K., Uchihashi, K., Toda, S., Oyama, J.-I., Node, K., and Morita, S. (2015). Scaffold-free tubular tissues created by a bio-3D printer undergo remodeling and endothelialization when implanted in rat aortae. PLoS One *10*, e0136681. https://doi.org/10.1371/journal.pone.0136681.

61. Roth, J.G., Brunel, L.G., Huang, M.S., Liu, Y., Cai, B., Sinha, S., Yang, F., Paşca, S.P., Shin, S., and Heilshorn, S.C. (2023). Spatially controlled construction of assembloids using bioprinting. Nat. Commun. *14*, 4346. https://doi.org/10.1038/s41467-023-40006-5.

62. Cheng, J., Wang, R., Sun, Z., Liu, Q., He, X., Li, H., Ye, H., Yang, X., Wei, X., Li, Z., et al. (2022). Centrifugal multimaterial 3D printing of multifunctional heterogeneous objects. Nat. Commun. *13*, 7931. https://doi.org/10.1038/s41467-022-35622-6.

63. Zhang, F., Wang, L.P., Brauner, M., Liewald, J.F., Kay, K., Watzke, N., Wood, P.G., Bamberg, E., Nagel, G., Gottschalk, A., et al. (2007). Multimodal fast optical interrogation of neural circuitry. Nature *446*, 633–639. https://doi.org/10.1038/nature05744.

64. Teramura, Y., Kaneda, Y., Totani, T., and Iwata, H. (2008). Behavior of synthetic polymers immobilized on a cell membrane. Biomaterials *29*, 1345–1355. https://doi.org/10.1016/j.biomaterials.2007.11.048.

65. Yoon, S.J., Elahi, L.S., Paşca, A.M., Marton, R.M., Gordon, A., Revah, O., Miura, Y., Walczak, E.M., Holdgate, G.M., Fan, H.C., et al. (2019). Reliability of human cortical organoid generation. Nat. Methods *16*, 75–78. https://doi.org/10.1038/s41592-018-0255-0.

66. Lim, K.S., Levato, R., Costa, P.F., Castilho, M.D., Alcala-Orozco, C.R., van Dorenmalen, K.M.A., Melchels, F.P.W., Gawlitta, D., Hooper, G.J., Malda, J., et al. (2018). Bio-resin for high resolution lithography-based biofabrication of complex cell-laden constructs. Biofabrication *10*, 034101. https://doi.org/10.1088/1758-5090/aac00c.

67. Yang, Y., Chu, C., Liu, L., Wang, C., Hu, C., Rung, S., Man, Y., and Qu, Y. (2023). Tracing immune cells around biomaterials with spatial anchors during large-scale wound regeneration. Nat. Commun. *14*, 5995. https://doi.org/10.1038/s41467-023-41608-9.

68. Bolger, A.M., Lohse, M., and Usadel, B. (2014). Trimmomatic: a flexible trimmer for Illumina sequence data. Bioinformatics *30*, 2114–2120. https://doi.org/10.1093/bioinformatics/btu170.

69. Kim, D., Langmead, B., and Salzberg, S.L. (2015). HISAT: a fast spliced aligner with low memory requirements. Nat. Methods *12*, 357–360. https://doi.org/10.1038/nmeth.3317.

70. Liao, Y., Smyth, G.K., and Shi, W. (2014). featureCounts: an efficient general purpose program for assigning sequence reads to genomic features. Bioinformatics *30*, 923–930. https://doi.org/10.1093/bioinformatics/btt656.

71. Sherman, B.T., Hao, M., Qiu, J., Jiao, X., Baseler, M.W., Lane, H.C., Imamichi, T., and Chang, W. (2022). DAVID: a web server for functional enrichment analysis and functional annotation of gene lists (2021 update). Nucleic Acids Res. *50*, W216–W221. https://doi.org/10.1093/nar/gkac194.

72. Villanueva, R.A.M., and Chen, Z.J. (2019). ggplot2: Elegant Graphics for Data Analysis (2nd ed.). Measurement: Interdisciplinary Research and Perspectives *17*, 160–167. https://doi.org/10.1080/15366367.2019.1565254.

Please cite this article in press as: Wang et al., Biomaterial-minimalistic photoactivated bioprinting of cell-dense tissues, Cell (2026), https://doi.org/10.1016/j.cell.2025.11.012

STAR★METHODS

KEY RESOURCES TABLE

REAGENT or RESOURCE	SOURCE	IDENTIFIER
Antibodies		
Mouse monoclonal anti-SOX-2	R&D Systems	Cat# MAB2018; RRID AB_358009
Goat monoclonal anti-Oct-3/4	R&D Systems	Cat# AF1759; RRID: AB_354975
Rabbit monoclonal anti-Albumin	Abcam	Cat# ab207327; RRID: AB_2755031
F-actin monoclonal Antibody	ThermoFisher	Cat# MA1-80729 RRID: AB_936561
Mouse monoclonal anti-E-cadherin	Abcam	Cat# ab231303; RRID: AB_562059
Mouse monoclonal anti-CYP1A2	Abcam	Cat# ab22717; RRID: AB_447282
Monoclonal anti-CYP3A4	ThermoFisher	Cat# MA3-032; RRID: AB_2261518
Mouse monoclonal anti-TUJ1	R&D Systems	Cat# NL1195V; RRID: AB_1241877
Rabbit monoclonal anti-CamKII	Abcam	Cat# AB134041; RRID AB_2811181
Monoclonal anti-Map-2	Abcam	Cat# ab5392; RRID:AB_2138153
Monoclonal anti-Isl-1	Millipore	Cat# ab20670; RRID:AB_881306
Chemicals, peptides, and recombinant proteins		
Hyaluronic acid	HAworks	HA-250k; CAS:
Dimethylformamide	Sigma-Aldrich	270547; CAS: 68-12-2
Methacrylate anhydride	Sigma-Aldrich	276685; CAS: 760-93-0
Sodium hydroxide	Sigma-Aldrich	221465; CAS: 1310-73-2
Sodium periodate	Sigma-Aldrich	311448; CAS: 7790-28-5
Y-27632	Tocris	Cat# 125450
SB431542	Sigma-Aldrich	Cat# S4317
LDN-193189	Tocris	Cat# 6053
Retinoic acid	Sigma-Aldrich	Cat# R2625
SAG	Santa Cruz Biotechnology	Cat# sc-202814A
Doxycycline	Sigma-Aldrich	Cat# D9891
Puromycin	Life Technologies	Cat# A11138
Human BDNF recombinant protein	Life Technologies	Cat# PHC7084
Human GDNF recombinant protein	ThermoFisher	Cat# PHC7045
Human CNTF recombinant protein	ThermoFisher	Cat# PHC7015
Dorsomorphin	Sigma-Aldrich	Cat# P5499
Human EGF recombinant protein	R&D Systems	Cat# 236-EG
Human FGF2 recombinant protein	R&D Systems	Cat# 233-FB
Human NT-3 recombinant protein	PeproTech	Cat# 450-03
FUDR	Sigma-Aldrich	Cat# F0503
XAV939	Tocris	Cat# 3748
Critical commercial assays		
SuperScript VILO cDNA Synthesis Kit	Invitrogen	11754250
TaqMan hPSC Scorecard	Life Technologies	A15872
CellTiter 96 AQueous Assay	Promega	PAG3580
Albumin ELISA kit	Abcam	AB179887
CellTiter-Glo Luminescent Cell Viability Assay	Promega	G9681
Experimental models: Cell lines		
NIH/3T3	ATCC	CRL-1658
MDA-MB-231	ATCC	HTB-26

(*Continued on next page*)

Please cite this article in press as: Wang et al., Biomaterial-minimalistic photoactivated bioprinting of cell-dense tissues, Cell (2026), https://doi.org/10.1016/j.cell.2025.11.012

Continued

REAGENT or RESOURCE	SOURCE	IDENTIFIER
HepG2/C3A	ATCC	CRL-10741
A549	ATCC	CCL-185
GFP-HUVECs	Angio-Proteomie	cAP-0001GFP
HUVECs	ATCC	PCS-100-013
Human umbilical vein SMCs	ScienCell Research Laboratories	8020
HLMECs	LONZA	CC-2527
Human ESC line WA01 (H1)	WiCell Research Institute	https://grants.nih.gov/stem_cells/registry/current.htm?id=29
Oligonucleotides		
Primers for the neuronal gene-assessments, see Table S1	This paper	N/A
Primers for hepatic tissue evaluations, see Table S2	This paper	N/A
Recombinant DNA		
Plasmid: pLenti-CaMKIIa-hChR2(H134R)-mCherry-WPRE	Zhange et al. [63]	Addgene Plasmid #20943
Software and algorithms		
ZEN black	Zeiss	https://www.zeiss.com
SolidWorks 2019	Dassault Systèmes	https://www.solidworks.com
ImageJ (v 2.0.0-rc-69/1.52p)	NIH	https://imagej.net/ij/
MestreNova (6.2.0)	Mestrelab Research	https://mestrelab.com
Quantstudio Real-time PCR Software (v1.5.1)	ThermoFisher	https://www.thermofisher.com
GraphPad Prism (v8.2.0)	GraphPad Software	https://www.graphpad.com/
Adobe Illustrator CC 2021	Adobe	https://www.adobe.com/
Adobe Photoshop CC 2021	Adobe	https://www.adobe.com/
BioRender	BioRender	https://biorender.com/
Deposited data		
RNA-seq of skin-excisional wound implantation	This paper	ArrayExpress #E-MTAB-16055

EXPERIMENTAL MODEL AND STUDY PARTICIPANT DETAILS

Cell cultures, human ESC culture and differentiation, and neuronal differentiation

NIH/3T3 fibroblasts, MDA-MB-231 cells, and HepG2/C3A cells (American Type Culture Collection, ATCC, USA) were cultured in Dulbecco's modified Eagle medium (DMEM, ThermoFisher, USA) supplemented with 10 v/v% fetal bovine serum (FBS, Gibco, USA) and 1 v/v% antibiotic-antimycotic (Gibco). A549 cells (ATCC) were maintained in F-12K medium (Gibco) supplemented with 10 v/v% FBS and 1 v/v% antibiotic-antimycotic. GFP-HUVECs and pristine HUVECs (ATCC) were maintained in EC-growth medium-2 (EGM-2, Lonza, Switzerland). Human umbilical vein SMCs were obtained from ScienCell Research Laboratories (USA) and cultured in SMC-growth medium-2 (SmGM-2, Lonza). HLMECs (Lonza) were cultured in EGM-2 microvascular EC-growth medium (EGM-2 MV, Lonza). All cells above were incubated at 37 °C and 5% CO_2 and sub-cultured when they reached 80-90% confluency.

Human ESC line WA01 (H1) was obtained from WiCell Research Institute (USA) and was previously approved by the Institutional Review Boards of Harvard University. Our laboratories screen for mycoplasma contamination routinely using the MycoAlert kit (Lonza) with no cell line used in this study testing positive. The use of these cells at Harvard was further approved and determined not to constitute Human Subjects Research by the Committee on the Use of Human Subjects in Research at Harvard University. Human ESCs were cultured with mTeSR plus medium (StemCell Technologies, Canada) on GelTrex (Gibco)-coated tissue culture dishes. Stem cells were maintained in 5% CO_2 incubators at 37 °C. Medium was changed every other day until passaging. After dissociation, 10-μM ROCK-inhibitor (Y-27632, Tocris, UK) was added to cell culture for 24 h, and the cells were co-infected with TetO-Ngn2-Puro and reverse tetracycline-controlled transactivator (rtTA).

Motor neurons were differentiated as previously described.[46] In brief, the cells were passaged and differentiated at the confluency of 70-80%. For the first 4 days of motor neuron differentiation, medium was changed to the induction medium with DMEM-F12

Please cite this article in press as: Wang et al., Biomaterial-minimalistic photoactivated bioprinting of cell-dense tissues, Cell (2026), https://doi.org/10.1016/j.cell.2025.11.012

(Life Technologies, USA), 1× GlutaMAX (Gibco), 1× N-2 supplement (Gibco), 0.1-mM non-essential amino acid (Gibco), and 0.5% glucose (Life Technologies). 10-μM SB431542 (Tocris), 100-nM LDN-193189 (Stemgent, USA), 1-μM retinoic acid (Sigma-Aldrich, USA), and 1-μM SAG (Santa Cruz Biotechnology, USA) were added on days 1-3. For NGN2 induction and neuron selection, 20-mg mL^{-1} doxycycline (Sigma-Aldrich) and 10-mg mL^{-1} puromycin (Life Technologies) were added on days 2-3. On days 4-7, the N2 medium was changed to Neurobasal (Life Technologies) containing 1× N-2 supplement, 1× B-27 supplement (Gibco), 1× GlutaMAX, and 100-μM non-essential amino-acids. Small molecules were added with 1-μM retinoic acid, 1-μM SAG, 20-mg mL^{-1} doxycycline, 10-mg mL^{-1} puromycin, and 10-ng mL^{-1} neurotrophic factors: glial cell-derived neurotrophic factor (GDNF, ThermoFisher), ciliary neurotrophic factor (CNTF, ThermoFisher), and brain-derived neurotrophic factor (BDNF, Life Technologies). On days 5-7, 10-mM 5-fluoro-2'-deoxyuridine thymidylate synthase inhibitor (FUDR, Sigma-Aldrich) was added to kill the mitotic cells. From day 8, the medium was changed to neuronal supportive medium containing Neurobasal, 1× N-2 supplement, 1× B-27 supplement, 1× GlutaMAX, and 100-μM non-essential amino-acids. The medium was supplemented with 10 ng mL^{-1} of neurotrophic factors (GDNF, CNTF, and BDNF). From this time onwards, half-medium change was performed every 2-3 days.

The differentiation of excitatory glutamatergic neurons was conducted as previously described.[47] In brief, stem cells were differentiated in the KnockOut Serum Replacement (KSR) medium (ThermoFisher) supplemented with 10-μM SB431542, 100-nM LDN-193189, 2-μM XAV939 (Tocris), and 2-μg mL^{-1} doxycycline (doxycycline was maintained for the entire differentiation process) for the first day. On day 2, the cells were differentiated using 50% KSR medium and 50% N2 medium supplemented with SB431542/XAV939/LDN-193189 and 5-μg μL^{-1} puromycin. On day 3, the medium was changed to N2 medium with 1× B27 supplement and 10-ng mL^{-1} neurotrophic factors (GDNF, CNTF, and BDNF). On day 4, neurobasal medium supplemented with 1× B27 supplement and 10-ng mL^{-1} neurotrophic factors (GDNF, CNTF, and BDNF) was added and maintained. Half medium-change was performed every 2-3 days.

METHOD DETAILS

Linker synthesis and characterizations

Briefly, 4.0 g of HA with MW of 250 kDa (HAworks, USA) was fully dissolved in 200 mL of deionized (DI) water overnight at 4 °C. 133.3 mL of dimethylformamide (DMF, Sigma-Aldrich) and 7.88 mL of methacrylate anhydride (MA, Sigma-Aldrich) were added to the HA solution under vigorous stirring. The pH of the solution was regulated to 8-9 with 1-M sodium hydroxide (Sigma-Aldrich) solution. The reaction was kept at 4 °C under continuous stirring for another 18 h. Subsequently, 0.5-M NaCl (Sigma-Aldrich) was dissolved in the mixture, and the mixture was precipitated in a double volume of ethanol (Sigma-Aldrich). HAMA was then collected as white pellets after precipitation. The precipitate was washed with ethanol 3 times before being dissolved in DI water and the solution was dialyzed against DI water for 5 days. Then, 1 g of HAMA synthesized from last step was fully dissolved in 200 mL of DI water overnight at 4 °C. 0.29 g of sodium periodate (Sigma-Aldrich) was added to the HAMA solution, and reacted for 2 h at room temperature. The linker was then purified by dialysis against DI water for 5-7 days, and further lyophilized for future study. The product was obtained by lyophilization and characterized by ^{1}H NMR spectroscopy (Bruker Avance II 300-MHz NMR, USA). For fluorescently labeled linker, OMHA was reacted with FITC-PEG-NH_2 (PG2-AMFC-2000, NANOCS, USA) in phosphate-buffered saline (PBS) for 4 h in the dark under stirring at room temperature. After dialyzing the mixture solution against DI water for 5 days and lyophilization, the FITC-labeled linker was obtained. As a control, fluorescently labeled HAMA were synthesized by dissolving HAMA in 2-(*N*-morpholino)ethanesulfonic acid (MES, Sigma-Aldrich) buffer and activated with 1-ethyl-3-(3-dimethylaminopropyl)carbodiimide/N-hydroxysuccinimide (EDC/NHS, Sigma-Aldrich) for 30 min, followed by conjugation with FITC-PEG-NH_2 in the dark for 4 h. The reaction mixture was then dialyzed against DI water for 7 days and lyophilized to obtain the final product.

Hydrazide titration for determining the degree of oxidation of OMHA linker

An excess of 0.25-M hydroxylamine hydrochloride (Sigma-Aldrich) was added to the 2 w/v% linker solution and reacted at 40 °C in the dark for 2 h. The mixture was then titrated with 0.1-M sodium hydroxide under continuous monitoring with a pH meter. The volume of sodium hydroxide required to reach a pH of 4 was recorded. The degree of oxidation was calculated according to the following equation:

$$DO(\%) = \left(\frac{mol_{CHO}}{mol_{disaccharide\ unit}}\right) \times 100\%$$

, where DO represents degree of oxidation, mol_{CHO} represents the amount of aldehyde groups determined from titration, and $mol_{disaccharide\ unit}$ was calculated as:

$$mol_{disaccharide\ unit} = \frac{mass_{HA}}{401.3}$$

, where 401.3 g mol^{-1} corresponds to the MW of one HA disaccharide repeating unit.

GPC analyses of HA, HAMA, and OMHA

Lyophilized HA, HAMA, or OMHA was dissolved in 1-M sodium nitrate (Sigma-Aldrich) at a concentration of 4 mg mL^{-1} and filtered through a 0.2-μm membrane filter. Subsequently, 100 μL of the freshly prepared solution was injected for analysis, with 1-M sodium nitrate serving as the mobile phase at a flow rate of 1 mL min^{-1}. Measurements were carried out on an Agilent 1260 system (Agilent Technologies, USA).

Preparation of CLINKs

For cell-linker coupling, the OMHA linker was first dissolved in sterile PBS (pH 7.4) at 4 °C to a final concentration of 2 w/v%. Cell pellets were obtained by gentle centrifugation (1,000 rpm, 5 min) and resuspended in an equal volume of the linker solution. The cell-linker suspension was incubated at room temperature (25 °C) for 5 min to allow amine-aldehyde coupling between cell membrane and the linker. After incubation, the mixture was gently centrifuged to remove unreacted linker. To prepare CLINK for bioprinting, the resulting CLINK was supplemented with a photoinitiator of Ru/SPS (Advanced BioMatrix, USA), with a volume ratio of CLINK:photoinitiator=100:1, yielding final concentrations of 0.5-mM Ru and 5-mM SPS. All procedures were conducted under sterile conditions. A step-by-step video protocol (Video S2) is provided to facilitate reproducibility. For most bioprinting experiments in this study, CLINKs were additionally supplemented with 1.0 w/v% photoabsorber (Ponceau 4R, Sigma-Aldrich) to improve resolution, unless otherwise specified.

Assessments of ROS levels after cell-linker coupling

For quantitative ROS-assessments following cell-linker coupling, a fluorescent ROS-detection kit (ThermoFisher, purified ROS probe) was used according to the manufacturer's instructions. The working probe solution (10 μM) and positive control solution (100 μM) were prepared in serum-free medium. Detached cells were treated with the OMHA linker or PBS for 1, 5, or 10 min, followed by gentle centrifugation, and resuspension in the probe solution. After incubation at 37 °C for 50 min in the dark, cells were washed 2-3 times with serum-free medium. Fluorescence intensities were measured using a microplate reader (Molecular Devices, USA) with an excitation wavelength of 488 nm and an emission wavelength of 525 nm.

Comparison of OMHA with commercial acrylate linker

For comparison, a commercial acrylate linker, acrylate-poly(ethylene glycol) 7.5K-succinimidyl carboxymethyl ester (NHS-PEG7.5K-acrylate), was used as a control. OMHA proved notably superior to NHS-PEG7.5K-acrylate in terms of printing fidelity and pattern-maintenance, even at much shorter curing times (Figure S1F). This was likely because the reaction time required between NHS and amine groups on cell membranes is much longer than that between aldehyde and amine groups, in addition to the optimal pH needed for amine reactivity (pH 7.2-9) in the former case.[64]

Characterizations of ESCs

ESCs or ESC CLINK were directly seeded into a Matrigel (Corning)-coated well plate. Additionally, ESC CLINK was bioprinted onto Matrigel-coated coverslips using a crosslinking time of 10 s. ESCs, ESCs modified with the OMHA linker, and biomaterial-minimalistic DLP-bioprinted ESCs were all maintained in mTeSR medium for 2 days. To detect the surface biomarkers, ESCs were rinsed with PBS and fixed in 4 w/v% paraformaldehyde (PFA, Sigma-Aldrich) for 10 min at room temperature. After rinsing with PBS, the samples were permeabilized with 0.3% Triton X-100 (Sigma-Aldrich) for 10 min and blocked in 5 w/v% bovine serum albumin (BSA, Sigma-Aldrich) for 1 h. Samples were subsequently incubated overnight at 4 °C with primary antibodies: Sox-2 (R&D Systems, USA) and Oct-3/4 (R&D Systems). Then the samples were incubated with secondary antibodies: Alexa Fluor 594 donkey anti-mouse (ThermoFisher) and Alexa Fluor 488 donkey anti-goat (ThermoFisher) for 2 h at room temperature. 4', 6-Diamidino-2-phenylindole (DAPI, Vector Laboratories, USA) was finally used to counterstain the nuclei. The stained samples were visualized by a confocal microscope (LSM880, Zeiss, Germany) and analyzed with ImageJ (National Institutes of Health, NIH, USA).

EB-formation

For EB-formation, ESCs were either used directly or first modified with the OMHA linker as described above. To obtain uniformly sized EBs, AggreWell-800 (StemCell Technologies) containing 300 microwells was used. Approximately 3×10^6 cells were added per well in Essential 8 medium (ThermoFisher) supplemented with the ROCK inhibitor Y-27632 (10 μM). The AggreWell plate was centrifuged at 100 g for 3 min to capture the cells in the microwells and then incubated at 37 °C with 5% CO_2. After 48 h, the EB spheres were collected from each well by pipetting the medium with a cut P1000 pipette tip and transferred into ultra-low attachment plastic dishes (Corning). EBs were imaged on day 7 with an inverted microscope (Zeiss). To quantitatively confirm the pluripotency of EBs, total RNAs were isolated from day-3 EBs using TRIzol (ThermoFisher). Then, the first-strand cDNA was synthesized using the SuperScript® VILO™ cDNA Synthesis Kit (Invitrogen, USA) according to the instructions of the manufacturer. Next, the qRT-PCR was performed with 384-well TaqMan® hPSC Scorecard™ Panel plates (Life Technologies) that were run on QuantStudio™ 5 Real-Time PCR instrument (ThermoFisher). Finally, the hPSC Scorecard Analysis software (Life Technologies) was applied to analyze 94 genes relating to the trilineage differentiation potential.

Please cite this article in press as: Wang et al., Biomaterial-minimalistic photoactivated bioprinting of cell-dense tissues, Cell (2026), https://doi.org/10.1016/j.cell.2025.11.012

hCO induction and neuronal differentiation, and hSpO induction

The hCOs were generated as previously described.[65] EBs were induced into neural lineage using Essential 6 medium (ThermoFisher) supplemented with two SMAD pathway-inhibitors SB431542 (10 μM) and dorsomorphin (2.5 μM, Sigma-Aldrich). On day 6, the organoids were transferred to the neural progenitor cell (NPC) medium containing neurobasal-A medium (ThermoFisher), B-27 supplement minus vitamin A (ThermoFisher), GlutaMAX supplement (1:100), penicillin-streptomycin (1:100, ThermoFisher), 20-ng mL^{-1} epidermal growth factor (EGF, R&D Systems), and 20-ng mL^{-1} fibroblast growth factor 2 (FGF2, R&D Systems). The NPC medium was changed every other day from day 15. From day 25, the NPC medium was supplemented with 20-ng mL^{-1} BDNF and 20-ng mL^{-1} neurotrophin-3 (NT3, PeproTech). From day 45, only NPC medium was used for medium-changes every 4 days. hCOs were imaged on days 5, 15, and 30 after differentiation with an inverted microscope. To quantify the representative genes of NPCs (*FOXG1* and *SOX2*) and neuronal cells (*SLC17A7* and *MAP2*), hCOs were collected at 25, 50, and 75 days after differentiation, followed by RNA-isolation and qRT-PCR. Detailed primer information is listed in Table S1. Furthermore, on day 75 after neuronal differentiation, hCOs generated from ESCs and ESC CLINK were collected, fixed, permeabilized, and blocked by 4 w/v% PFA, 0.03 v/v% Triton X-100, and 5 w/v% BSA, respectively. Subsequently, the samples were incubated with the primary antibodies against NeuN (Abcam, USA) and then incubated with the corresponding secondary antibodies at room temperature for 2 h, which was followed by DAPI counterstaining of the nuclei. The samples were visualized using a confocal microscope.

The hSpOs were generated as previously described(Andersen et al., 2019). In brief, Essential 6 medium supplemented with dorsomorphin (2.5 μM) and SB431542 (10 μM) was used from day 1 to day 6. WNT-activator CHIR 99021 (3 μM; Selleckchem, USA) was added from day 4 to day 18. On day 6, spheroids were transferred to a neural medium containing retinoic acid (0.1 μM), EGF (20 ng mL^{-1}), and FGF-2 (10 ng mL^{-1}), with the SAG (0.1 μM) added from day 11. Starting on day 7, the medium was changed every other day. On day 19, hSpOs were transferred to a neural medium supplemented with N-2 supplement, BDNF (20 ng mL^{-1}), insulin-like growth factor 1 (IGF-1, 10 ng mL^{-1}; Peprotech), L-ascorbic acid (200 nM; Wako Pure Chemical Industries, Japan), and cAMP (50 nM; Sigma-Aldrich). For hSpO-induction, the Notch pathway-inhibitor *N*-[*N*-(3,5-difluorophenacetyl)-l-alanyl]-s-phenylglycinet-butylester (DAPT, 2.5 μM; StemCell Technologies) was added on days 19, 21, and 23. From day 43 onward, the medium was changed every 4-5 days.

Rheological characterizations of CLINK

Rheology measurement was performed on a Discovery HR-3 rheometer (TA Instruments, USA) with a 40-mm-diameter parallel plate geometry and a gap height of 0.8 mm. 2 mL of NIH/3T3 CLINK or unmodified cells were added to the plate and trimmed with a spatula before the measurements. Apparent viscosities as a function of shear rate were measured *via* steady-state flow-sweeps from shear rates of 0.01 to 200 s^{-1}. Amplitude-sweeps were measured as a function of shear strain (0.01-2,000%) *via* oscillation experiments at a fixed frequency of 1 Hz and a temperature of 28 °C.

DLP bioprinter

A top-down DLP-based bioprinter was built in-house by placing the PRO4500 Optical Engine (Wintech Digital Systems Technology, USA) over the CLINK vat, where the patterns were projected onto the top surface of the CLINK (Figure S3A). The light density projected onto the vat area was measured with a photometer (IDEAL Electrical, USA) as 16.8 lumens (= 0.443 mW cm^{-2}). The build platform was fabricated from acrylic pieces and submerged into the CLINK, with a glass slide (Carolina, USA) placed on top to allow the bioprinted construct to adhere during and after bioprinting. The z-axis position of the platform was controlled using a stepper-motor linear driver (TOAUTO, USA) with a 100-μm layer thickness-adjustment. A limit-switch was incorporated into the bioprinter to restrict platform-movement and standardize the z-axis starting point. Custom software, developed in MATLAB (v2020, MathWorks, USA), was used to control the DLP bioprinting process, including layer thickness-adjustments. Digital models were designed in SolidWorks (Dassault Systèmes, France), which were further sliced into a series of 2D images at a thickness of 100 μm using the open-source DLP slicer (https://formlabs.com/blog/open-source-dlp-slicer, Formlabs, USA).

Evaluations of printability

Square patterns with side lengths ranging from 0.25, 0.6, 1, to 1.75 mm were DLP-bioprinted to assess the printability of CLINK. The NIH/3T3 CLINK was prepared with 0.5/5-mM Ru/SPS, 1.0 w/v% photoabsorber, and various NIH/3T3 cell densities (1×10^7, 1×10^8, and 1×10^9 cells mL^{-1}), or different concentrations of photoinitiator (0.25/2.5-mM, 0.5/5-mM, 0.75/7.5-mM, and 1/10-mM Ru/SPS), or varying concentrations photoabsorber (0 w/v%, 0.5 w/v%, 1 w/v%, and 1.5 w/v% Ponceau 4R) were assessed. Each formulation was bioprinted with 5-s crosslinking intervals to investigate the influences of cell density, photoinitiator amount, and photoabsorber concentration on printability and printing fidelity, respectively. Additionally, printing time was varied from 1 to 8 s to explore their effects on printability and curing thickness using the NIH/3T3 CLINK containing 0.5/5-mM Ru/SPS and 1 w/v% photoabsorber. Optical images of the bioprinted constructs were captured using a fluorescence microscope (Nikon, Japan), and the printed areas and thicknesses were measured with ImageJ.

The differences were compared between the bioprinted area of each square and the designed digital pattern, where the closer value indicated better printing fidelity. The squares bioprinted with CLINK of NIH/3T3 fibroblasts containing the photoinitiator system, 0.5-mM/5-mM Ru/SPS, revealed larger bioprinted areas than their corresponding designed pattern sizes

(Figures 3A and S2A). In previous studies including those of our own, Ponceau 4R was reported as a cytocompatible photoabsorber to attenuate excessive light and control the optical penetration length in DLP bioprinting, aiming to obtain the desired curing depth and printing fidelity.[22–24,66] Indeed, the presence of photoabsorber Ponceau 4R resulted in a better match of the pattern size/shape to the theoretical values, which was positively correlated to photoabsorber concentrations between 0 to 1.5 w/v%. The squares of 0.25 × 0.25 mm^2 were only partially bioprinted with the CLINK containing 1.5 w/v% photoabsorber. Thus, 1 w/v% Ponceau 4R was selected as the proper photoabsorber amount to achieve best printing fidelity and proper printability. Moreover, the squares bioprinted by the CLINK with more than 0.5-mM/5-mM Ru/SPS displayed diminished fidelities, attributing to over-curing by the increased photoinitiator concentrations (Figure S2B). To investigate whether the printing fidelity and curing thickness could be tuned by different crosslinking times, CLINK of NIH/3T3 fibroblasts consisting of 0.5-mM/5-mM Ru/SPS and 1 w/v% Ponceau 4R was bioprinted under the exposure from 1 to 8 s. With the curing time less than 2 s, equal to the irradiation power of 0.886 mJ cm^{-2}, the cells could not be properly patterned (Figure S2C), which suggested 2 s as the threshold power for CLINK bioprinting. When the curing time was increased to 2 s or beyond, the square patterns were obtained, implying the ability of rapid, visible-light curing for the CLINK. The biomaterial-minimalistic bioprinted constructs possessed high cell densities, and they presented clear edges when the CLINK was exposed to light for 5 to 8 s. Meanwhile, as the printing time was prolonged from 5 to 8 s, the curing thickness was elevated from 102.56 to 153.85 μm. Using the optimized NIH/3T3 CLINK containing 0.50-mM/5.00-mM Ru/SPS and 1 w/v% Ponceau 4R together with the exposure time of 5 s, the high-cell-density constructs were readily observed only when the cells were involved in the CLINK at a high density (~1 × 10^9 cells cm^{-3}, Figure S2D). As calculated by the close-packed sphere model (solid volume fraction of approximately 74%) and typical cellular diameters of 8-15 μm, the cell density in our biomaterial-minimalistic bioprinted constructs would fall within the range of 0.42 × 10^9 to 2.76 × 10^9 cells mL^{-1}, orders of magnitude higher than most other previous demonstrations using conventional biomaterial-rich bioinks.

To study the influence of curing time and light intensity on cell viability, NIH/3T3 CLINK containing 0.5/5-mM Ru/SPS and 1.0 w/v% photoabsorber was bioprinted with 14 s at 0.06 mW cm^{-2} and 2 s at 0.44 mW cm^{-2}. The viabilities of bioprinted cells were measured with live/dead staining (ThermoFisher) captured on day 1 post-bioprinting. In detail, the constructs were rinsed with PBS and incubated with 2-μM of calcein-AM and 4-μM of ethidium homodimer-1 for 30 min, followed by observation with fluorescence microscopy (Zeiss). Both samples bioprinted with a longer curing duration at a lower light intensity (14 s at 0.06 mW cm^{-2}; 0.84 mJ cm^{-2}) and a shorter curing duration at a higher light intensity (2 s at 0.44 mW cm^{-2}; 0.88 mJ cm^{-2}) revealed satisfactory cell viabilities after 1 day of culture (Figure S2E). The results illustrated that the CLINK of high cell densities enabled us to achieve good printing fidelity and accomplish desired feature resolutions reproducibly, through the DLP-based biomaterial-minimalistic cell-dense bioprinting methodology that we have developed.

Biomaterial-minimalistic DLP bioprinting

Before bioprinting, the cells were stained with CellTrackers (Invitrogen) for visualization and then modified with the OMHA linker. The planar patterns were projected onto the CLINK for 5 s for each bioprinting session, followed by washing the bioprinted constructs with PBS to remove the uncrosslinked CLINK. The multi-cell bioprinting process was conducted by printing each type of cells under different patterns. The bioprinted constructs were imaged directly following bioprinting using a fluorescence microscope. For the breast cancer model, HUVEC CLINK was bioprinted in a vascular pattern, followed by bioprinting MDA-MB-231 CLINK with a square pattern surrounding the vasculature. After washing with PBS to remove uncrosslinked CLINK, the bioprinted breast cancer model was further coated with 0.25 w/v% alginate (Sigma-Aldrich), followed by culturing with 50% EGM-2 and 50% DMEM containing 10 v/v% FBS. After 1 day of culture, the bioprinted constructs were incubated for a few minutes in 0.01-M EDTA (Sigma-Aldrich) solution to remove alginate rapidly, and then rinsed with PBS for further cultivation. The breast cancer model was imaged on 0, 3, 5, and 7 days post-bioprinting using a fluorescence microscope.

For 3D biomaterial-minimalistic DLP bioprinting, the NIH/3T3 CLINK was transferred into the vat before bioprinting, followed by lowering the build platform to the initial position (100 μm under the bioink surface). Our customized software realized complete control over the image-projection and the movement of the build plate. The 3D construct was bioprinted with a 5-s crosslinking time for each layer by lowering the platform layer-by-layer (100 μm of thickness for each layer). For bioprinting 3D constructs embedded with hollow channels, uncrosslinked NIH/3T3 CLINK within channels was immediately washed with PBS after bioprinting. The bioprinted samples were collected *via* freezing at -20 °C overnight and cutting to visualize cross-sections. F-actin staining was performed by fixation, permeabilization, blocking, incubating with the primary antibody against F-actin (ThermoFisher) and DAPI. The samples were then visualized using a confocal microscope. The same models of hollow channels were further applied to multi-material biomaterial-minimalistic DLP bioprinting, where CLINKs containing two colors of CellTracker-stained NIH/3T3 fibroblasts were bioprinted and PBS washing was conducted between different CLINKs. The bioprinted constructs were imaged directly following bioprinting using a fluorescence microscope, from the top and side views cut at relevant hollow channel positions. To further visualize the internal hollow structures within the bioprinted 3D constructs, we perfused the painting pigment (Easyou, China) solutions into the open channels. Meanwhile, the bioprinted 3D samples were fixed with 4 w/v% PFA, stepwise dehydrated in ethanol, blocked in paraffin wax, cut into thin sections along with the vertical direction to the channels, and placed on glass slides. The slides were dewaxed and stained with an H&E Stain Kit (Abcam) according to the manufacturers' instructions, which were photographed under a light microscope (Zeiss). A more sophisticated 3D multi-material construct (a voxelated 3D cube) was also bioprinted, with NIH/3T3 CLINKs stained with three different colors of CellTrackers. Every layer of the construct was applied with distinct patterns of three CLINKs, with a 10-s

Please cite this article in press as: Wang et al., Biomaterial-minimalistic photoactivated bioprinting of cell-dense tissues, Cell (2026), https://doi.org/10.1016/j.cell.2025.11.012

exposure time for each. PBS washing was conducted between different CLINKs to remove uncrosslinked CLINKs and avoid contamination.

Fabrication of liver tissues with biomaterial-minimalistic DLP bioprinting

To model the hepatic lobule structure, a two-step biomaterial-minimalistic bioprinting approach was used. First, the HUVEC CLINK was bioprinted to form the vascular sinusoids. Following this, the HepG2/C3A CLINK was bioprinted with a 10-s crosslinking time. For comparison, HepG2/C3A-only biomaterial-minimalistic constructs were bioprinted under the same pattern, with 10-s crosslinking time. Moreover, biomaterial-rich tissues containing HepG2/C3A ($\sim 8 \times 10^6$ cells mL^{-1}) and 10 w/v% GelMA were bioprinted with a 30-s printing time. The biomaterial-minimalistic, cell-dense constructs were subsequently coated with 0.25 w/v% alginate and cultured in a mixture of DMEM containing 10 v/v% FBS and EGM-2 (1:1). After 1 day of culture, the bioprinted constructs were incubated in 0.01-M EDTA solution to rapidly remove alginate and washed with PBS for further cultivations.

To visualize the cells post-bioprinting, HUVECs and HepG2/C3A cells were pre-stained with CellTrackers prior to bioprinting. Fluorescence micrographs of bioprinted samples were captured on days 1, 3, 5, and 7. Cell viabilities were also assessed using live/dead staining at these time points after bioprinting. Cellular metabolic activities were measured *via* an MTS assay with the CellTiter 96® AQueous Assay (Promega, USA), according to manufacturer's instructions. For immunostaining, the samples were collected at 7 days after bioprinting, fixed with 4 w/v% PFA, permeabilized with 0.03 v/v% Triton X-100, and blocked with 5 w/v% BSA. Analyses of gene-expressions were conducted on the samples on day 7. Total RNAs were extracted using TRIzol, followed by cDNA-syntheses and qRT-PCR with primers obtained from Integrated DNA Technologies (USA). Detailed primer information is listed in Table S2. Moreover, the supernatants from cell cultures on 5 and 10 days were harvested, stored at -80 °C, and analyzed for ALB-secretion using an ELISA kit (Abcam), according to manufacturer's instructions.

To fabricate and assemble the medium-throughput chip, the entire chip was designed in SolidWorks. Molds were manufactured by laser-engraving and cutting acrylic sheets (McMaster-Carr, USA) using a VLS 2.30 Desktop Laser (Universal Laser Systems, USA). Polydimethylsiloxane (PDMS, Dow, USA) monomer was mixed with its curing agent in a 10:1 ratio and cast into the molds. By adding two pieces of properly cut PDMS above and below the chip layer, the chip was sealed between the top and bottom acrylic frames using multiple screws distributed across the device. The biomaterial-minimalistic bioprinting within the medium-throughput design began by filling the vat with the HepG2/C3A CLINK containing 0.5/5-mM Ru/SPS and 1 w/v% photoabsorber. An array of hepatic lobule patterns was projected, completing the bioprinting of all the patterns within the entire chip simultaneously under 10-s exposure. The bioprinted samples in the medium-throughput chip were images under a microscope.

To evaluate cell viability after exposure to DOX, liver units bioprinted in the medium-throughput chip were treated with DOX (Cayman Chemical, USA) on day 1 post-bioprinting. Varying concentrations of DOX (0, 50, 100, 150, and 200 μM) were tested at two different time points (24 and 48 h). Following DOX-exposure, a CellTiter-Glo® Luminescent Cell Viability Assay (Promega) was conducted as the instructions of manufacturer. Briefly, the cell-lysis reagent was added to samples to release intercellular adenosine triphosphate (ATP) into the surrounding solution. Then, a secondary reagent was added that luminesces on interaction with ATP, which could be detected by a luminescence plate reader.

The 3D liver tissues, with or without embedded channels, were bioprinted using 15-s crosslinking time for each 200-μm layer of the GelMA bioink, or a 10-s crosslinking time for each 200-μm layer of the HepG2/C3A CLINK. Four different 3D constructs, including GelMA, GelMA with HepG2/C3A, HepG2/C3A CLINK without channels, and HepG2/C3A CLINK with channels, were fabricated and further evaluated *in vivo*. For the *in vitro* investigations, the supernatants from liver tissue cultures were collected on 1, 5, and 10 days and stored at -80 °C. Quantifications of ALB and AFP secretions were performed using ELISA kits for ALB (Abcam) and AFP (Abcam), respectively, according to manufacturers' instructions. In the *in vivo* studies (approved by the Institutional Animal Care and Use Committee of Brigham and Women's Hospital, 2016N000162), the recipient athymic nude mice (7-week-old female, Charles River Laboratories, USA) were anesthetized following a standard isoflurane protocol, and mesenteric parametrial transplantation was performed on a heating pad set to 37 °C to maintain body temperature. After anesthesia, a 1-2 cm of incision was made on the lateral abdominal skin of each animal, and the peritoneum was carefully opened to expose the parametrial fat pad. The bioprinted constructs were gently placed on the fat pad, secured in place, and the peritoneum and skin were closed in layers to complete the procedure. Serum of the transplanted mice was further examined for the secretion of human ALB (Bethyl, USA), human fibronectin (Bethyl), and human alpha-1 antitrypsin (Boster, USA) by ELISA on days 3 and 7 post-implantation. At the end of the experiments (7 days), the animals were sacrificed, and the tissues were harvested from the intraperitoneal space. The explants were then fixed in 4 w/v% PFA for 16 h and further sectioned. Immunofluorescence staining of both *in vitro* and *in vivo* samples was performed by incubating the tissues with the primary antibodies against ALB (Abcam), E-cadherin (Abcam), CYP1A2 (Abcam), or CYP3A4 (ThermoFisher) overnight at 4 °C, followed by incubation with the corresponding secondary antibodies and DAPI-counterstaining of the nuclei. Finally, the samples were visualized using a confocal microscope, and the IODs of fluorescence signals were analyzed with ImageJ.

Modeling of neural circuits *via* biomaterial-minimalistic DLP bioprinting of human ESC-derived neurons

Neurons were all bioprinted and cultured on laminin- and poly-D-lysine-precoated glass coverslips. The two-step biomaterial-minimalistic bioprinting approach was performed to model the neural circuit, in which cortical neuron CLINK was first bioprinted, followed by the bioprinting of motor neuron CLINK with 5-s crosslinking time each. The biomaterial-minimalistic bioprinted constructs

were rinsed with PBS and coated with 0.25 w/v% alginate, and cultured in the neuronal cell culture medium. After 1 day, the bioprinted constructs were incubated in 0.01-M EDTA solution for a few minutes to remove alginate rapidly and washed with PBS for further cultivation. The biomaterial-minimalistic DLP-bioprinted neural circuit samples were fixed, permeabilized, and blocked with 4 w/v% PFA, 0.03 v/v% Triton X-100, and 5 w/v% BSA, respectively. The samples were incubated with the primary antibodies to TUJ1 (Abcam), CamKII (Abcam), Map-2 (Abcam), and Isl-1 (Millipore, USA) overnight at 4 °C, and then incubated with the corresponding secondary antibodies at room temperature for 2 h, which was followed by DAPI-counterstaining of the nuclei. The samples were then visualized using confocal microscopy.

For optogenetics stimulation and MEA-recording, we delivered pLenti-CaMKIIa-hChR2(H134R)-mCherry-WPRE (Addgene, USA) into cortical neurons. ChR2-infected cortical neurons and motor neurons were separately bioprinted on the two sides of MEA well plates (Axion Biosystems, USA), which were precoated with laminin and poly-D-lysine. Recordings of extracellular spikes (action potentials) were performed using the Axion Biosystems MEA plate system (Maestro, Axion BioSystems) and maintained at a temperature of 37 °C. Neuronal activities were measured at 7 days after bioprinting. The stimulations were conducted as three blue exposures (100 pulses at 485 nm) each separated by 20 s. Standard settings were maintained for all Axion MEA-recordings and analyses. It was confirmed that similar results across a wide range of action potential threshold and cluster similarity radius settings were obtained. Data was analyzed using the Axion Integrated Studio 2.4.2 and the Neural Metric Tool (Axion Biosystems).

CardioChamber modeling *via* biomaterial-minimalistic DLP bioprinting of human iPSC-derived hCMs

The human iPSCs were maintained in mTeSR medium on Matrigel-coated plates. hCM differentiation from iPSCs was carried out using a commercially available protocol and a defined differentiation medium (StemCell Technologies). From day 8, differentiated cells were cultured with maintenance medium (StemCell Technologies) and changed every 2 days. The hCMs were characterized by the expression of cTnT using both confocal microscopy and flow cytometry (CytoFLEX S, Beckman Coulter, USA).

For the 3D bioprinting of CardioChambers, the hCM CLINK was prepared and bioprinted with 10-s crosslinking time for the first three layers and 8-s for the remaining layers. For calcium transient-imaging of the CardioChambers, the cell membrane-permeable calcium ion fluorescent probe Fluo-4 AM (ThermoFisher) was used according to the manufacturer's protocol. Briefly, CardioChambers were incubated with the working solution for 30 min, followed by full de-esterification and calcium transient imaging using a Leica Incubator i8 workstation (Leica, Germany). Data-analyses were performed using ImageJ and Origin (Version 9.8.0.200, OriginLab, USA). After 7 days of culture post-bioprinting, CardioChambers were fixed with 4 w/v% PFA for 1 h before embedded in the optimal cutting temperature (OCT, Tissue-Tek, USA) compound. Transversal sections (8-μm thickness) were used for histological staining and fluorescence immunostaining for cTNT and MYL7 to confirm the chamber-like structure and cardiac functions.

Skin-excisional wound model and implantation of bioprinted constructs

Four types of constructs were fabricated using biomaterial-minimalistic DLP-bioprinting: MSCs in GelMA ($\sim 8 \times 10^6$ cells mL^{-1}), as well as CLINKs ($\sim 1 \times 10^9$ cells mL^{-1}) of MSCs, MSCs/ECs/MSCs in triple layers, and MSCs/ECs patterned in RAS. For visualization purpose, we also bioprinted CellTracker-labeled MSCs (yellow) and GFP-HUVECs (green). All procedures involving animals were approved by the IACUC of Brigham and Women's Hospital (2023N000108). Mouse skin-excisional wound-healing studies were performed as previously described.[67] Briefly, 8-week-old female C57BL/6 mice (Charles River Laboratories) were anaesthetized using aerosolized isoflurane and sustained for whole procedure. A sterilized 6-mm biopsy punch was then applied to create full-thickness excisional wounds on either side of the dorsal midline. Subsequently, the created wounds were sealed with sterile Tegaderm film (3M Inc., USA) and respectively fixed on the silicone ring with sutures. At the culmination of the wound healing experiment (day 21 or 25), the mice were euthanized by isoflurane-overdose and cervical dislocation and imaged with a digital camera. On the predefined times (days 3, 7, 14, and 21) after the wounds were created, images of healed wounds were taken, and the mice were euthanized to excise the healed skin. The skins were processed to section with 8-μm thickness and then stained with H&E or Masson's trichrome (StatLab, USA) following the production protocols. Tissue sections were fixed, blocked, and stained with primary antibody (CD31 or K15, Abcam) overnight at 4 °C, followed by incubation with the corresponding secondary antibody and DAPI counterstaining of the nuclei. The stained tissue sections were finally visualized by a confocal microscope (LSM880, Zeiss) and the acquired images were further analyzed with ImageJ.

Triplicates of collected tissues from each group were further analyzed for the bulk RNA-seq procedure. Library quality was evaluated by Qubit fluorometer 3.0 (ThermoFisher) and Agilent 4200 system (Agilent Technologies, USA). Subsequently, the libraries were sequenced by the Illumina NovaSeq 6000 (Illumina, USA). Raw reads were trimmed by Trimmomatics[68] to remove low-quality basses and adapters, then aligned to mouse genome (mm10), using HISAT (version 2.1.0)[69] with default parameters. Annotation file, version M20 in gtf format for mouse, was downloaded from GENCODE Database (https://www.gencodegenes.org). Then featureCounts (v1.5.0-p3) was used to count the reads numbers for each gene.[70] To calculate the transcripts per million (TPM) values of genes, the read counts were first divided by the length of each gene in kilobases, or reads per kilobase (RPK). Then, all the RPK values were summed in a sample and divided by 1,000,000 to obtain the "per million" scaling factor. Finally, the RPK value for each gene was divided by this "per million" scaling factor. DEGs of the two groups (triplicates per group) was obtained using the DESeq2 R package (v1.32.0).[71] A DEG was considered significantly enriched when its GO terms and KEGG pathways had a corrected p value less than 0.05. Chord plots and heatmap of DEGs were plotted by ggplot2 (v3.4.2).[72]

Please cite this article in press as: Wang et al., Biomaterial-minimalistic photoactivated bioprinting of cell-dense tissues, Cell (2026), https://doi.org/10.1016/j.cell.2025.11.012

QUANTIFICATION AND STATISTICAL ANALYSIS

The data were presented as means ± standard deviations (SDs). All statistical analyses were performed with one-way ANOVA or two-way ANOVA followed by a Tukey's Honest Significant Difference test or a two-tailed student's t-test. $p < 0.05$ was considered statistically significant. GraphPad Prism software (v8.2.0) was used for all statistical analyses, and Microsoft Excel (v16.54) was used for data-handling.

Supplemental figures

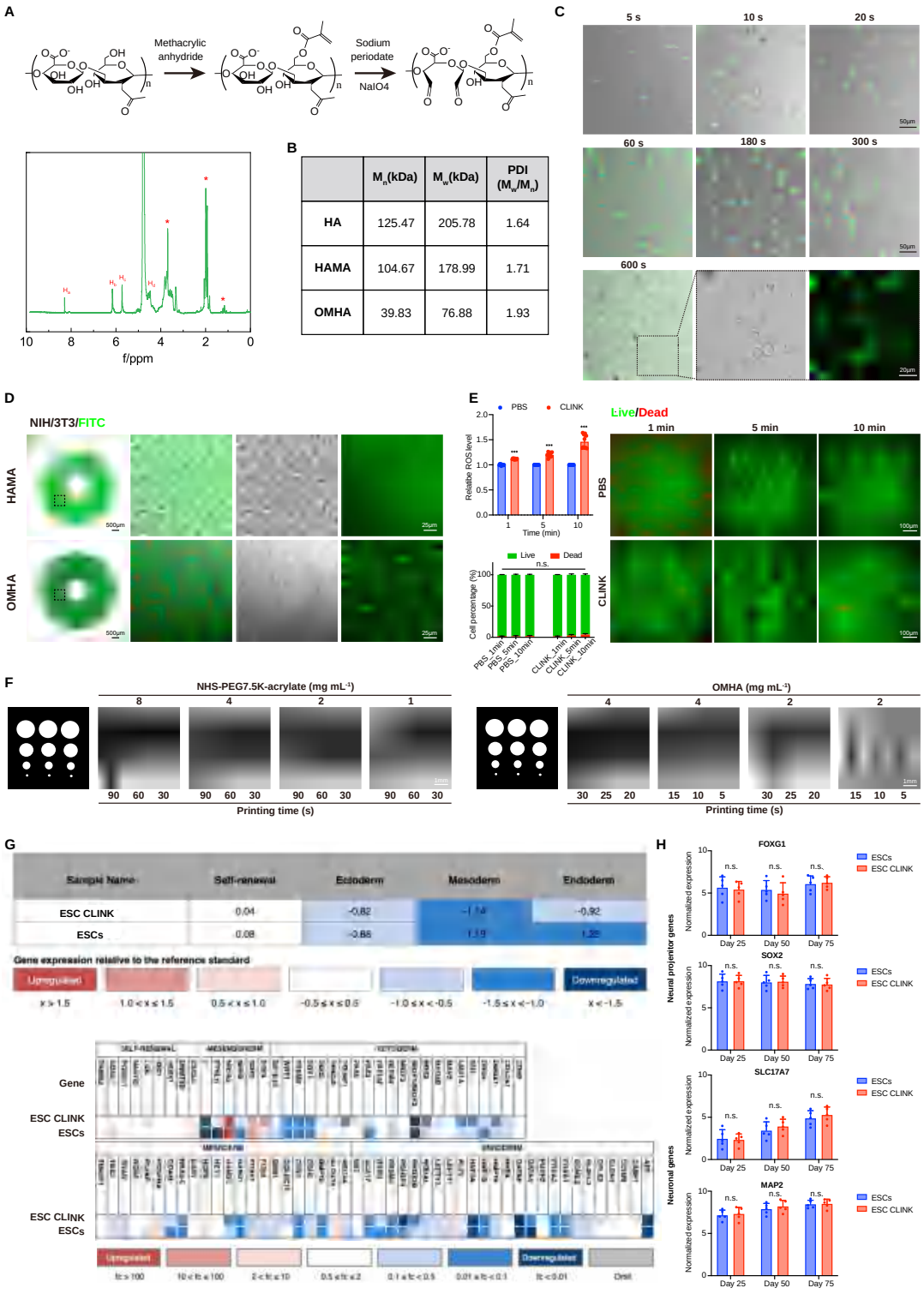

	M_n(kDa)	M_w(kDa)	PDI (M_w/M_n)
HA	125.47	205.78	1.64
HAMA	104.67	178.99	1.71
OMHA	39.83	76.88	1.93

(legend on next page)

Figure S1. Linker characterizations and investigation of linker influence on cellular behavior, related to Figure 2 and STAR Methods

(A) ^{1}H-NMR spectra of OMHA with marked peak assignments and areal integration.

(B) GPC analyses of MW and PDIs of HA, HAMA, and OMHA.

(C) Superimposed images of bright-field and fluorescence micrographs for OMHA conjugation on NIH/3T3 fibroblasts. The suspension cells were reacted with 1% w/v FITC-OMHA linker for 5, 10, 20, 60, 180, 300, and 600 s.

(D) Comparison of linker distributions for HAMA and OMHA. Fluorescence images of FITC-HAMA and FITC-OMHA revealing their localizations after DLP bioprinting.

(E) Evaluations of ROS-productions and cell viabilities of linker influence on NIH/3T3 fibroblasts. Quantitative results of ROS assay showing relative ROS levels of NIH/3T3 fibroblasts before and after 1, 5, and 10 min of linker reaction (top-left). Fluorescence micrographs showing live (green)/dead (red) staining of NIH/3T3 fibroblasts before and after 1, 5, and 10 min of linker reaction, with corresponding quantitative analyses of live/dead cell percentages (bottom-left).

(F) Bioprinted patterns with cells modified by NHS-PEG7.5K-acrylate or OMHA at different concentrations and photocrosslinking times.

(G) Averaged differentiation potential differences of EBs formed by ESCs or ESC CLINK at day 7. Colors correlate to the fold changes in expressions relative to the corresponding reference sets. Overall differentiation potential differences of EBs, and each gene expression in the self-renewal, ectoderm, mesoderm, and endoderm genes, are shown.

(H) Expression levels of neural progenitor genes (*FOXG1* and *SOX2*) and neuronal genes (*SLC17A7* and *MAP2*) of hCOs differentiated from ESCs and ESC CLINK on days 25, 50, and 75.

In (E), top-left, $n = 10$; two-way ANOVA; $^{***}p < 0.001$ (compared with the group of PBS at the same time point). Bottom-left, $n = 3$; two-way ANOVA; n.s., non-significant difference. In (G), $n = 5$; one-way ANOVA; n.s., no significance (compared with the group of ESCs).

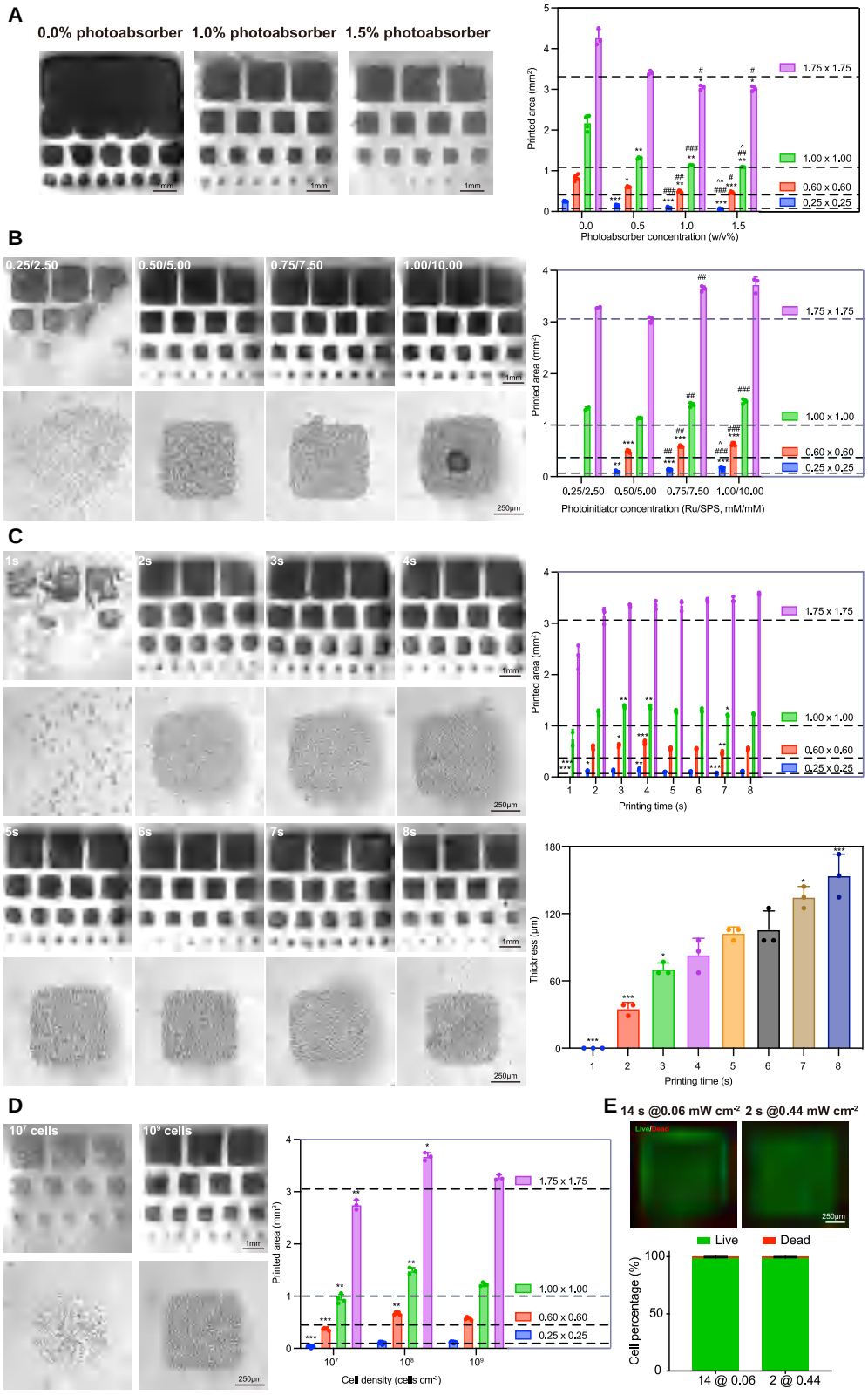

(legend on next page)

Figure S2. Printability optimizations of biomaterial-minimalistic DLP bioprinting with CLINKs, related to Figure 3

(A) The effects of photoabsorber concentration on printing fidelity of NIH/3T3 CLINK containing 0.50/5.00 mM Ru/SPS and various concentrations of photoabsorber Ponceau 4R. The 1-w/v% photoabsorber condition is the same as in Figure 3A.

(B) The effects of photoinitiator concentration on printing fidelity of NIH/3T3 CLINK containing 1 w/v% of Ponceau 4R and bioprinted within 5 s. Zoomed-in micrographs of the squares illustrate the high cell densities within the bioprinted biomaterial-minimalistic structures.

(C) Effects of printing time on printing fidelity and crosslinking thickness of NIH/3T3 CLINK containing 0.5/5-mM Ru/SPS and 1 w/v% Ponceau 4R. Zoomed-in micrographs of the squares illustrate the high cell densities within the bioprinted biomaterial-minimalistic structures.

(D) Influence of cell density on printing fidelity of NIH/3T3 CLINK containing 0.5/5 mM Ru/SPS and 1 w/v% Ponceau 4R with 5-s printing time. Zoomed-in micrographs of the squares illustrate the high cell densities within the bioprinted biomaterial-minimalistic structures.

(E) Fluorescence micrographs showing live (green)/dead (red) staining of biomaterial-minimalistic bioprinted NIH/3T3 CLINK under similar irradiation doses but with various light intensities and photocrosslinking durations on day 1, with corresponding quantitative analyses of the percentages of live/dead cell numbers. In (A), $n = 3–8$; two-way ANOVA; $^{*}p < 0.05$, $^{**}p < 0.01$, $^{***}p < 0.001$ (compared with the group of 0.0 w/v% photoabsorber); $\#p < 0.05$, $\#\#p < 0.01$, $\#\#\#p < 0.001$ (compared with the group of 0.5 w/v% photoabsorber); $\hat{}p < 0.05$, $\hat{}\hat{}p < 0.01$ (compared with the group of 1.5 w/v% photoabsorber). In (B), $n = 3–8$; two-way ANOVA; $^{**}p < 0.01$, $^{***}p < 0.001$ (compared with the group of 0.25/2.5 mM/mM of photoinitiator); $\#\#p < 0.01$, $\#\#\#p < 0.001$ (compared with the group of 0.5/5 mM/mM of photoinitiator); $\hat{}p < 0.05$ (compared with the group of 0.75/7.50 mM/mM of photoinitiator). In (C), printed area, $n = 3–8$; two-way ANOVA; $^{*}p < 0.05$, $^{**}p < 0.01$, $^{***}p < 0.001$ (compared with the group of 5-s printing time); thickness, $n = 3$; one-way ANOVA; $^{*}p < 0.05$, $^{***}p < 0.001$ (compared with the group of 5-s printing time). In (D), $n = 3–8$; two-way ANOVA; $^{*}p < 0.05$, $^{**}p < 0.01$, $^{***}p < 0.001$ (compared with the group of high-cell-density).

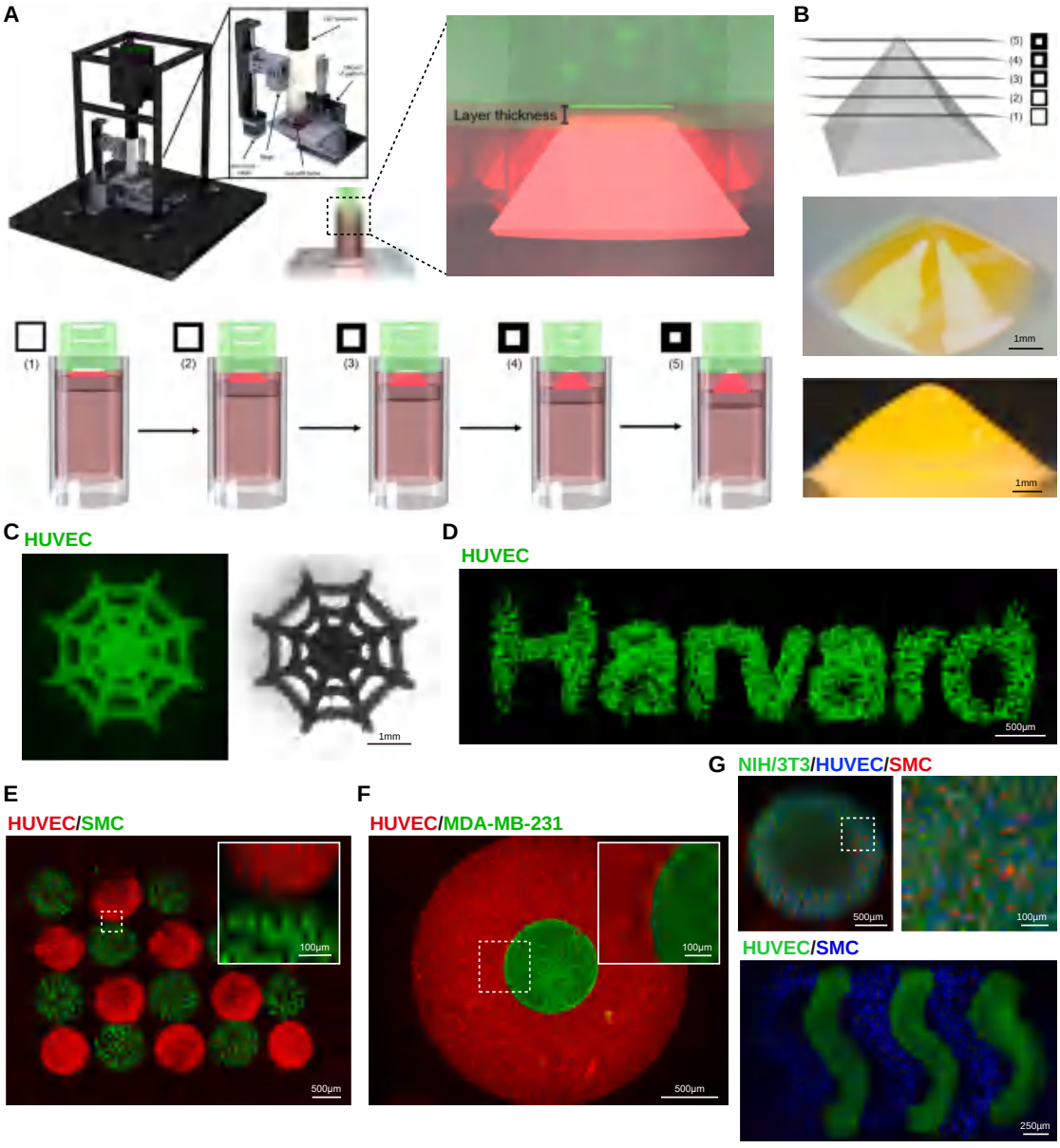

Figure S3. Bioprinter setup, bioprinting process, and biomaterial-minimalistic DLP-bioprinted planar high-cell-density structures, related to Figure 3

(A) Schematic showing all the main hardware components utilized. Projections of sliced images with synchronized downward motor/stage movements were achieved where the layer thickness was tightly controlled.

(B) The slicing process (pyramid structure taken as an example). Photographs show a representative bioprinted construct.

(C) Fluorescence micrograph showing a spider web pattern bioprinted with GFP-HUVEC CLINK (green) with fine tips.

(D) Fluorescence micrograph showing the word of Harvard bioprinted with HUVEC CLINK (green).

(E) Fluorescence micrograph showing a multicell dot array bioprinted with HUVEC (red) and human umbilical vein SMC (green) CLINKs.

(F) Fluorescence micrograph showing a tumor model bioprinted with an MDA-MA-231 CLINK (green) circle surrounded by a HUVEC CLINK (red) ring.

(G) Fluorescence micrograph showing a heterogeneous circle bioprinted with NIH/3T3 (green), HUVEC (blue), and human umbilical vein SMC (red) CLINKs, as well as a vascular pattern bioprinted with GFP-HUVEC (green) and human umbilical vein SMC (blue) CLINKs lined up against each other.

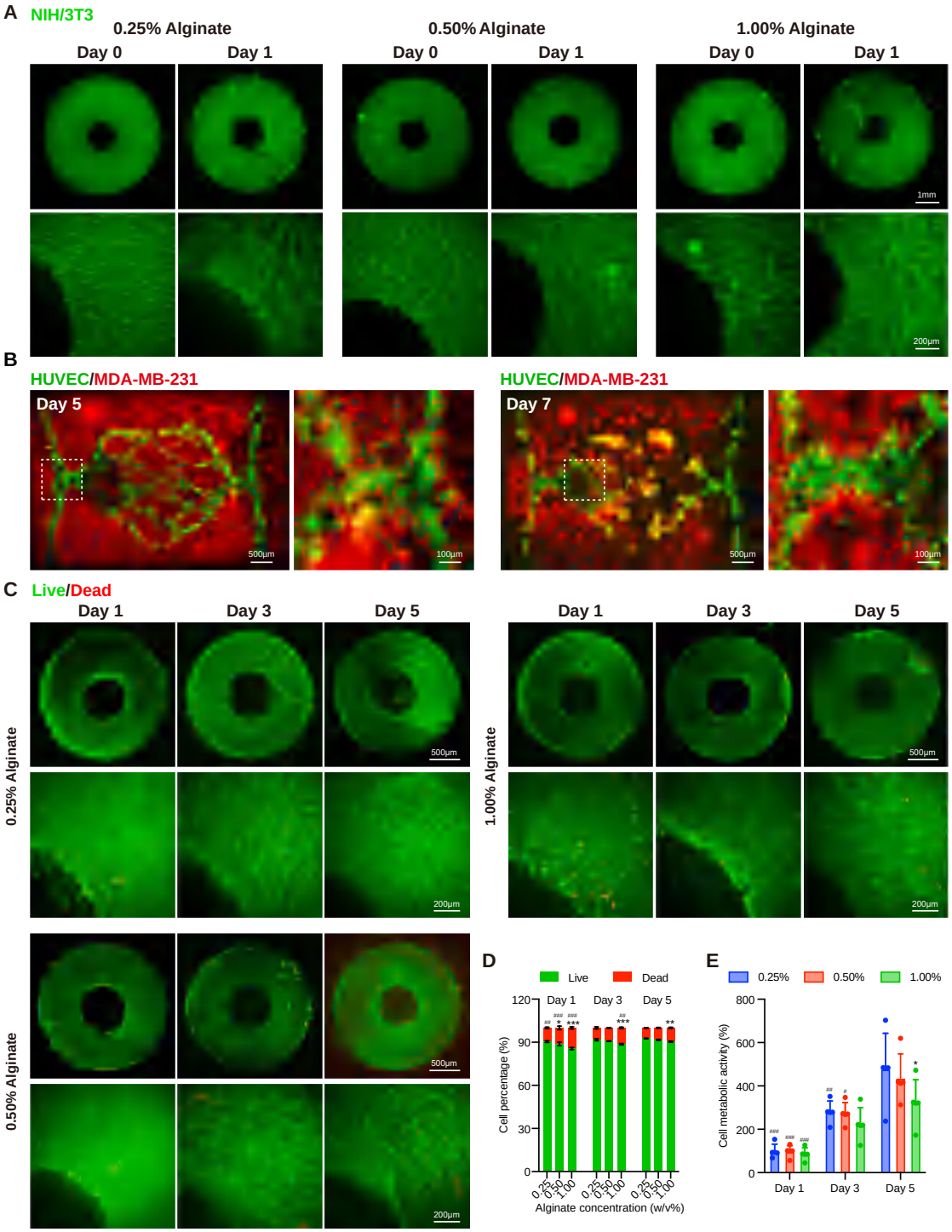

Figure S4. Evaluation of cell behavior of bioprinted CLINKs with varied concentrations of alginate coating, related to Figure 3

(A) Bioprinted ring constructs composed of CellTracker-labeled NIH/3T3 CLINK (green) with alginate coating concentrations of 0.25, 0.50, and 1.00 w/v% on days 0 and 1.

(B) Fluorescence micrograph showing longer-term culture of bioprinted endothelialized breast cancer model with HUVEC (green) and MDA-MA-231 (red) CLINKs.

(C) Fluorescence micrograph showing live (green)/dead (red) staining of bioprinted NIH/3T3 CLINK with alginate coating concentrations of 0.25, 0.50, and 1.00 w/v% on days 1, 3, and 5.

(D) Corresponding quantitative analyses of the percentages of live/dead cell ratios.

(legend continued on next page)

(E) Quantitative results of MTS assays showing metabolic activities of bioprinted NIH/3T3 CLINK.

In (D), $n = 3$; two-way ANOVA; $^{*}p < 0.05$, $^{**}p < 0.01$, $^{**}p < 0.001$ (compared with the group of 0.25 w/v% alginate at the same time point); $\#\#p < 0.01$, $\#\#\#p < 0.001$ (compared with the same group at day 5). In (E), $n = 5$; two-way ANOVA; $^{*}p < 0.05$ (compared with the group of 0.25 w/v% alginate at the same time point); $\#p < 0.05$, $\#\#p < 0.01$, $\#\#\#p < 0.001$ (compared with the same group at day 5).

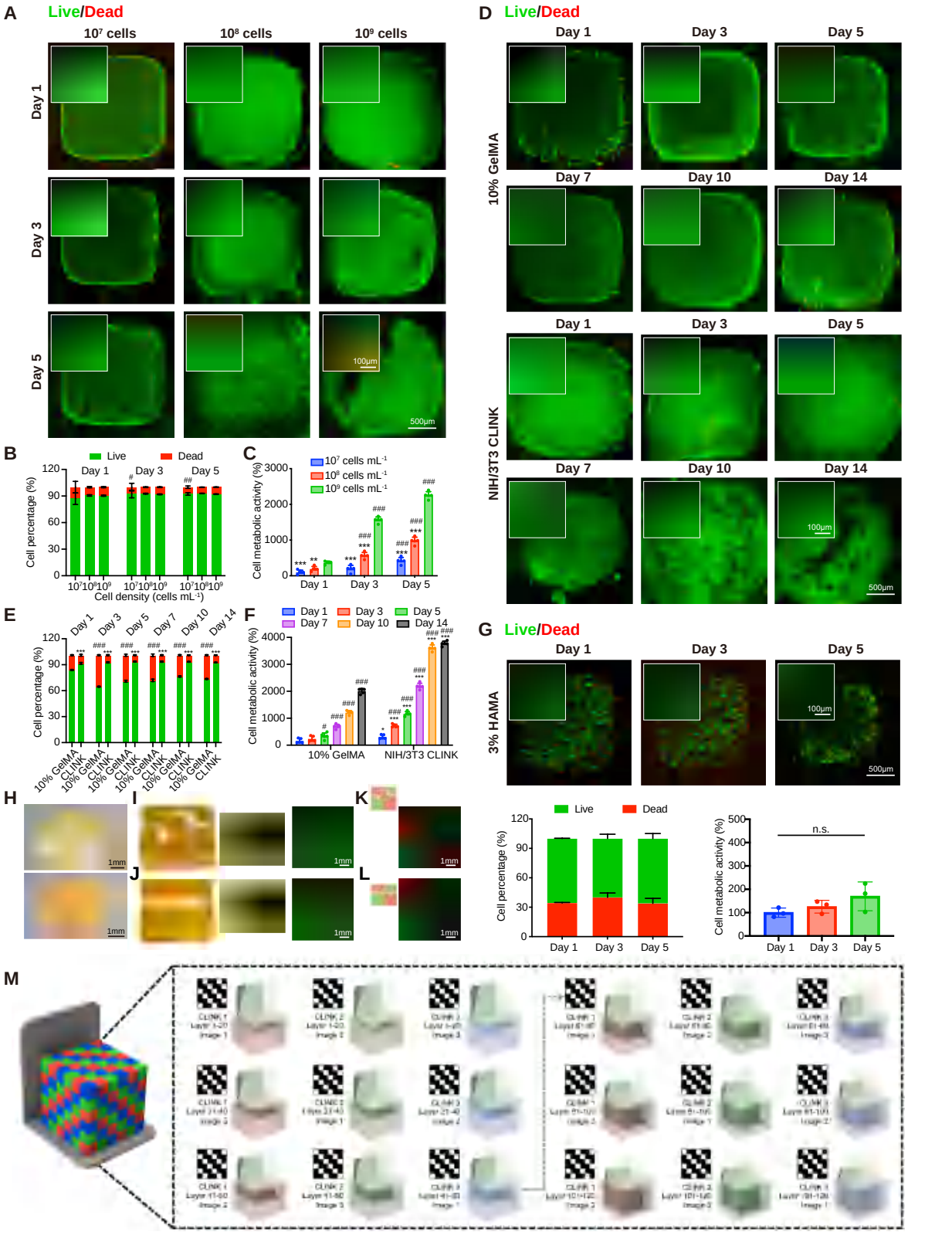

(legend on next page)

Figure S5. Evaluations of cell behavior of biomaterial-minimalistic DLP-bioprinted NIH/3T3 fibroblasts and 3D constructs and schematic of the bioprinting process, related to Figure 3

(A) Fluorescence micrographs showing live (green)/dead (red) staining of biomaterial-minimalistic bioprinted NIH/3T3 CLINK with cell densities of 10^7, 10^8, and 10^9 cells mL^{-1} on days 1, 3, and 5.

(B) Corresponding quantitative analyses of the percentages of live/dead cell ratios.

(C) Quantitative results of MTS assays showing metabolic activities of the bioprinted NIH/3T3 CLINK.

(D) Fluorescence micrographs showing live (green)/dead (red) staining of bioprinted NIH/3T3 fibroblasts in 10 w/v% GelMA hydrogels or NIH/3T3 CLINK in biomaterial-minimalistic bioprinted cell-dense constructs on days 1, 3, 5, 7, and 14.

(E) Corresponding quantitative analyses of the percentages of live/dead cell numbers.

(F) Quantitative results of MTS assay showing metabolic activities of the bioprinted NIH/3T3 fibroblasts.

(G) Evaluations of cell viabilities of DLP-bioprinted NIH/3T3 fibroblasts in HAMA. Fluorescence micrographs showing live (green)/dead (red) staining of bioprinted NIH/3T3 fibroblasts (8×10^6 cells mL^{-1}) in 3 w/v% HAMA hydrogels on days 1, 3, and 5. Corresponding quantitative analyses of the percentages of live/dead cell ratios. Quantitative results of MTS assays showing metabolic activities of the bioprinted NIH/3T3 fibroblasts.

(H) Photographs showing pyramid and ring-shaped constructs bioprinted with the NIH/3T3 CLINK. The same bioprinted pyramid is also presented in Figure S3B.

(I and J) Photographs showing constructs containing bifurcation geometries bioprinted with fluorescently labeled NIH/3T3 CLINK (green). The channels were perfused with a dark green dye.

(K and L) Fluorescence micrographs showing constructs containing bifurcation geometries bioprinted with multiple cell populations of fluorescently labeled NIH/3T3 CLINKs (green and red), containing heterogenous colors in the horizonal direction.

(M) Schematic showing the multi-material biomaterial-minimalistic DLP bioprinting process.

In (B) and (C), $n = 5$; two-way ANOVA; $^{**}p < 0.01$, $^{***}p < 0.001$ (compared with the group of 10^9 cells mL^{-1} at the same time point); $\#p < 0.05$, $\#\#p < 0.01$, $\#\#\#p < 0.001$ (compared with the same group at day 1). In (E) and (F), $n = 5$; two-way ANOVA; $^{*}p < 0.05$, $^{***}p < 0.001$ (compared with the group of 10 w/v% GelMA at the same time point); $\#p < 0.05$, $\#\#p < 0.01$, $\#\#\#p < 0.001$ (compared with the same group at day 1). In (G), $n = 3$–4; one-way ANOVA; n.s., non-significant difference.

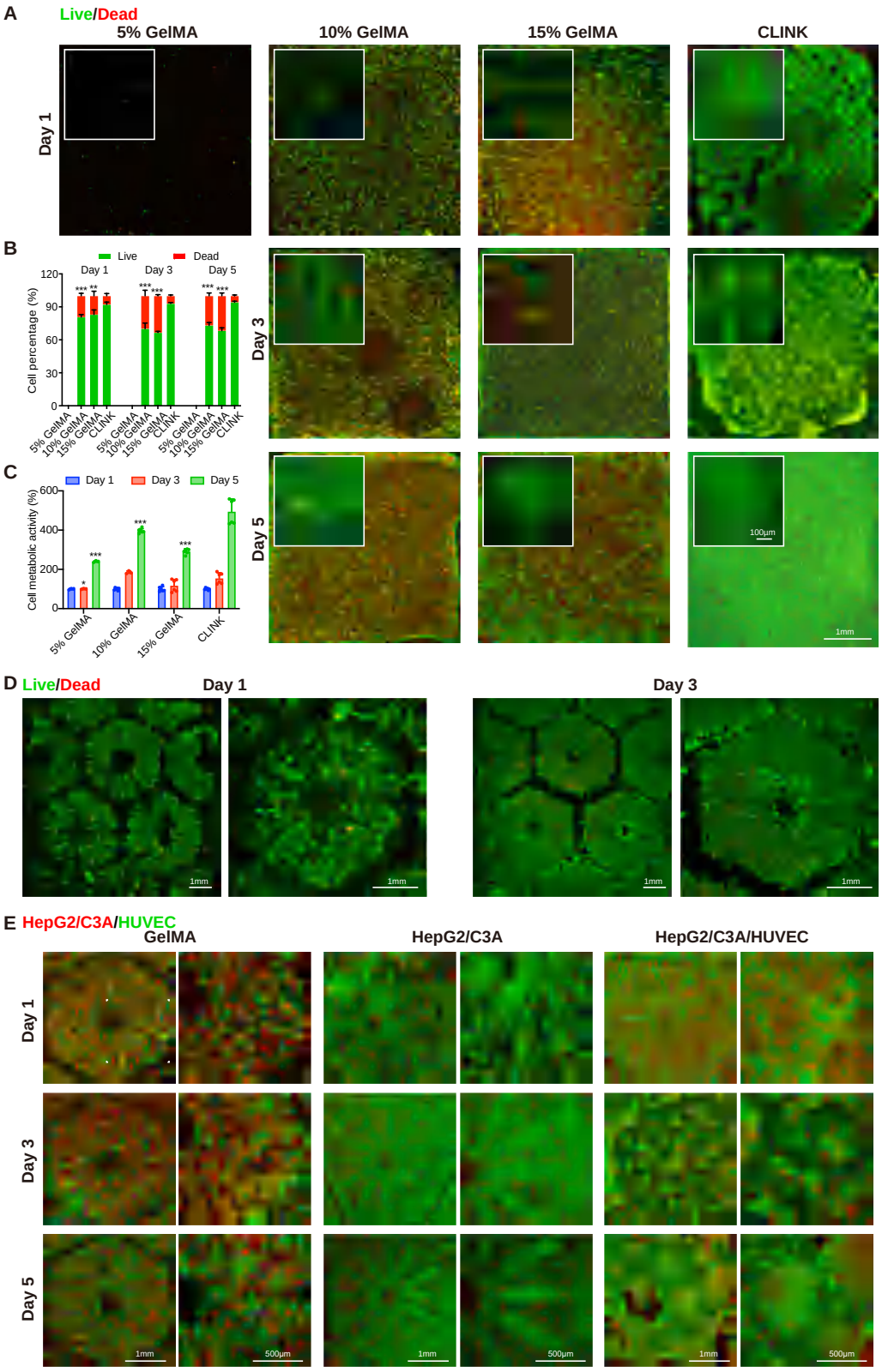

(legend on next page)

Figure S6. Evaluations of cell viabilities of bioprinted NIH/3T3 fibroblasts and HepG2/C3A hepatic tissues, related to Figure 4

(A) Fluorescence micrographs showing live (green)/dead (red) staining of bioprinted NIH/3T3 fibroblasts in 5, 10, and 15 w/v% GelMA hydrogels and in biomaterial-minimalistic bioprinted cell-dense constructs on days 1, 3, and 5.

(B) Corresponding quantitative analyses of the percentages of live/dead cell numbers.

(C) Quantitative results of MTS assays showing metabolic activities of the bioprinted NIH/3T3 fibroblasts.

(D) Fluorescence micrographs showing live (green)/dead (red) staining of biomaterial-minimalistic DLP-bioprinted cell-dense HepG2/C3A hepatic tissues.

(E) High-magnification images showing live (green)/dead (red) staining of bioprinted HepG2/C3A cells in 10 w/v% GelMA hydrogel and HepG2/C3A cells or HepG2/C3A plus HUVECs in biomaterial-minimalistic bioprinted cell-dense hepatic tissues on days 1, 3, and 5.

In (B) and (C), $n = 3–6$; two-way ANOVA; $^{*}p < 0.05$, $^{**}p < 0.01$, $^{***}p < 0.001$ (compared with the group of biomaterial-minimalistic bioprinting at the same time point).

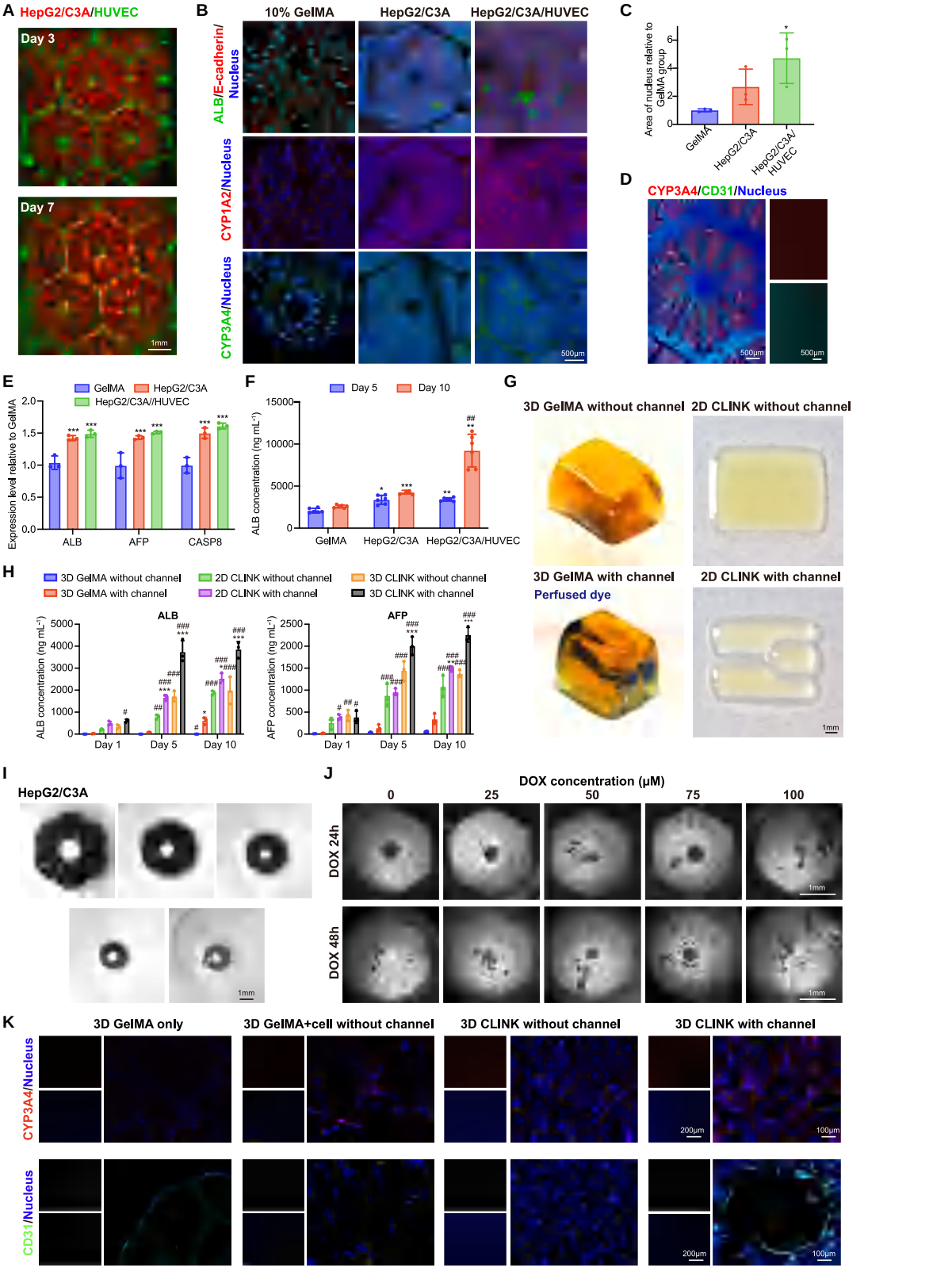

(legend on next page)

Figure S7. Evaluations of cell viabilities of bioprinted HepG2/C3A hepatic tissues, related to Figure 4

(A) Longer-term culture of biomaterial-minimalistic DLP-bioprinted cell-dense hepatic tissues containing GFP-HUVECs (green) and HepG2/C3A cells (red).

(B) Confocal immunofluorescence micrographs of ALB (green) and E-cadherin (red) or CYP1A2 (red) or CYP3A4 (green), with nucleus counterstaining (blue) of the bioprinted HepG2/C3A cells in 10 w/v% GelMA hydrogel, and HepG2/C3A cells or HepG2/C3A plus HUVECs in biomaterial-minimalistic bioprinted cell-dense hepatic tissues on day 7.

(C) Corresponding quantitative analyses of the nuclei areas.

(D) Confocal immunofluorescence micrographs of CYP3A4 (red) and CD31 (green) staining, with nucleus counterstaining (blue) of HepG2/C3A cells and HUVECs in biomaterial-minimalistic bioprinted cell-dense hepatic tissues on day 7.

(E) Plot showing gene expression levels of *ALB*, *AFP*, and *CASP8*, normalized with *GAPDH* for the HepG2/C3A cells grown in bioprinted 10 w/v% GelMA hepatic tissues, and in biomaterial-minimalistic bioprinted cell-dense hepatic tissues without or with HUVECs on day 7. All gene expression fold changes are relative to the corresponding expressions of the GelMA group.

(F) Quantitative results of ALB secretion levels of HepG2/C3A cells, grown in bioprinted 10 w/v% GelMA hepatic tissues, and in biomaterial-minimalistic bioprinted cell-dense hepatic tissues without or with HUVECs on days 5 and 10.

(G) Hepatic tissues bioprinted with 10 w/v% GelMA laden with HepG2/C3A and bioprinted with biomaterial-minimalistic cell-dense 2D CLINK of HepG2/C3A without or with perfusable bifurcation channels.

(H) ALB and AFP secretion profiles of bioprinted hepatic tissues without or with embedded hollow channels. Quantitative results show ALB and AFP secretion levels of HepG2/C3A cells, grown in bioprinted 10 w/v% GelMA hepatic tissues, and in bioprinted biomaterial-minimalistic cell-dense 2D/3D hepatic tissues without or with channels on days 1, 5, and 10.

(I) Bright-field micrographs showing identification of minimally printable hepatic lobule size.

(J) Representative bright-field micrographs showing biomaterial-minimalistic DLP-bioprinted hepatic tissues treated with varying DOX concentrations for different time points (24 and 48 h).

(K) Immunofluorescence micrographs illustrating staining results for CYP3A4 (red) and CD31 (green), with nucleus counterstaining (blue) of the hepatic tissues on day 3 post-implantation.

In (C), $n = 3$; one-way ANOVA; $^{*}p < 0.05$ (compared with the group of GelMA). In (E), $n = 3$; one-way ANOVA; $^{***}p < 0.001$ (compared with the group of GelMA). In (F), $n = 6$; two-way ANOVA; $^{*}p < 0.05$, $^{**}p < 0.01$, $^{***}p < 0.001$ (compared with the group of GelMA); $\#\#p < 0.01$ (compared with the group of HepG2/C3A). In (H), $n = 3$; two-way ANOVA; $^{*}p < 0.05$, $^{**}p < 0.01$, $^{***}p < 0.001$ (compared with the group without channels but bioprinted using the same method and on the same day); $\#p < 0.05$, $\#\#p < 0.01$, $\#\#\#p < 0.001$ (compared with the group of GelMA with channel and on the same day).

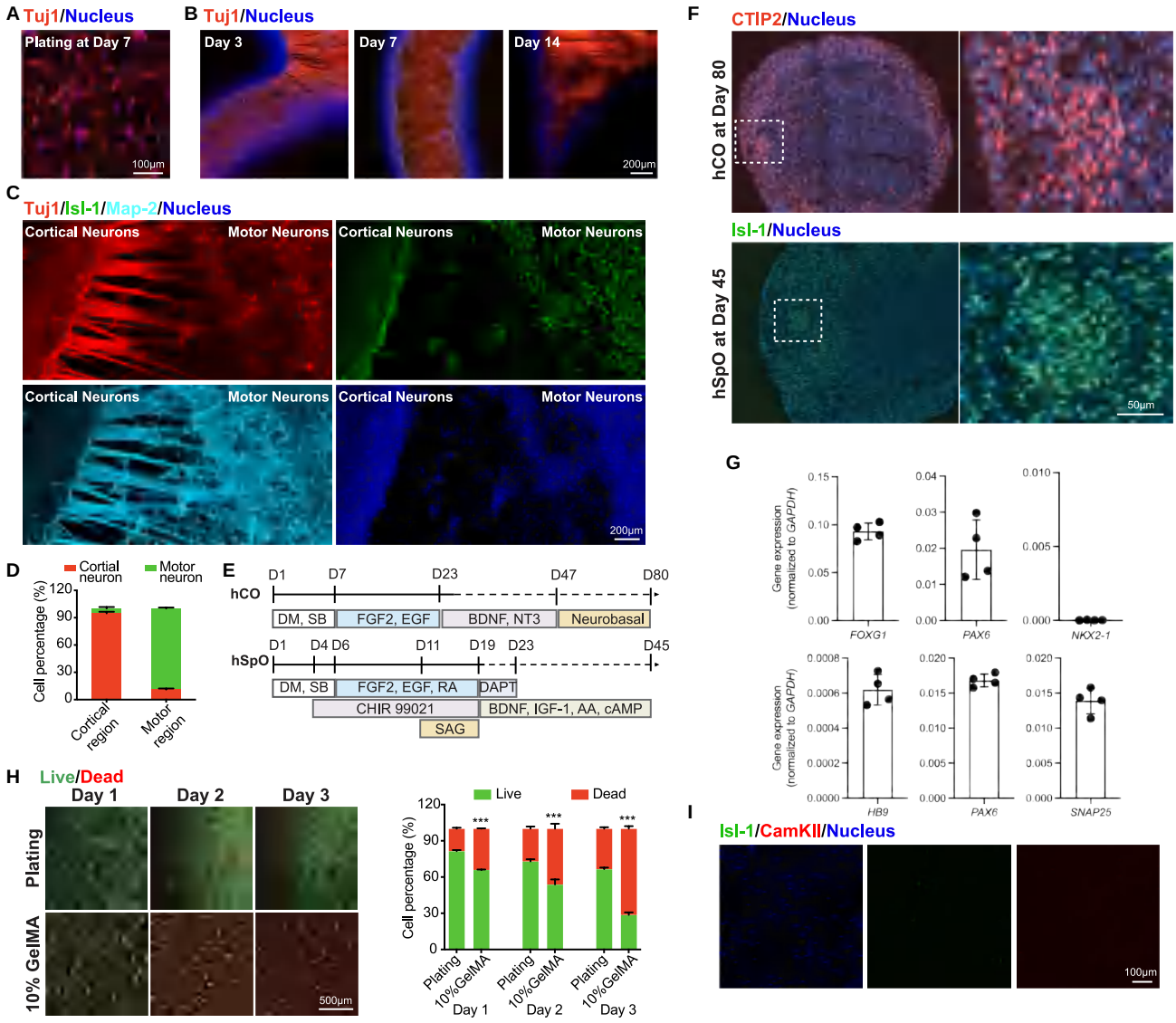

Figure S8. Investigations of bioprinted neurons, related to Figure 5

(A) Fluorescence micrographs showing Tuj1 staining (red) of cultured neurons on poly-D-lysine-coated petri dish on day 7.

(B) Fluorescence micrographs showing Tuj1 staining (red) of biomaterial-minimalistic DLP-bioprinted cell-dense neural circuits on days 3, 7, and 14.

(C) Single-channel images separately displaying cortical and motor neurons with CamKII and Isl-1-staining, as well as characterized neurites with Map-2-staining.

(D) Quantified results show the localization proportions of cortical neurons (CamKII$^+$ cells) and motor neurons (Isl-1$^+$ cells) in the two regions.

(E–G) Generation and characterizations of hCOs and hSpOs.

(E) Schematic showing the differentiation procedures for hCOs and hSpOs.

(F) Immunofluorescence micrographs showing staining of cortical neurons in hCOs at day 80 (CTIP2, red) and motor neurons in hSpOs at day 45 (Isl-1, green). The dashed boxes highlight regions magnified in the right panels.

(G) Quantitative gene expression profiles of hCOs with cortical-related genes (*FOXG1* for forebrain, *PAX6* for progenitors, and *NKX2-1* for ventral forebrain), and those of hSpOs with spinal/motor-related genes (*HB9* for motor neurons, *PAX6* for progenitors, and *SNAP25* for neurons).

(H and I) Neurons bioprinted with 10 w/v% GelMA.

(H) Fluorescence micrographs showing live (green)/dead (red) staining of plated neurons and bioprinted neurons embedded in 10 w/v% GelMA on days 1, 2, and 3 after bioprinting. Corresponding quantitative analyses reveal the percentages of live/dead cell ratios.

(I) Fluorescence micrographs showing the absence of neuron biomarker expressions detected in the bioprinted neurons embedded in 10 w/v% GelMA.

In (H), $n = 3$; one-way ANOVA; ***$p < 0.001$ (compared with the group of plating neurons).

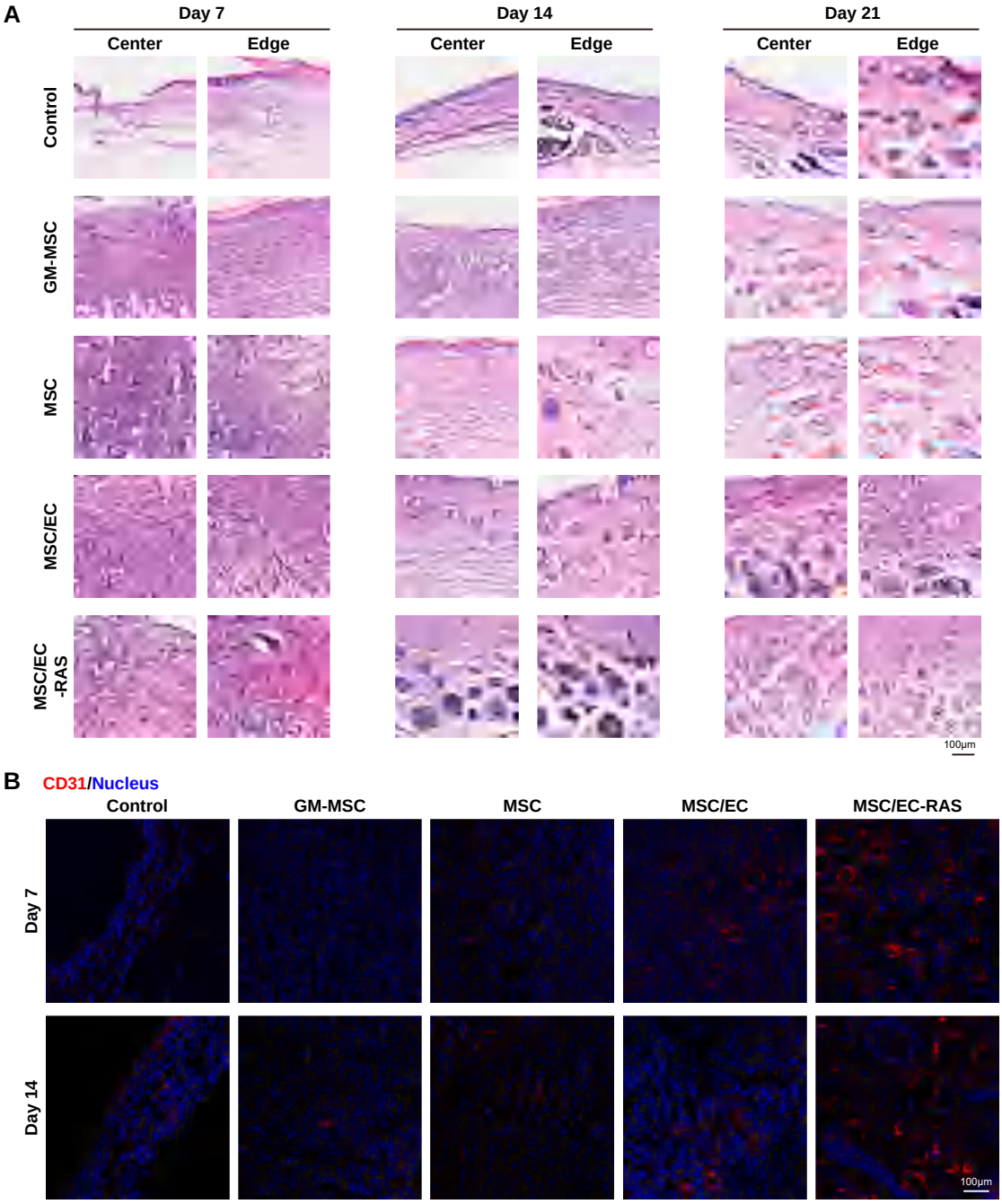

Figure S9. Evaluations of biomaterial-minimalistic DLP bioprinting of MSC/EC CLINK for skin regeneration, related to Figure 6

(A) Bright-field micrographs showing H&E staining of wounds at the center and edge regions on days 7, 14, and 21.

(B) Fluorescence micrographs showing CD31 staining of wounds on days 7 and 14.

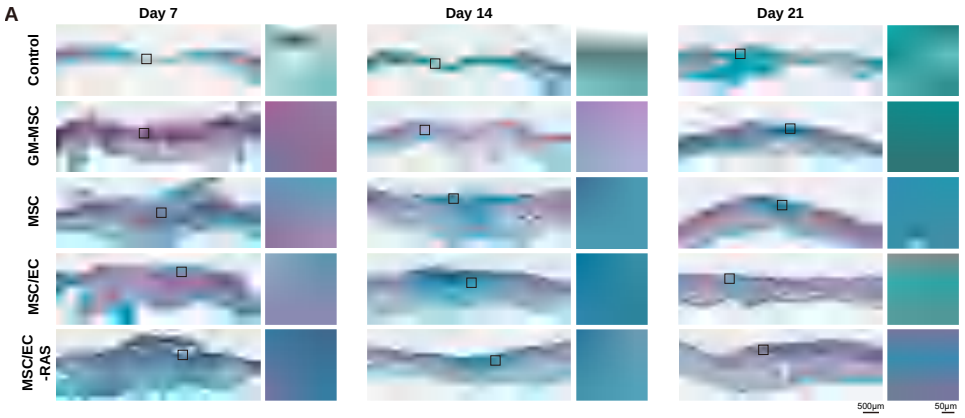

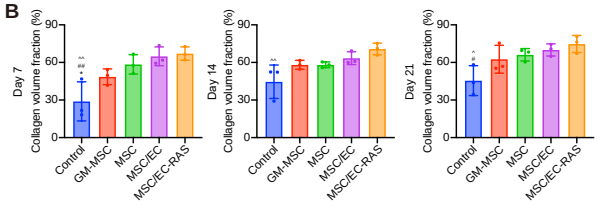

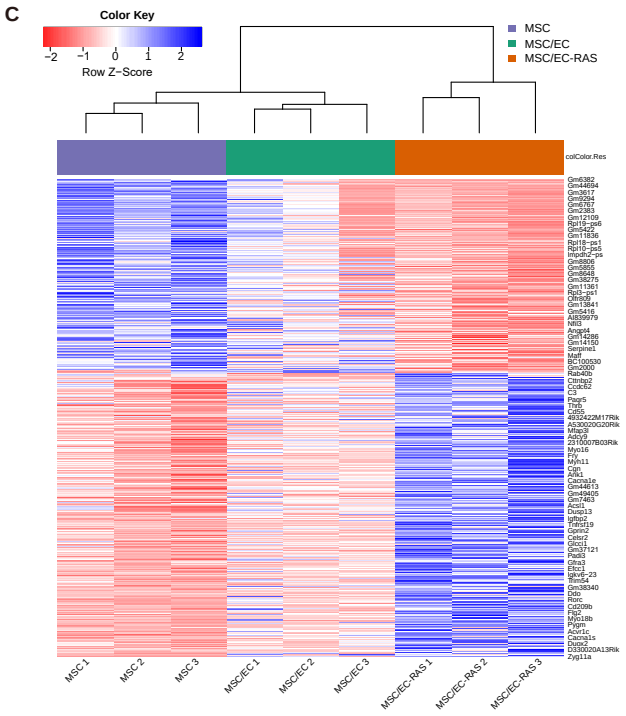

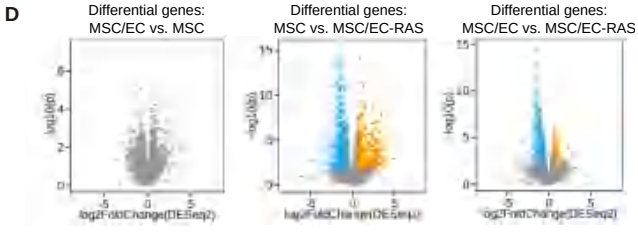

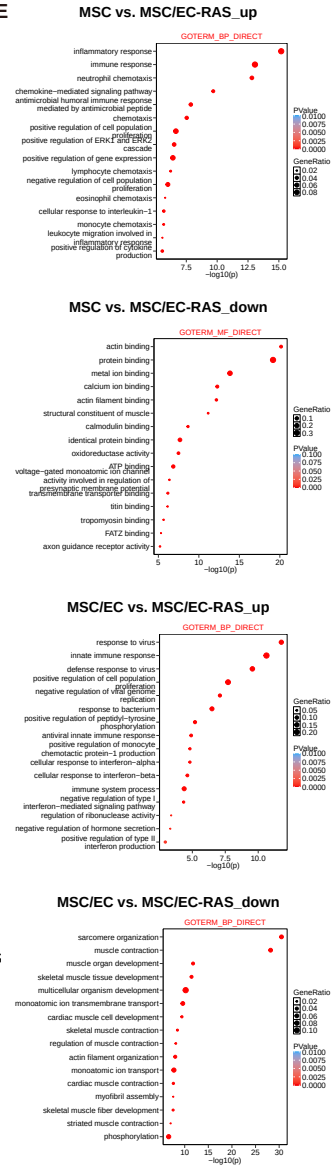

(legend on next page)

Figure S10. Evaluations of biomaterial-minimalistic DLP bioprinting of MSC/EC CLINK for skin regeneration and possible molecular mechanisms, related to Figure 6

(A) Bright-field micrographs showing Masson's trichrome staining of wounds on days 7, 14, and 21.

(B) Corresponding quantification analyses of collagen areas in the wound areas.

(C–E) Gene-expression profiling of wound healing in mice.

(C) Heatmaps of DEGs of the MSC, MSC/EC, and MSC/EC-RAS groups. Genes are indicated on the right side. Red color represents low expression levels, while blue color represents upregulated expression levels, compared with the MSC constructs.

(D) Volcano plots of the groups of MSC/EC versus MSC, MSC versus MSC/EC-RAS, and MSC/EC versus MSC/EC-RAS. Gene values are reported as a $\log_2$ fold change ($p < 0.05$).

(E) GO-enrichment plots of DEGs of the groups of MSC versus MSC/EC-RAS and MSC/EC versus MSC/EC-RAS.

In (B), $n = 3$; one-way ANOVA; *$p < 0.05$ (compared with the group of MSC); #$p < 0.05$, ##$p < 0.01$, (compared with the group of MSC/EC); ^$p < 0.05$, ^^$p < 0.01$ (compared with the group of MSC/EC-RAS).